Radiative Forcing & Feedback Through the Lens of Solar Geoengineering

by

John G. Virgin

A thesis
presented to the University of Waterloo
in fulfillment of the
thesis requirement for the degree of
Doctor of Philosophy
in
Geography

Waterloo, Ontario, Canada, 2023

Examining Committee Membership

The following served on the Examining Committee for this thesis. The decision of the Examining Committee is by majority vote.

External Examiner:	Dr. Christopher Smith Natural Environment Research Council Research Fellow University of Leeds
Supervisor(s):	Dr. Christopher Fletcher Associate Professor, Dept. of Geography University of Waterloo
Internal Member:	Dr. Jason Cole Adjunct Professor, Dept. of Geography University of Waterloo Research Scientist, Environment & Climate Change Canada
Internal-External Member:	Dr. Rebecca Saari Assistant Professor, Dept. of Civil & Environmental Engineering University of Waterloo
Other Member(s):	Dr. Ben Kravitz Assistant Professor, Dept. of Earth & Atmospheric Sciences Indiana University

Author's Declaration

This thesis consists of material all of which I authored or co-authored: see Statement of Contributions included in the thesis. This is a true copy of the thesis, including any required final revisions, as accepted by my examiners.

I understand that my thesis may be made electronically available to the public.

Statement of Contributions

This document contains three separate manuscripts that have been published or submitted to peer reviewed academic journals. The thesis expands the conventional energetic approach to assessing global climate change through a combination of external forcings and surface temperature feedbacks through the lens of solar geoengineering. That is, adapting conventional understanding of forcing and feedback in climate science to analyze potential feedback loops under a geoengineered climate. The first manuscript (Chapter 2 of this thesis) explores forcing and feedback in two different versions of an Earth System Model to understand what is driving differences in each model's surface response to greenhouse gas forcing.

Virgin, J. G., C. G. Fletcher, J. N. Cole, K. von Salzen, and T. Mitovski, 2021: Cloud feedbacks from canesm2 to canesm5. 0 and their influence on climate sensitivity. *Geoscientific Model Development*, **14 (9)**, 5355–5372

The contributions to this manuscript are as follows:

- Conceptualization - J. G. Virgin, J. N. Cole
- Formal Analysis - J. G. Virgin
- Methodology - J. G. Virgin, J. N. Cole
- Supervision - J. G. Virgin, C. G. Fletcher
- Writing - J. G. Virgin
- Review & Editing - J. G. Virgin, J. N. Cole, K. von Salzen, T. Mitovski, C. G. Fletcher

The second manuscript (Chapter 3 of this thesis) seeks to understand how greenhouse gas and solar forcing produce non-linear climate responses when combined as a proxy for a geoengineered climate.

Virgin, J., and C. Fletcher, 2022: On the linearity of external forcing response in solar geoengineering experiments. *Geophysical Research Letters*, **49 (15)**, e2022GL100 200

The third manuscript (Chapter 4 of this thesis) uses an Earth system model to simulate an idealized, transient geoengineering experiment with both greenhouse gas and solar forcing to understand how multiple external forcings can produce climate responses that feed back on one another from an energetic perspective.

Virgin, J., and C. Fletcher, 2023: Declining geoengineering efficacy caused by cloud feedbacks in transient solar dimming experiments. *Manuscript Submitted to Journal of Climate*

The contributions to Virgin and Fletcher (2022) and Virgin and Fletcher (2023) are as follows:

- Conceptualization - J. G. Virgin
- Formal Analysis - J. G. Virgin
- Methodology - J. G. Virgin
- Supervision - J. G. Virgin, C. G. Fletcher
- Writing - J. G. Virgin
- Review & Editing - J. G. Virgin, C. G. Fletcher

Abstract

Global, annual mean surface temperature continues to rise in the wake of the Paris Agreement goal of limiting warming to 2°C and pursing efforts to limit warming to less than 1.5°C. Research paradigms have arisen to analyze projections of future warming, as well as understanding the drivers of anthropogenic climate change since the preindustrial era. One such paradigm is the characterization of anthropogenic emissions of greenhouse gases as an external radiative forcing on the climate system, as well as feedbacks from the climate response to forcing that augment the rate in which the Earth system reestablishes energy balance. As surface temperatures rise, solar geoengineering has been proposed as a means to deliberately alter Earth's energy balance and achieve Paris Agreement goals through reducing the amount of incoming shortwave radiation from reaching the surface. Through the lens of the conventional forcing-feedback framework, solar geoengineering is challenging to frame due to the purposeful introduction of an external forcing in order to suppress surface warming, and therefore feedback. Furthermore, the potential for multiple external forcings via solar geoengineering to produce feedbacks from an energetic perspective, even in the absence of surface warming, is poorly understood. This thesis attempts to adapt the forcing-feedback paradigm to define potential radiative feedbacks on the climate system as a result of solar geoengineering through three studies.

First, we perform an analyses of radiative forcing and feedback between two versions of the Canadian Earth System Model (CanESM) to understand what is physically driving differences in surface warming. We find little difference in radiative forcing from increased CO_2 between the two model versions. More positive radiative feedbacks produce a larger amount of warming in CanESM5, primarily from a reduction boundary layer clouds across the equatorial Pacific that reduced the Earth's albedo to a greater extent. This analysis

was essential to understand how radiative feedbacks, specifically from clouds, can impact the rate surface warming.

Next, we analyzed radiative forcing from both increased CO_2 and a reduced solar constant using the Community Earth System Model (CESM). We find that the magnitude of solar forcing required to offset the positive radiative forcing from quadrupling CO_2 is sensitive to radiative adjustments from both forcings. Radiative adjustments, which are climate responses from an external forcing in the absence of surface warming that impact Earth's energy balance, as a result of reductions in cloud fraction had a dampening effect on the reduction of the solar constant. This work informed how solar constant tuning, which we used as a proxy for more realistic representations of solar geoengineering, can produce changes in cloud fraction that impact planetary albedo and therefore the amount solar forcing required to achieve energy balance.

Finally, we extend the work of the first two studies by defining and investigating potential geoengineering radiative feedbacks in a transient solar geoengineering experiment using CESM. We reduce the solar constant over time in an idealized geoengineering experiment that maintains near-zero global mean surface warming in the wake of increasing CO_2 and find a decreasing trend in optically thick tropical clouds. Reductions in cloud fraction reduced planetary albedo, which further decreased the amount of solar forcing needed to achieve the same net energy reduction at the surface, thus producing a positive radiative feedback loop in absence of global mean surface warming. This work highlights the need to understand potential feedbacks from realizable methods of solar geoengineering such as stratosphere aerosol injections.

Keywords: geoengineering, climate sensitivity, energy budget, cloud feedbacks, radiative forcing, earth system model

Acknowledgements

I would like to acknowledge Dr. Chris Fletcher, Dr. Jason Cole, and Dr. Karen Smith.

Chris, for five years of support and guidance. Your extensive feedback helped to make me a better writer, cautious interpreter, and mindful collaborator. In my first year on the way to a conference in Montreal, you spoke of yourself as a supervisor that "could be worse, but could be better". I do not think it could have been much better. Also, quick acknowledgment to the number of times you edited, disagreed with, and critiqued your own words through multiple manuscript revisions.

Jason, for providing me with numerous opportunities to showcase work, investigate new ideas, and a chance to collaborate with the scientific community at Environment and Climate Change Canada. Your perspectives and scientific insight shaped the trajectory of this thesis more than anything else.

Karen, for enabling my interest in climate science despite my lack of preparedness. Your support and patience through a steep learning curve was the primary driver behind me pursuing a PhD program, and so I would not have made it this far without it.

Finally, I would like to also acknowledge the rest of my examining committee for committing their time and energy to provide guidance and thoughtful critique throughout the comprehensive examination and thesis defence process.

Dedication

"If you hate to go to school, you may grow up to be a mule."

For Gerry Fogarty.

Table of Contents

List of Figures

List of Tables

List of Abbreviations

AA Arctic amplification 82

AMIP Atmosphere Model Inter-comparison Project xiv, 29

AOD aerosol optical depth 67

BTS bulk tropospheric stability 95

CAM4 Community Atmosphere Model 4 51

CAMRT Community Atmosphere Radiative Transfer Model 54

CanESM Canadian Earth System Model 20

CCCma Canadian Centre for Climate Modeling and Analysis 20

CCF cloud controlling factor 19

CDR carbon dioxide removal 7

CESM Community Earth System Model 51

CFMIP Cloud Feedback Model Inter-comparison Project 41

CH_4 methane 2

CICE Community Ice CodE Model 69

CLM4 Community Land Model 4 51

CLUBB Cloud Layers Unified By Binormals 109

CMIP6 Coupled Model Inter-comparison Project 18

CO_2 carbon dioxide 1

COSP Cloud Object Simulator Package 24

CRE cloud radiative effect 24

CTP cloud top pressure 51

ECS effective climate sensitivity 6, 18

EIS estimated inversion strength 39

ERF effective radiative forcing 2, 21

ESM earth system model 5, 19

ESS earth system sensitivity 6

GE geoengineering effiency 9

GeoMIP Geoengineering Model Inter-comparison Project 12, 49

GFDL Geophysical Fluid Dynamics Laboratory 24

GHG greenhouse gases 2

GLENS Geoengineering Large Ensemble 110

HadGEM Hadley Centre Global Environment Model 24

IRF instantaneous radiative forcing 3, 50

ISCCP International Satellite Cloud Climatology Project 24

LCC low cloud cover 19

LES large eddy simulations 19

LW longwave 1, 24

MCB marine cloud brightening 8

N_2O nitrous oxide 2

OLR outgoing longwave radiation 2, 5, 60

PBL planetary boundary layer 8, 19

PI proportional-integral 72

POP2 Parallel Ocean Program 2 69

RF radiative forcing 2

RFMIP Radiative Forcing Model Inter-comparison Project 22

RHS right hand side 54

RRTM Rapid Radiative Transfer Model 24

RTM River Transport Model 69

SAG stratosphere aerosol geoengineering 8, 66

SI system identification 73

SRM solar radiation modification 7, 79

SSP Shared Socioeconomic Pathways 67

SST sea surface temperature 5, 19

SW shortwave 1, 19

TOA top of atmosphere 1, 21

Chapter 1

Introduction

1.1 Radiative Forcing & Feedback

The global climate is a system of energy flows. The Earth receives radiant energy from the sun in the form of ultraviolet radiation and primarily emits energy back to space in the form in infrared radiation. Over long timescales, the climate system relaxes toward these two energy flows balancing each other, pushing the system to be in an equilibrium state where the net radiative flux at Earth's top of atmosphere (TOA) is close to zero. Earth's annual mean atmosphere energy budget is shown in Figure 1.1. The atmosphere acts as an intermediary to the flux of radiation in both the shortwave (SW) and the longwave (LW) wavelengths, where SW is categorized into radiation between 0.1 and 4 microns and LW categorized as > 4 microns. The Earth's variable surface topography, clouds, and gaseous absorbers (e.g., carbon dioxide (CO_2), H_2O) in the atmosphere all interact with radiation in some form to augment the flows of radiant energy either through reflection, absorption and remission, or latent and sensible heat fluxes (Kiehl and Trenberth, 1997).

As noted in Figure 1.1, the atmosphere is more transparent to SW radiation reaching the surface than LW radiation escaping to space. The Earth's atmosphere is more opaque in the LW, meaning that less radiation is fully transmitted from the surface to space due to the presence of gaseous absorbers and clouds, which fully absorb and re-emit radiation along specific wavelengths in the LW. For example, the 15 μm wavelength band is fully opaque, where 100% of radiation is absorbed in Earth's atmosphere due to the presence of CO_2 (Hartmann, 2015). In contrast, the 8-14 μm band, or "atmospheric window", is nearly completely transparent to LW radiation in the atmosphere (see Figure 1.1). The vertical distribution of temperature also impacts the total flux of thermal infrared radiation as well where outgoing longwave radiation (OLR) approximately scales to the fourth power of temperature.

In the SW, transmittance of radiation from the sun to the Earth's surface is impacted by both absorption and scattering in the atmosphere. The optical depth of the atmosphere is defined as the proportion by which it reduces an incident beam of solar radiation by both the combination of extinction due to absorption and scattering. Clouds and gaseous absorbers (e.g., water vapour) both contribute to the atmosphere's optical depth (see "absorbed atmosphere" and "reflected" in the yellow lines in Figure 1.1).

Changes to the flows of radiant energy in the climate system by the introduction of an external agent is defined as radiative forcing (RF) (Ramanswamy et al., 1991). The principle RF example is anthropogenic emissions of well mixed greenhouse gases (GHG) such as CO_2, methane (CH_4), and nitrous oxide (N_2O). Global emissions of GHG, measured in tonnes of CO_2 equivalent, reached 55$\pm$5.2Gt in 2022 (Forster et al., 2023). In terms of radiation, the effective radiative forcing (ERF) from all anthropogenic sources aggregated over 1750-2022 was 2.91 W m^{-2} ($\pm$0.72 W m^{-2}, 5-95% confidence interval).

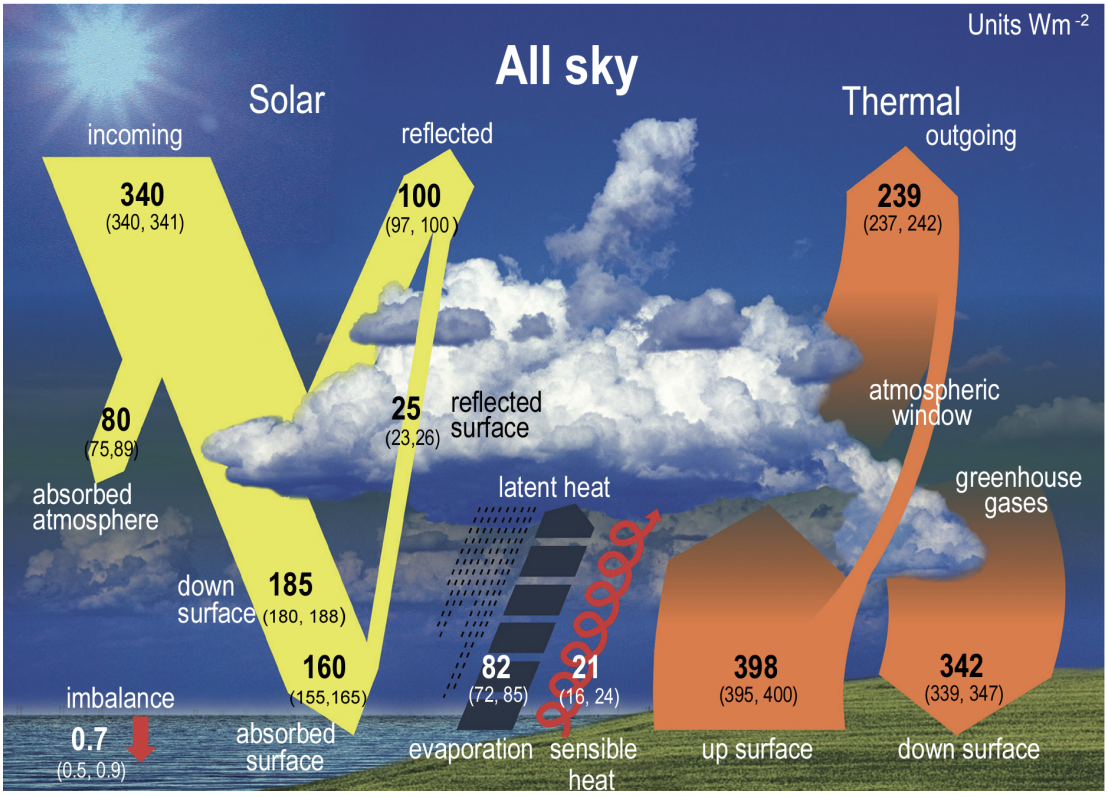

Figure 1.1: Schematic showing Earth's annual mean atmosphere global energy budget. Yellow arrows denote shortwave radiation, red arrows denote longwave radiation, and the green arrow denotes latent and sensible heat flux from thermals and evapotranspiration. This figure was adapted as shown here by Forster et al. (2021) and originally produced in Kiehl and Trenberth (1997).

Effective radiative forcing is defined as the total RF from an external agent, which is comprised of both an instantaneous component and a radiative adjustment (Sherwood et al., 2015; Hansen et al., 2005). The instantaneous component of the RF is the direct radiative flux change as a result of changes in atmospheric composition (Figure 1.2a). In the case of an increase in CO_2 concentration, the instantaneous component, or instantaneous radiative forcing (IRF), is the increase in downwelling LW flux towards the surface as a result of absorption and remission from CO_2. Observational evidence of the IRF from all

historical forcing agents show that the radiative impact from increasing GHG emissions has increased in the twenty-first century, where Kramer et al. (2021) estimated the total historical IRF from 2003 to 2018 increased by 0.53± 0.11 W m^{-2}. This result was not only driven by increased GHG emissions, but also from a reduction in aerosol emissions as well.

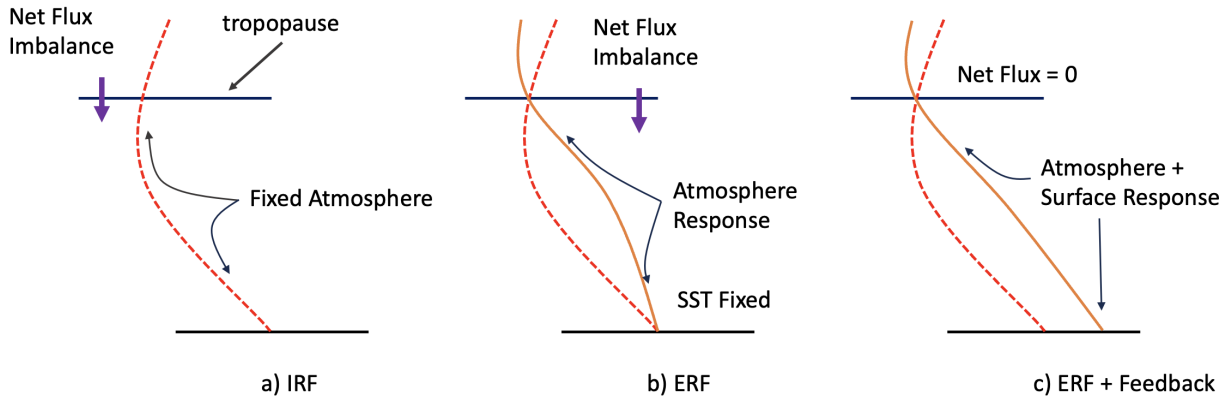

Figure 1.2: Conceptual diagram comparing the atmosphere and surface response to perturbation for a) the instantaneous radiative forcing (IRF), b) the effective radiative forcing (ERF), and c) the full system response (atmosphere+surface). This figure has been adapted from Figure 2 in Hansen et al. (2005).

Studying Earth's radiation budget through analysis of RF has significantly advanced our understanding of both anthropogenic climate change and the climate system as a whole (Wetherald and Manabe, 1975; Hansen et al., 1997, 2005; Zhang and Huang, 2014). The taxonomy of RF has evolved to reflect our scientific understanding as well. As noted in the previous paragraph, the IRF is only one component of the total ERF. Radiative adjustments, which are defined as the radiative flux from the total atmosphere response after a forcing agent has been introduced (Figure 1.2b), are a key source of study as well (Chung and Soden, 2015; Sherwood et al., 2015). Radiative adjustments occur from changes in state variables that perturb atmosphere infrared opacity or planetary albedo. Changes in clouds, air temperature, water vapour, and surface albedo all result in either

more or less radiation escaping to space, which alters Earth's TOA energy budget.

Earth system models (ESMs) are particularly useful for studying the RF of specific climate forcers such as aerosols, GHGs, or land use change. With the ability to constrain model components (e.g., the ocean), one can isolate specific responses from ESMs. By definition, the ERF term excludes the surface response, which practically manifests in academic study by fixing the ocean sea surface temperatures (SSTs) and sea ice variables (Pincus et al., 2016). The atmosphere responds comparatively fast in relation to the ocean, which has led to radiative adjustments being defined as "rapid" adjustments as well (Gregory et al., 2004). Therefore, the ocean's response to forcing, which is on longer timescales of years to decades to centuries, is defined as a feedback (Hansen et al., 1984; Cess et al., 1990). Where there is no feedback (e.g. in a fixed-SST experiment design with ESMs), net TOA flux $\neq 0$ as the Earth's blackbody response (also known as the Planck response) is constrained and OLR from the surface cannot increase without changes in temperature (Figure 1.1, see "radiation emitted by surface", and Figure 1.2a & b).

When the surface is not constrained and is allowed to respond to external forcing, changes in SSTs impact other variables such as clouds, air temperature, and surface albedo that further perturb Earth's energy budget, which then feed back onto the surface (Figure 1.3). This forcing-feedback framework is a classic method of study with both ESMs and other, simpler climate models that has been rigorously analyzed in climate science and continues to inform our understanding of climate change today. For modelling global mean surface temperature, the relationship between forcing and feedback is expressed linearly, where the change in net TOA radiative flux from forcing is balanced over time by changes in temperature (Gregory et al., 2004).

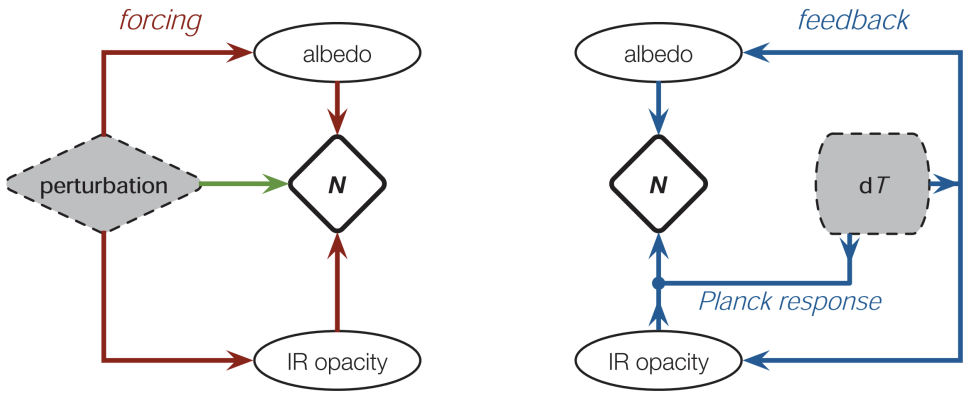

Figure 1.3: Conceptual diagram showing forcing (left) and feedback (right) through their impact on planetary albedo and atmosphere infrared opacity. This figure has been adapted from Figure 1 in Sherwood et al. (2015).

The forcing-feedback framework has been used extensively to quantify uncertainty with respect to climate sensitivity in ESMs. Climate sensitivity, or the amount of warming the Earth would exhibit as a response to a positive ERF, is easily quantified using the linear framework. The most commonly used metric is warming as a response to an instantaneous doubling of atmosphere CO_2 concentration– effective climate sensitivity (ECS) Charney et al. (1979). The term "effective" in ECS as it is defined here is a deliberate reference to the modelled linear relationship between radiative forcing and warming, where ESMs are forced with an abrupt doubling or quadrupling of CO_2 and then global, annual mean surface warming when the system reaches equilibrium is estimated by linear regression Andrews et al. (2012). Given this is an extrapolation, it is not representative of warming once an ESM reaches true equilibrium Knutti et al. (2017). Furthermore, this simplified approach does not encompass all feedbacks and assesses warming on relatively shorter timescales (centuries). Earth system sensitivity (ESS) is intended to be a more holistic term as it accounts for feedbacks on longer timescales such as changes in vegetation, permafrost, ice

sheets, and atmospheric chemistry (Knutti and Rugenstein, 2015). However, the feedbacks incorporated into the definition of ESS span millennia that many ESMs do not explicitly resolve. Therefore, effective climate sensitivity, while a simplification, is still a useful emergent property of ESMs that gives insight into both forcing and feedback as they have been discussed thus far.

1.2 Geoengineering

Geoengineering is defined as deliberate manipulation of Earth's energy budget via anthropogenic means. The term is broad in scope and meant to capture a wide array of proposed methods to modify radiant energy fluxes (Figure 1.4). Sometimes referred to as emergency climate intervention, the concept of purposeful human intervention of Earth's energy budget is not a new one, as albedo modification and various other concepts have been suggested over the past 50 years (Caldeira and Bala, 2017). However, in the wake of the 2016 Paris Agreement goals of limiting global, annual mean surface temperature rise to <2°C and pursuing efforts to limit warming to < 1.5°C, geoengineering as a potential means to offset the positive ERF from increasing GHG emissions has received more attention from academia (this thesis being no exception). Geoengineering can be separated into two categories— solar radiation modification (SRM) and carbon dioxide removal (CDR). CDR techniques encompass both technological means to remove CO_2 from the atmosphere such as direct air capture, as well as enhancement of natural carbon sinks such as reforestation and Biochar (Figure 1.4). In contrast, SRM techniques aim to reduce the amount of direct SW radiation incident on the Earth from reaching the surface. There are some other proposed geoengineering techniques that attempt to manipulate LW radiative flux in the atmosphere such as modifying cirrus cloud opacity, which is neither CDR nor SRM

(Mitchell and Finnegan, 2009).

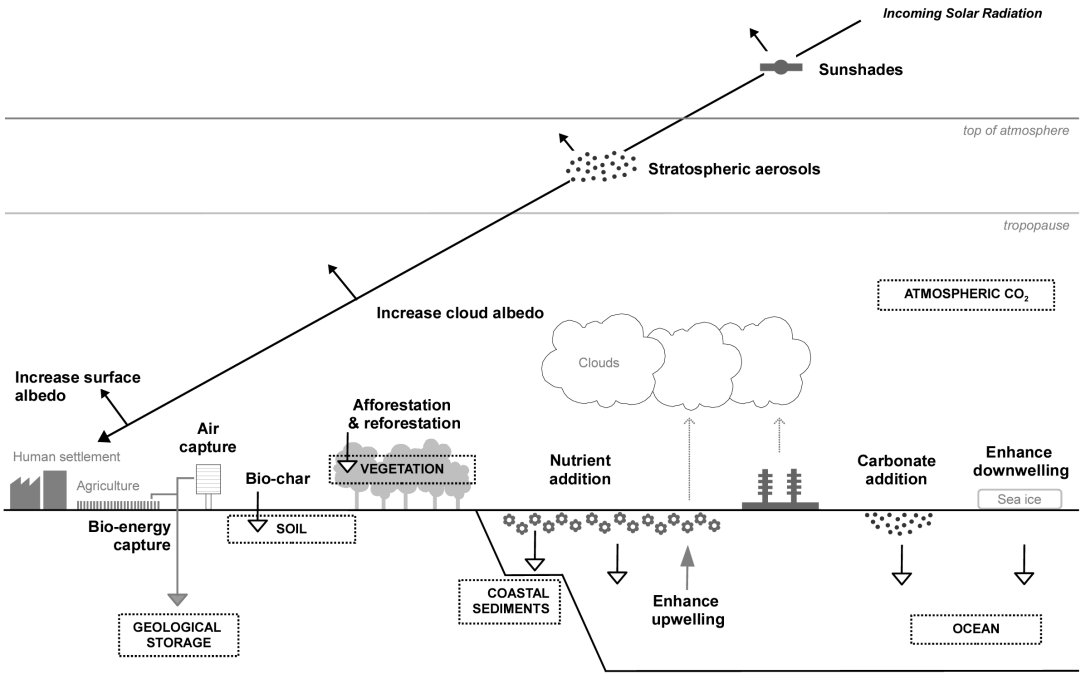

Figure 1.4: Conceptual diagram showing an overview of potential geoengineering strategies. Filled in black arrows indicate shortwave radiation, white arrow heads indicate enhancing natural flows of carbon, dotted arrows indicate sources of cloud condensation nuclei (Lenton and Vaughan, 2009).

Two proposed SRM techniques that adapt on naturally occurring processes in Earth's climate are stratosphere aerosol geoengineering (SAG) and marine cloud brightening (MCB) (Latham et al., 2012; Rasch et al., 2008). MCB is an iteration on the naturally occurring process of water droplets near the planetary boundary layer (PBL) nucleating on sufficiently small enough aerosol particles to form cloud droplets, thus increasing the optical depth of stratocumulous clouds (Latham, 1990). MCB would seed these clouds with aerosols to produce more CCN of an effective radius, which would increase optical depth and there-

fore planetary albedo. SAG's naturally occurring analogue is volcanic eruptions. The 1991 Mount Pinatubo eruption ejected approximately 20 Mt SO_2 into the stratosphere, which produced a transient negative ERF and offset a portion of warming from greenhouse gas emissions (Stenchikov et al., 1998). SAG would involve injections of SO_2 into the stratosphere to mimic this effect, albeit with specific targets and objectives in mind.

Of all proposed geoengineering techniques, research into the effectiveness, impacts, cost, and technical implementation of SAG has progressed the most over the past decade (Kravitz and MacMartin, 2020). Modeling studies using ESMs with SAG experiment designs have provided some confidence in its effectiveness to avoid more severe impacts of climate change with sophisticated injection techniques (Tilmes et al., 2018; Kravitz et al., 2017). However, there is also some level of confidence in the trade offs associated with SAG, such as stratosphere ozone reduction (Tilmes et al., 2009). There is substantial uncertainty as well given both the lack of a historical precedent, field research, and inherent knowledge gaps and large uncertainty in our understanding of the climate system. Of particular importance is the uncertainty in the efficiency of SAG from an energy budget perspective, where geoengineering effiency (GE) is defined as the ERF, in W m^{-2}, per some unit of geoengineering (e.g., per Tg injection of SO_2). Outside of the physical impacts, SAG also presents a challenge in international governance as well due to its relatively inexpensive cost compared to projected changes to GDP as a result of climate change, coupled with its global scope (McLaren and Corry, 2021).

Some of the trade offs with SAG and SRM more generally can be characterized simply by virtue that any adverse impacts from increased atmosphere CO_2 concentration is not addressed, such as ocean acidification (Robock, 2008). From a governance perspective alone, deployment of SRM could catalyze emissions intensive activities as the perceived risk would be reduced. Furthermore, if any implementation of SAG is not strategic in its

deployment to try and reduce the disparity of impacts, some developing regions may be disproportionately impacted from either first order (e.g., air quality from aerosol deposition), or second order (e.g., impacts on regional climate regimes). Reliance is another note of caution for any implementation of geoengineering, where increased SAG alongside GHG emissions would necessitate persistent and larger injections in order to prevent a fast "termination" effect on Earth's climate (Jones et al., 2013). Notably, this risk assumes a chronic increase in net GHG emissions throughout the deployment of some form of SRM. From a geopolitical perspective, SRM could be used as a tool for targeted adverse regional climate impacts should the implementation measures become more sophisticated. Lastly, there may also be direct impacts on natural vegetation or agriculture from reduced SW radiation reaching the surface (Robock, 2008). However, some research has speculated that more diffusive radiation reaching the surface, coupled with the CO_2 fertilization effect on plants and its positive impact on net primary productivity, could offset this (Glienke et al., 2015). Vegetation impacts from SRM and CDR are still highly uncertain and model dependent.

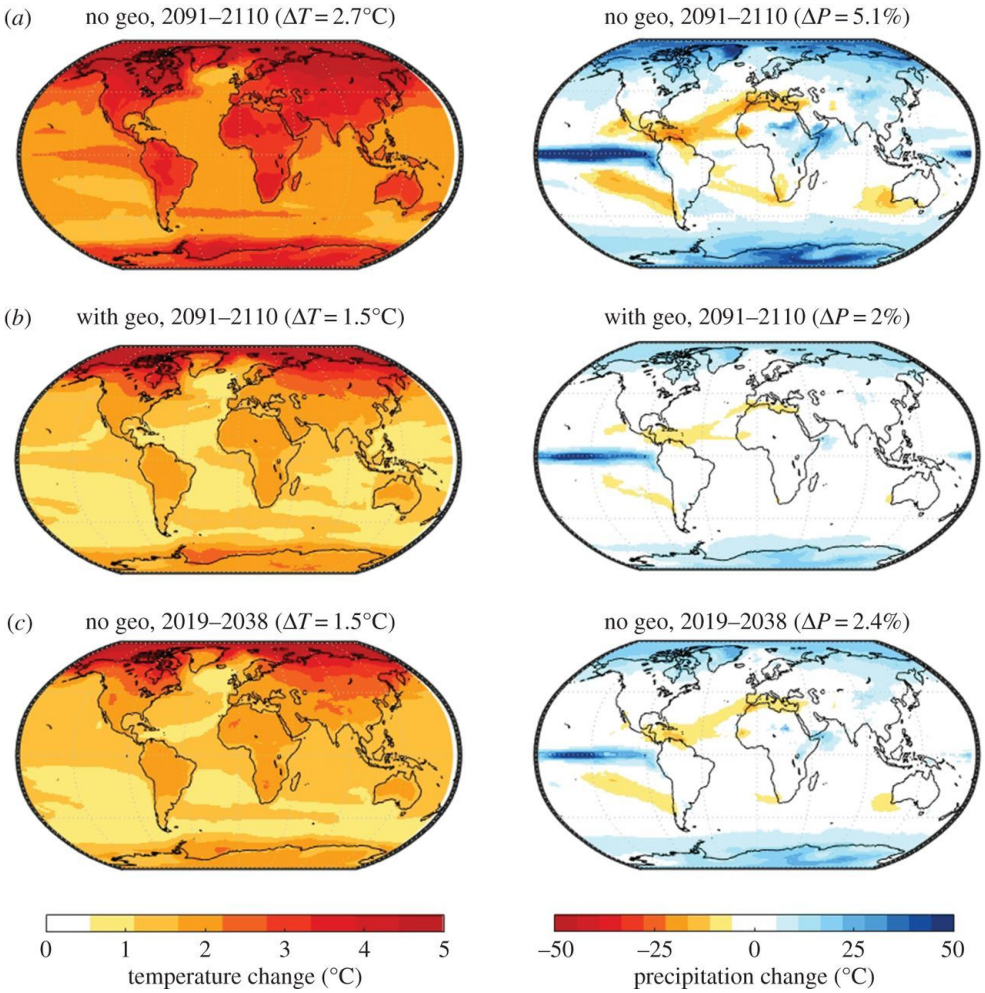

Figure 1.5: Median projected surface temperature (left) and precipitation changes (right) by the end of century for a climate with geoengineering ("with geo", subplot b) and without geoengineering under RCP8.5 ("no geo", subplot a and c). In this scenario, SRM is used to meet Paris Agreement targets by 2100. The "with geo" simulation output here is produced from an emulator trained on an ensemble of models participating in GeoMIP(MacMartin et al., 2018).

ESMs have been a cornerstone of solar geoengineering research with their ability to simulate a wide variety of experiment designs. Figure 1.5[1] illustrates the potential for

[1]This figure was extracted as is from its source publication. The precipitation colour bar unit is incorrectly labelled as °C here, where it should be %

modelling techniques to simulate target-based hypothetical scenarios where a mix of CDR and SRM are deployed to meet Paris Agreement targets. The changes plotted in Figure 1.5 show similar spatial patterns of surface temperature (i.e. polar amplification) and hydrological cycle changes as a "no geo" simulation, but smaller in magnitude and satisfying the Paris Agreement 1.5°C target. Here, SRM was simulated using an ensemble of ESMs directly modifying the amount of incident SW radiation on Earth's atmosphere as proxy for SAG. These "solar dimming" style experiments are useful as an accessible experiment design for ESMs of varying complexity, as experiment designs with SAG need to consider aerosol-cloud interactions, stratospheric chemistry, and prognostic treatment of aerosols (Visioni et al., 2021a). Where more ESMs are able to run solar dimming experiments, a larger ensemble size provides a more robust assessment of structural uncertainty embedded within ESMs.

Model inter-comparison projects have been essential for both catalyzing solar geoengineering research and providing a means to assess geoengineering impacts through inter-model uncertainty. The Geoengineering Model Inter-comparison Project (GeoMIP) is a standard set of experiments designed for modeling groups to run in order to facilitate inter-model comparison of various proposed geoengineering solutions (Kravitz et al., 2011b, 2015). Designs ranged from simple, such as the G1 experiment where solar dimming offset a prescribed increase in CO_2 (Figure 1.6a), to more realistic, such as the G6sulfur experiment (Figure 1.6b) where injections of SO_2 are prescribed to bring the ERF from Shared Socioeconomic Pathway (SSP) tier 1 high forcing scenario down to that of a medium emissions SSP scenario. While the G6sulfur experiment was related to policy relevant experiments, the G1 experiment and G6Solar experiment are useful to understand geoengineering efficiency from an energy budget perspective— particularly in the context of radiative adjustments. Radiative adjustments and their impact on the global energy bud-

get, as well as their potential to impact geoengineering efficiency through changes in clouds, temperature, water vapour, or surface albedo, are still poorly understood.

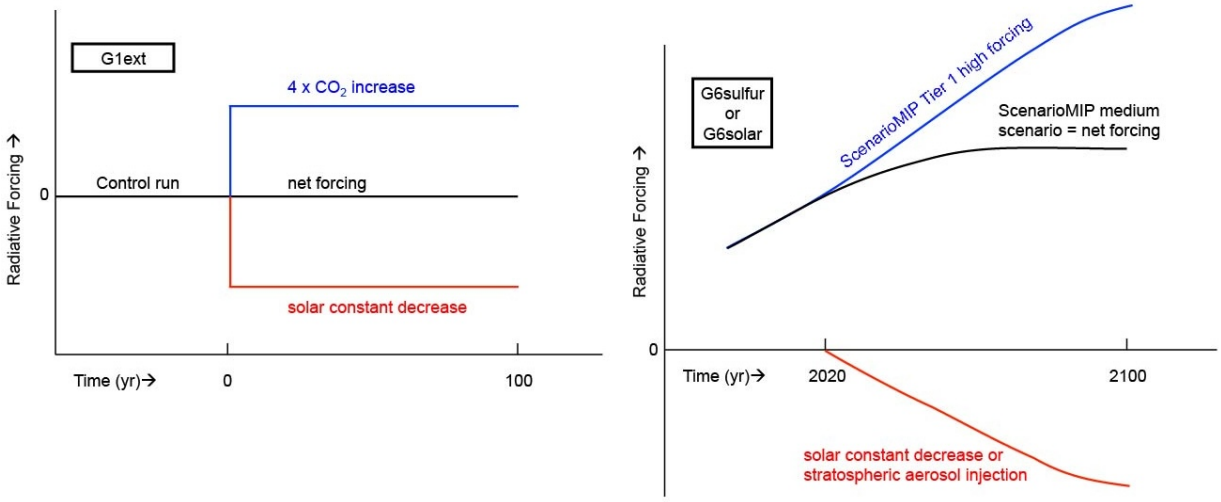

Figure 1.6: Three ESM geoengineering experiment designs from GeoMIP6. This figure has been adapted from Figures 1 and 2 in (Kravitz et al., 2015)

1.3 Research Goals

The overarching purpose of this thesis is to demonstrate how the conventional forcing-feedback paradigm for analyzing feedbacks in the climate system using ESMs could be adapted to quantify potential radiative feedbacks for geoengineering experiments. These feedbacks, henceforth referred as geoengineering feedbacks, could advance our understanding of forcing efficacy for geoengineering techniques given their focus on TOA radiative balance, which has a first-order impact on surface temperature response. While the third and final manuscript is primarily focused on addressing the overarching purpose, the chronology of all three manuscripts build on top of one another with the methods, results, and

conclusions that culminate in the final manuscript.

The research goals of this thesis are as follows:

1. Use conventional methods and climate model experiment design to understand how radiative forcing and individual radiative feedbacks contribute to differences in climate sensitivity and surface warming between ESMs.

2. Understand the physical drivers of surface radiative feedbacks and how they impact planetary albedo and atmosphere infrared optical opacity, and therefore energy balance.

3. Leverage the use of fixed-SST experiment design to quantify and differentiate radiative adjustments from surface radiative feedbacks and how they influence TOA energy balance, and therefore forcing efficacy. Extend the analysis of adjustments to assess solar forcing efficacy as a proxy for geoengineering.

4. Develop a method for quantifying geoengineering radiative feedbacks in transient dual-forcing experiments, where CO_2 is incrementally increased and the solar constant is decreased. Use this methodology to understand how geoengineering efficiency may evolve over time as a result of changes in planetary albedo.

Goals 1 & 2 are addressed in Chapter 2, goal 3 in Chapter 3, and goal 4 in Chapter 4. These goals are revisited in Chapter 5 as part of concluding remarks.

1.4 Chapter Structure

This thesis is comprised of three manuscript chapters and two supporting chapters. Chapter 1 and 5 are the supporting introductory and conclusion chapters, respectively. Chapters

2, 3, and 4 are the main body of thesis and contain three manuscripts that were published or submitted to be published in academic journals. The manuscript chapters follow in the chronological order that each manuscript was submitted for publication. Each manuscript chapter is a self contained study and has been reformatted for this thesis document as written for their respective journal. All references have been aggregated across the five chapters into the references section. While each manuscript stands alone, the results and conclusions drawn in the order that they are presented are a direct through-line to the research goals of this thesis as outlined in the previous section.

Chapter 2, the first manuscript, is an analysis of radiative forcing and feedback between two versions of the Canadian Earth System Model (CanESM) using idealized forcing experiments. With respect to CanESM, this manuscript was an attribution study to understand what was driving a large increase in ECS from CanESM2 to CanESM5. For this thesis, Chapter 2 is an analysis of CO_2 forcing and surface temperature radiative feedbacks in a warming climate. The supporting information document published alongside this manuscript has been reformatted as Appendix A

Chapter 3 shifts the focus onto radiative forcing rather than feedback. Using the fixed-SST experiment design with the Community Earth System Model, this manuscript decomposes the IRF and radiative adjustments for idealized CO_2 and solar forcings in order to understand how rapid adjustments from solar constant tuning contribute to its total ERF. Through the lens of geoengineering, this manuscript explores how the total troposphere adjustment in idealized solar dimming experiments is driven by both CO_2 and solar forcing, which has implications for trying to model geoengineering in terms of energy balance. The supporting information document published alongside this manuscript has been reformatted as Appendix B.

Chapter 4 combines the thematic focus of the previous two manuscripts to assess geo-

engineering feedbacks in transient solar dimming experiments. In contrast to the fixed-SST configuration of CESM used for Chapter 3, this study uses the full coupled configuration of CESM with an active ocean to simulate an idealized solar dimming experiment where the solar constant parameter in CESM is dynamically adjusted every year to suppress global mean surface warming in response to increasing CO_2. This experiment is used to quantify a new type of radiative feedback specifically for geoengineering experiments that have multiple external forcings, as well as a spatially heterogeneous surface temperature response. The version of this chapter submitted for publication has an appendix, which has been reformatted here as Appendix C. Lastly, Chapter 5 discusses some limitations of the methods used across all three manuscripts, as well as avenues for possible future research.

Chapter 2

Cloud Feedbacks from CanESM2 to CanESM5.0 and their Influence on Climate Sensitivity

2.1 Overview

The newest iteration of the Canadian Earth System Model (CanESM5.0.3) has an Effective Climate Sensitivity of 5.65 kelvin, which is a 54% increase relative to the model's previous version (CanESM2 - 3.67 K), and the highest sensitivity of all current models participating in the sixth phase of the coupled model inter-comparison project (CMIP6). Here, we explore the underlying causes behind CanESM5's increased ECS via comparison of forcing and feedbacks between CanESM2 and CanESM5. We find only modest differences in radiative forcing as a response to CO_2 between model versions. We find small increases in the surface albedo and longwave cloud feedback, as well as a substantial increase in

the SW cloud feedback in CanESM5. Through the use of cloud area fraction output and cloud radiative kernels, we find that more positive low and non-low shortwave cloud feedbacks— particularly with regards to low clouds across the equatorial Pacific, as well as sub/extratropical free troposphere cloud optical depth— are the dominant contributors to CanESM5's increased climate sensitivity. Additional simulations with prescribed sea surface temperatures reveal that the spatial pattern of surface temperature change exerts controls on the magnitude and spatial distribution of low cloud fraction response, but does not fully explain the increased ECS in CanESM5. The results from CanESM5 are consistent with increased ECS in several other CMIP6 models, which has been primarily attributed to changes in shortwave cloud feedbacks.

2.2 Introduction

ECS, defined as the global, annual mean surface warming the Earth would exhibit as a response to a doubling of CO_2, is a frequently cited emergent property from simplified climate models (Charney et al., 1979), as well as modern Earth system models (Andrews et al., 2012; Vial et al., 2013). The first estimates of ECS from two Earth system models ranged from 2.0 - 3.5 K (Charney et al., 1979). In the latest phase of the Coupled Model Inter-comparison Project (CMIP6), the range of ECS from participating models has widened (1.8 - 5.5 K), with the mean shifting towards higher values than the previous phase of CMIP (3.2 to 3.7 K from CMIP5 to CMIP6) (Flynn and Mauritsen, 2020; Zelinka et al., 2020). Inter-model spread of ECS is primarily attributed to radiative feedbacks on the climate system- specifically with regards to cloud feedbacks, which are the primary source of spread across models (Caldwell et al., 2016; Vial et al., 2013; Dufresne and Bony, 2008).

Understanding cloud feedback uncertainty and its influence on the ECS of ESMs has been an imperative of researchers in recent decades- particularly with regards to properties such as cloud optical depth, which determine the amount of reflected SW radiation and thus help cool the planet (Vial et al., 2013; Tan et al., 2016; Zelinka et al., 2020; Bjordal et al., 2020). SW cloud feedbacks can be separated based on latitude; middle latitude SW cloud feedbacks are mostly negative from the optical thickening of clouds due to phase transition towards liquid in ice/mixed phase clouds (Goosse et al., 2018; Senior and Ingram, 1989). In high latitudes, sea ice loss exposes the ocean surface and increases surface turbulent fluxes, and therefore humidity, which increases low level cloudiness (Goosse et al., 2018). In low latitudes, the SW cloud feedback is robustly positive in both ESMs and large eddy simulations (LES), owing to a reduction in the fraction and thickness of marine shallow cumulus and stratocumulus clouds near the PBL (Bretherton and Blossey, 2014; Bretherton et al., 2013; Ceppi et al., 2017). The physical mechanisms behind SW low cloud feedbacks are tied to multiple thermodynamic, radiative, and dynamical processes- termed cloud controlling factor (CCF) (Klein et al., 2017). Specifically, mechanisms favoring an increase in low cloud fraction in baseline climatology regimes include stronger PBL temperature inversions (Wood and Bretherton, 2006; Klein and Hartmann, 1993; Bretherton et al., 2013), colder sea surface temperatures (SST) (Bretherton and Blossey, 2014), less subsidence (Blossey et al., 2013), and increased free troposphere humidity (Van der Dussen et al., 2015).

While the sensitivity of marine low cloud cover (LCC) to specific factors varies significantly from model to model, differing sensitivities to SSTs have been identified as a explanatory factor for spread across ESMs (Qu et al., 2014). This link suggests the spatial pattern of surface warming has important implications for low cloud responses (Rose et al., 2014; Zhou et al., 2015), and therefore the SW cloud feedback and climate sensitivity

(Andrews and Webb, 2018).

Here, we investigate the causes of increased climate sensitivity in the newest version of the Canadian Earth System Model (CanESM), which is the highest of all models currently participating in CMIP6 (Flynn and Mauritsen, 2020). We examine CanESM5's high ECS particularly in relation to the previous model version that was contributed to CMIP5 (CanESM2). With a particular focus on decomposed cloud feedbacks, we quantify the differences in both forcing and feedback between CanESM2 and CanESM5 in order to establish a physical link for the shift in ECS. Lastly, we examine the spatial pattern of warming in CanESM5 and its influence of both global mean and local cloud feedbacks as a potential explanatory variable for CanESM5's high ECS.

2.3 Methods

2.3.1 Models

We compare two versions of CanESM in this study. CanESM2, the second generation earth system model from the Canadian Centre for Climate Modeling and Analysis (CCCma), consists of their fourth generation atmosphere model (CanAM4), land surface model (CLASS), terrestrial carbon model (CTEM), CSM ocean model from the National Centre for Atmosphere Research (NCAR), and ocean carbon model (CMOC) (von Salzen et al., 2013; Arora et al., 2009; Zahariev et al., 2008; Arora et al., 2011; Gent et al., 1998). CanESM5 (Swart et al., 2019), is the newest generation of the Canadian Earth System Model, uses an updated version of CLASS (version 2.7 to 3.6.2) (Verseghy, 2000), CanNEMO for the ocean model, which is based on NEMO3.4.1 (Madec, 2012), and Louvain-la-Neuve sea ice model (LIM2) (Fichefet and Maqueda, 1997; Bouillon et al., 2009).

The fifth generation atmospheric model (CanAM5) has the same horizontal resolution as CanAM4 while increasing the vertical layers from 35 to 49 with majority of the additional layers added to the upper troposphere and lower stratosphere. While there are a number of improvements to radiative transfer, aerosol, and surface parameterization, changes to cloud parameterizations are discussed briefly given their direct potential connection to cloud feedbacks. Ice cloud parameterizations in CanAM5 largely remain as in CanAM4 (von Salzen et al., 2013) with the exception of adjustments to uncertain parameters. For liquid clouds, the primary change is autoconversion of cloud liquid to rain in CanAM5, which now uses the parameterization of Wood (2005) instead of the parameterization of Khairoutdinov and Kogan (2000) which was used in CanAM4. The change in autoconversion parameterization includes the second indirect aerosol effect— a process not considered in CanAM4 (von Salzen et al., 2013).

2.3.2 Forcing-Feedback Analysis

We consider energy balance at Earth's TOA using the following equation:

$$N = F + \lambda \Delta T_s \tag{2.1}$$

Where N is net radiation imbalance (in Wm^{-2}), F is the ERF due to that of an external agent (e.g. CO_2, in Wm^{-2}), ΔT_s is the global, annual mean surface air temperature response (in Kelvin), and λ is the net Climate Feedback Parameter (in $Wm^{-2}K^{-1}$). Equation 2.1 assumes a linear relationship between radiation imbalance and surface temperature response (i.e. a constant λ). Under this assumption, an earth system model with a stronger (more negative) λ term will reestablish energy balance with a smaller surface temperature response than a weak λ term. We calculate the net feedback parameter using pre-industrial

control and abrupt-4xCO_2 experiments for each version of CanESM. For CanESM2, we use 150 years of pre-industrial control and abrupt 4xCO_2 coupled model output submitted to the Earth System Grid Federation under run 1, initialization 1, and physics 1 (r1i1p1) (Taylor et al., 2012). For CanESM5, we use the same experiments submitted for the core CMIP6 experiment deck under run 1, initialization 1, physics 2, forcing 1 (r1i1f1p2) (Eyring et al., 2016).

The surface temperature response after the system has reached equilibrium ($N = 0$ Wm^{-2}) is defined as the Equilibrium Climate Sensitivity, which is typically measured under a 2xCO_2 ERF ($ECS = -F/\lambda$). We use the term "Effective" above, as opposed to "Equilibrium" Climate Sensitivity, given the linear assumptions in Equation 2.1, where Equilibrium Climate Sensitivity is representative of warming once the system as reached true equilibrium and does not require any form of statistical extrapolation (Knutti et al., 2017). The extent that the linear approximation accurately represents both forcing and feedback varies from model to model, where some models exhibit a more linear response to CO_2 than others (Andrews et al., 2012). A time varying net feedback parameter has been- at least partially- attributable to differences in model timescale and magnitude of "rapid adjustments" in the climate system, where quick tropospheric climate response to CO_2 modifies TOA energy balance (Smith et al., 2018; Forster et al., 2013; Sherwood et al., 2015).

We consider the influence of rapid adjustments by diagnosing the ERF using two distinct methods. First, we use an ordinary least squares linear regression between TOA radiation imbalance (N) and surface temperature response (ΔT_s) in abrupt 4xCO_2 experiments, where the extrapolated y-intercept of the regression line equals 2x the ERF (ERF_g, Gregory et al. (2004)). Second, we use 30 year fixed sea surface temperature experiments (piClim-control and piClim-4xCO_2) submitted to the Radiative Forcing Model Inter-comparison

Project (RFMIP) (Pincus et al., 2016). The ERF is calculated as the TOA radiation delta in 30 year annual mean fixed sea surface temperature experiments (ERF_h), where one experiment uses pre-industrial control CO_2 and the other uses abrupt 4xCO_2 (Hansen et al., 2005; Pincus et al., 2016). Under the ERF_h definition, both tropospheric and stratospheric rapid adjustments from clouds, air temperature, water vapour, and surface albedo are included along with CO_2.

Using the Gregory regression method, we obtain the net feedback parameter as the slope of the regression line. Furthermore, we quantify the ECS for an abrupt 2xCO_2 forcing as the extrapolated x-intercept of the regression line divided by two. We consider the net feedback parameter as the linear sum of individual radiative feedbacks within the climate system:

$$\lambda = \lambda_p + \lambda_{lr} + \lambda_{wv} + \lambda_a + \lambda_c + R_e \tag{2.2}$$

Where the net feedback parameter is made up of contributions from the Planck (λ_p), lapse rate (λ_{lr}), water vapour (λ_{wv}), surface albedo (λ_a), and cloud (λ_c) feedbacks. A residual term is also included (R_e) in order to account for nonlinearities. We use a combination of the radiative kernel and Gregory regression methods to diagnose individual radiative feedbacks (Block and Mauritsen, 2013; Soden and Held, 2006). Specifically, we use six sets of radiative kernels to calculate TOA fluxes for temperature, water vapour, and surface albedo responses (Soden et al., 2008; Block and Mauritsen, 2013; Shell et al., 2008; Pendergrass et al., 2018; Huang et al., 2017; Smith, 2018). Then, each flux is linearly regressed against global, annual mean surface air temperature response for 150 years, where the slope of the regression line is considered the feedback value (in $Wm^{-2}K^{-1}$). We use the clear sky linearity test to validate the accuracy of each radiative kernel (Shell et al., 2008), where the sum of all clear sky feedbacks is compared against the net clear sky climate feedback parameter as estimated using the Gregory regression technique with clear sky TOA

flux. Three radiative kernels passed the clear sky linearity test (relative errors of less than 10%) (Figure A.1), which are used to calculate an ensemble kernel mean for all feedbacks. The three sets of kernels that passed the clear sky linearity test are derived from: the Geophysical Fluid Dynamics Laboratory (GFDL) ESM (Soden et al., 2008), the Hadley Centre Global Environment Model (HadGEM) (Smith, 2018), and from a combination of the ERA-interim reanalysis data set and the Rapid Radiative Transfer Model (RRTM) (Huang et al., 2017).

2.3.3 Cloud Feedbacks

Cloud feedbacks cannot be calculated via the standard radiative kernel method due to nonlinearities associated with cloud vertical overlap (Soden et al., 2008). We estimate cloud feedbacks using two methods- the adjusted cloud radiative effect (CRE) and cloud radiative kernel method. The CRE response is defined as the difference between clear and total sky radiative fluxes. We adjust the CRE for the effects of environmental masking from other feedbacks using clear sky radiative kernels (Soden et al., 2004). The CRE 'adjustment' using clear sky radiative kernels takes into account differences in temperature and water vapour between a clear and cloudy atmosphere to isolate the radiative perturbation from clouds. We also account for the masking effect of CO_2 forcing by using a globally uniform proportionality constant of 1.16 between clear and total sky CO_2 forcing (Chung and Soden, 2015). After adjusting the CRE, the cloud flux response is regressed similarly to noncloud feedbacks, where the slope of the regression line equals the cloud feedback. This method is performed twice to yield a value for both the SW and LW cloud feedbacks.

We use cloud radiative kernels and cloud area fraction output from the International Satellite Cloud Climatology Project (ISCCP), produced from the Cloud Object Simulator

Package (COSP) (Bodas-Salcedo et al., 2011) in CanESM2 and CanESM5, to diagnose cloud feedbacks for different cloud top pressures and optical depths (Zelinka et al., 2012a). Specifically, we calculate a cloud area fraction response, relative to a pre-industrial control climatology, for every year, grid point, optical depth, and cloud top pressure bin for each year in the abrupt 4xCO_2 simulation. Then, cloud radiative kernels are applied to the cloud area fraction response to derive TOA flux perturbations. Similar to noncloud feedbacks, each point is then linearly regressed against global, annual mean surface air temperature response over 150 years, where the slope of the regression line is equal to the feedback value.

In this study, we consider low clouds as having their tops $\geq$ 680 hPa and non-low clouds with tops $\leq$ 680 hPa. A key limitation of COSP output is the potential obscuring of low clouds via shift in the distribution of high cloud fraction (Zelinka et al., 2018). We account for the obscuring of low clouds via normalizing low cloud fraction by upper level clear-sky fraction as in Scott et al. (2020). Using this method, non-obscured low cloud responses are weighted by the area fraction not covered by high clouds.

To further separate cloud feedbacks into contributions from cloud altitude, optical depth, and amount components, we utilize the refined decomposition technique as in Zelinka et al. (2016). Using this method, cloud kernels are decomposed into individual components for cloud amount, optical depth, altitude, and residuals, while cloud area fraction anomalies are resolved into contributions from altitude/optical depth shifts and total amount separately. For a full mathematical breakdown of this decomposition, see Appendix B in Zelinka et al. (2013) and the supplemental information document from Zelinka et al. (2016).

For CanESM2, only 40 years of cloud area fraction data (years 1-20 & 120-140) were available in the abrupt-4xCO_2 simulation. To test the impact of sample size on our results,

we subsample the output from the CanESM5 abrupt-4xCO_2 simulation for the same time periods as are available from CanESM2 (years 1-20 & 120-140) and find highly similar results to those obtained from the full 150 years (Figure A.2). Furthermore, we find very similar results for LW and SW cloud feedback components from CanESM2 and CanESM5 computed using the radiative kernel method and the adjusted-CRE method (Figure A.3). This provides confidence that both methods are accurately capturing the pattern and magnitude of cloud feedbacks in these models.

2.4 Results

2.4.1 Effective Climate Sensitivity & Radiative Forcing

We begin by quantifying net feedback, forcing, and ECS for CanESM2 and CanESM5 (Figure 2.1a). Relative to CanESM2, CanESM5 has a weaker net feedback parameter (-0.64 $Wm^{-2}K^{-1}$) and higher ECS (5.65 K), meaning that ECS has increased by 54% between CanESM version 2 and 5. For comparison, we also show the model range of ECS for both CMIP5 and 6 using horizontal lines below the x-axis in Figure 2.1a, illustrating the high ECS in CanESM5 relative to all other CMIP6 models (Flynn and Mauritsen, 2020). Both versions of CanESM exhibit a strong linear relationship between surface air temperature and net TOA flux (correlation coefficients are 0.92 and 0.95 for CanESM2 and CanESM5, respectively). For some ESMs, the influence of a time-varying climate feedback parameter, which could be roughly separated into a "fast response" period in the first few decades and a weaker (less negative) feedback over the latter century, had a significant influence on model's ECS values calculated via the Gregory technique (Andrews et al., 2015). Here, the strong linearity for both versions of CanESM suggests any lack of robustness in the

Gregory technique is not a primary cause of the ECS increase in CanESM5.

We now turn to the different components of the forcing-feedback framework to elucidate any changes in either forcing, or feedback, and their influence on ECS. We compare the ERF for CanESM2 and CanESM5 via two methods. The ERF_g is determined by the y-intercept of the Gregory regression plots (filled in circles on the y-axis in Figure 2.1a). The ERF_g is 7.21 and 7.54 Wm^{-2} for CanESM2 and 5, respectively. For comparison, we also show the ERF_h as estimated using fixed-SST simulations submitted to RFMIP (open squares). The ERF_h is 7.34 for CanESM2 and 7.60 Wm^{-2} for CanESM5. Both methods produce very similar estimates of ERF— within ± 5%— which strongly suggests that the change in ECS between CanESM2 and 5 is not explained by a change in radiative forcing. However, it is worth noting that we do not investigate the role of the land surface response in the fixed-SST experiments and its impact on the ERF. Given only the SSTs are fixed, some of the warming over land is aliased into the ERF_h values for both CanESM2 and CanESM5. Still, the results here show that, even if there is a substantial difference in land surface warming between model versions in the RFMIP experiments, the ERF is still largely unchanged from CanESM2 to CanESM5. We next decompose the net feedback parameter for both models to elucidate the any potential differences in the strength of radiative feedbacks.

2.4.2 Radiative Feedbacks

Planck, lapse rate, water vapour, surface albedo, and cloud TOA feedbacks are shown in Figure 2.1b. Planck and lapse rate plus water vapour feedbacks are roughly equal between CanESM2 and CanESM5. The surface albedo feedback is more positive in CanESM5, showing an increase of 0.05 $Wm^{-2}K^{-1}$ over CanESM2, which is primarily due sea ice loss

over the Arctic (Swart et al., 2019), as well as a consistently more positive snow albedo feedback over polar land surfaces (not shown).

Lastly, cloud feedbacks increase in CanESM5— primarily in the SW; the result is a more positive net cloud feedback (+0.34 $Wm^{-2}K^{-1}$ relative to CanESM2). The net feedback (sum of all individual feedbacks) is also shown in Figure 2.1b to demonstrate the strong agreement the sum of kernel derived net feedback parameter (filled circles) and the net feedback parameter obtained from the Gregory regression technique (filled triangles). Strong agreement between both methods indicate that kernel ensemble mean is accurately capturing the extent of net TOA flux perturbation as outputted directly from the models.

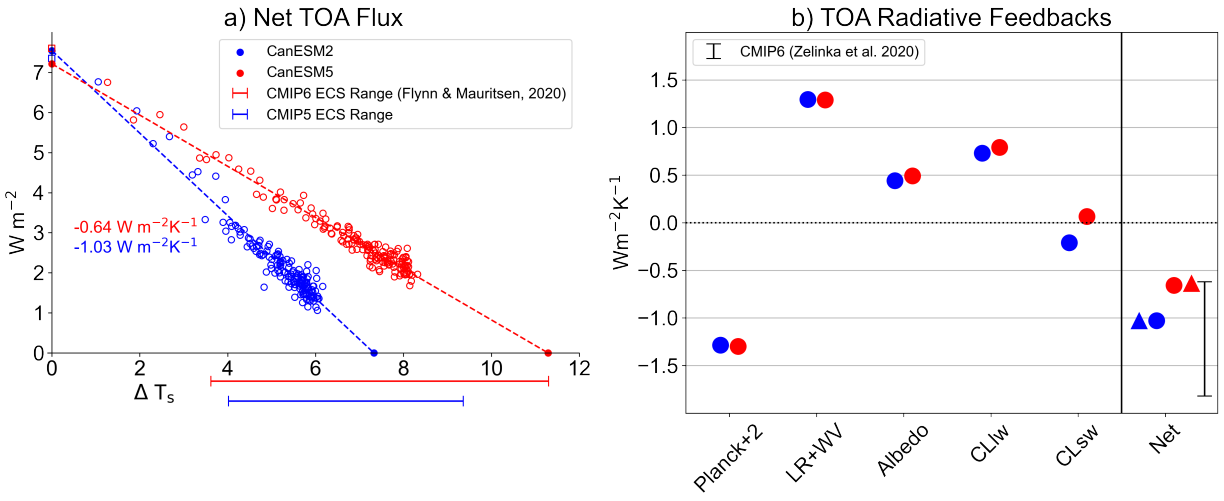

Figure 2.1: a) Net TOA radiation plotted against global, annual mean surface air temperature change in abrupt-4xCO2 simulations for CanESM2 (blue) and CanESM5 (red). Standard 150 year Gregory regressions using net top-of-atmosphere radiative flux (adjusted by a preindustrial 150 year annual mean control climate) are conducted, where the x-axis intercept of the regression line divided by two is defined as the ECS, and the y-axis intercept is defined as the ERF. For comparison, the ERF, as calculated using fixed SST AMIP style runs, is shown for both versions of CanESM via the open squares along the y-axis. Bars below the x-axis denote the model range x2 for ECS for both CMIP5 & CMIP6 (Flynn and Mauritsen, 2020). b) Global, annual mean top of atmosphere radiative feedbacks calculated using radiative kernels (in Wm^{-2}K^{-1}). From left to right, feedbacks are listed as Planck+2 (a value of 2 was added for display purposes to better illustrate differences in the other feedbacks), lapse rate plus water vapour, surface albedo, cloud, and net feedback. For comparison, we also show the net climate feedback value obtained using the standard Gregory regression approach (filled triangles), as well as the CMIP6 model range (Zelinka et al., 2020)

We find our results in line with literature assessing causes behind similar increases in ECS observed by many modelling centres participating in CMIP5 and CMIP6 (Flynn and Mauritsen, 2020; Zelinka et al., 2020; Gettelman et al., 2019; Andrews et al., 2019; Golaz et al., 2019). The LW cloud feedback is positive for both versions of CanESM— increasing by 0.06 Wm^{-2}K^{-1} from CanESM2 to 5 (Figure 2.1b). CanESM2 exhibits a negative SW cloud feedback (-0.21 Wm^{-2}K^{-1}), while in CanESM5 the SW cloud feedback has become

weakly positive (0.06 $Wm^{-2}K^{-1}$), indicating an absolute difference of 0.27 $Wm^{-2}K^{-1}$ (Figure 2.1b).

We quantify each individual feedback and forcing change (in terms of ECS increase) in Table 2.1. While the SW cloud feedback exhibits the largest difference between CanESM2 and CanESM5, both the surface albedo feedback and the LW cloud feedback offer non-negligible contributions to CanESM5's high ECS. The SW cloud feedback is the cause of at least half of the ECS increase from CanESM2 to CanESM5 (1.08 K), followed by the LW cloud and surface albedo feedbacks, respectively. Notably, There is a 3% error between the kernel ensemble-derived and model ECS values (Figure A.1). As a result, we do not consider the small contributions from the Planck, and lapse rate + water vapour changes as they are close to these error bounds (Table 2.1). Furthermore, despite the strong linear relationship between net TOA radiation and global, annual mean surface air temperature response for both version of CanESM (Figure 2.1a), the regression derived ERF model difference is opposite sign of the ERF difference calculated from fixed-SST experiments (Figure 2.1a).

Given the importance of the cloud feedback in explaining the change in ECS from CanESM2 to 5, we devote the rest of this article to investigating the causes of this change by further decomposing both the SW and LW cloud feedbacks into their altitude, optical depth, and amount components. Although the change in net LW cloud feedback is small, we will demonstrate in the following section that this is due to compensating differences in individual components.

Table 2.1: Contributions of each component in the forcing-feedback framework to CanESM5's increased ECS (in kelvin). Individual contributions from feedbacks were calculated by substituting in feedback values from CanESM5 into CanESM2 and recalculating ECS, then taking the difference between CanESM5's ECS and the recalculated ECS. Relative contributions in parenthesis are defined as the percentage of each value of the difference between CanESM5 and CanESM2s ECS (1.98 K). This process was repeated for all individual feedbacks, as well as the ERF.

ERF	Planck	LR + WV	Surface Albedo	LW Cloud	SW Cloud
-0.08	0.04	0.08	0.34	0.39	1.08
(-4.59 %)	(1.96 %)	(3.85 %)	(17.30 %)	(19.8 %)	(54.38 %)

Decomposition

The SW cloud feedback arises due to changes in cloud amount and/or optical properties. Cloud optical thickness is dependent on water path and cloud droplet size distribution (Slingo, 1989). The phase composition of clouds (liquid, ice, or mixed) is linked strongly to their optical thickness due to liquid droplets and ice crystals having different characteristic size distributions, where clouds composed of predominantly smaller liquid droplets tend to be more reflective (Pruppacher and Klett, 1980). As a result, regions where cloud composition consists entirely of liquid droplets, or are mixed phase, tend to exhibit higher albedo. In terms of feedbacks, cloud phase and amount changes have been identified as an explanatory factor to ECS spread in ESMs (Tan et al., 2016; Zelinka et al., 2016). Thus, we now decompose the cloud feedbacks using cloud radiative kernels and ISCCP simulator output for each version of CanESM following the methods described in Zelinka et al. (2012a,b) to investigate individual cloud feedback processes. We apply the decomposition

separately to low and non-low clouds.

In Figure 2.2, we decompose LW and SW cloud feedbacks into contributions from changes in cloud optical depth, cloud altitude, and cloud amount. The LW total cloud feedback is dominated by contributions from non-low clouds (Figure 2.2a), with small negative contributions from low clouds (Figure 2.2b). Changes in cloud optical depth or amount have little radiative influence for low clouds given low cloud top temperatures are close to that of the surface, resulting in similar outgoing longwave radiation (i.e. little greenhouse effect). Furthermore, particularly for CanESM2, the strong non-low LW feedback is largely offset by a negative SW feedback of comparable magnitude. For CanESM2, contributions to the LW feedback are comparable for optical depth and amount feedbacks—with largest contribution coming from altitude. The altitude feedback arises from cloud temperature dependent emission properties, and therefore operates predominantly in the longwave for non-low clouds. Tropical free troposphere clouds rise and maintain cooler cloud top temperatures relative to the surface, thereby becoming more efficient at trapping outgoing longwave radiation (Zelinka and Hartmann, 2010; Gettelman and Sherwood, 2016). For CanESM5, the net non-low LW feedback is approximately equal to CanESM2, albeit with a different decomposition makeup. Specifically, CanESM5 has a more positive LW altitude and optical depth feedback. However, these increases are offset by a weaker cloud amount feedback. For low clouds, the LW feedbacks are all small in magnitude. The residuals (yellow) are similarly small in both models (Figure 2.2), indicating that nonlinear processes are less important for understanding the changes between models.

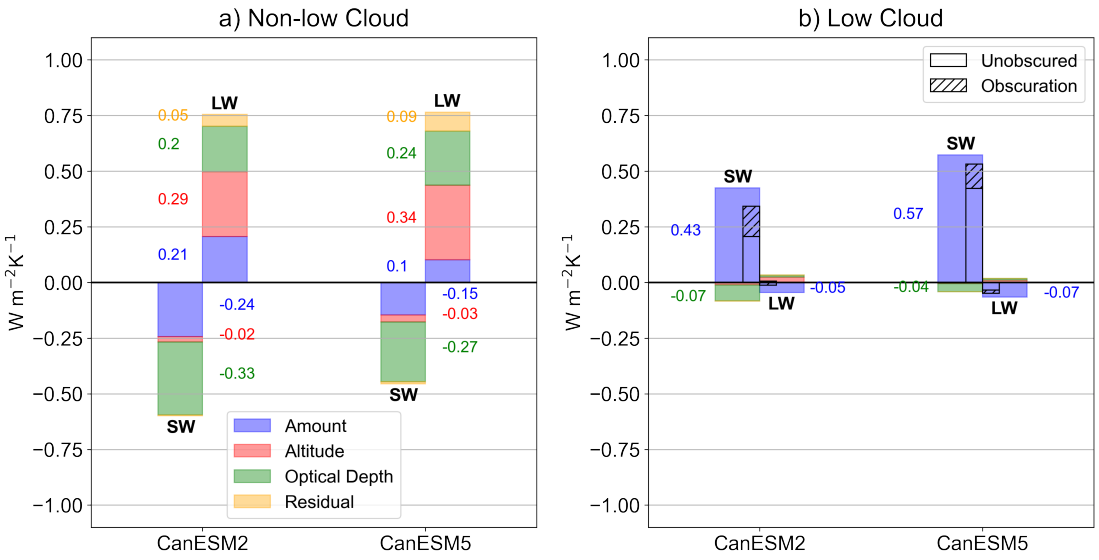

Figure 2.2: Global, annual mean decomposed cloud feedbacks for CanESM2 & CanESM5. Feedbacks are partitioned into both LW and SW contributions from cloud amount (blue), cloud altitude (red), optical depth (green), and residual (orange) terms, for non-low (panel a) and low clouds (panel b). Low cloud feedbacks are also separated via non-obscured and obscuration terms in black bars in panel b. For contributions smaller than 0.01 Wm^{-2}K^{-1}, text values were omitted for the sake of clarity.

In the SW, both models exhibit strong negative feedbacks for non-low clouds and strong positive feedbacks for low clouds (Figure 2.2). The negative non-low cloud shortwave feedback is driven by an increase in cloud amount and optical depth with warming. This result is consistent with both modelling and theoretical understanding of non-low cloud responses to warming. Specifically, an increasing number of liquid droplets relative to ice crystals gives rise to more mixed phase clouds, as well as increases the proportion of liquid to ice in existing mixed phase clouds, resulting in an higher optical depth (Senior and Ingram, 1989), and a positive relationship between mid latitude cloud liquid water content and the slope of the moist adiabat as the troposphere warms (i.e. a function of temperature) (Betts, 1987). For low clouds, the SW is dominated by a strong positive amount feedback

(decrease in cloudiness), with a small negative contribution from optical depth feedback (increase in cloud optical depth) (Figure 2.2b). For CanESM5, SW feedbacks differ from CanESM2 considerably for both non-low and low clouds. For non-low clouds, CanESM5's optical depth feedback is weaker (less negative) than CanESM2 (+0.06 $Wm^{-2}K^{-1}$) (Figure 2.2a). While the SW non-low cloud amount feedback is also weaker in CanESM5, the difference is offset in the LW. For low clouds, the SW amount feedback exhibits the largest difference between the two model versions (+0.14 $Wm^{-2}K^{-1}$). The change in SW cloud feedback strength and sign between CanESM2 and CanESM5 is related to multiple feedback mechanisms operating at different cloud heights. The largest contributor is the SW low cloud amount feedback, which is more positive in CanESM5. Changes in optical depth feedbacks are mainly important for non-low clouds, and are less negative in CanESM5.

The large difference in SW low cloud feedback strength between CanESM2 and CanESM5 raises the possibility that a portion of what the COSP interprets as a low cloud response is actually the result of changes in the spatial distribution of non-low cloud fraction under climate change; a phenomenon known as 'obscuration' (Zelinka et al., 2018). Separating for obscuration does not also separate out the amount and optical depth feedbacks. Therefore, we consider the SW unobscured low cloud feedback as combination of changes in proportional cloud amount and optical depth. The black bars in Figure 2.2b indicate the both CanESM2 and CanESM5 have a non-negligible obscuration term. However, given that the extent of obscuration is similar between both versions of CanESM (see hatched bars in Figure 2.2b), it does not appear to be a major contributor to increased feedback strength in CanESM5 relative to CanESM2.

Spatial Distribution

Low cloud amount feedbacks are considered a robust positive feedback mechanism diagnosed from both observational and modelling studies, albeit with substantial inter-model spread in terms of strength (Eitzen et al., 2011; Clement et al., 2009; Zelinka et al., 2016). The low cloud amount feedback is closely tied to the distribution of marine stratiform cloud regimes persisting in the sub/tropics over ocean eastern boundary current regions (Klein et al., 2017). The non-low cloud optical depth feedback has been shown to have rich- and sometimes offsetting- spatial structure, owing to mostly negative feedback mid/high latitudes and a rich zonal structure at low latitudes (Zelinka et al., 2012b, 2016). As such, we now examine the spatial distribution of both the SW low cloud amount and non-low cloud optical depth feedbacks (Figure 2.3).

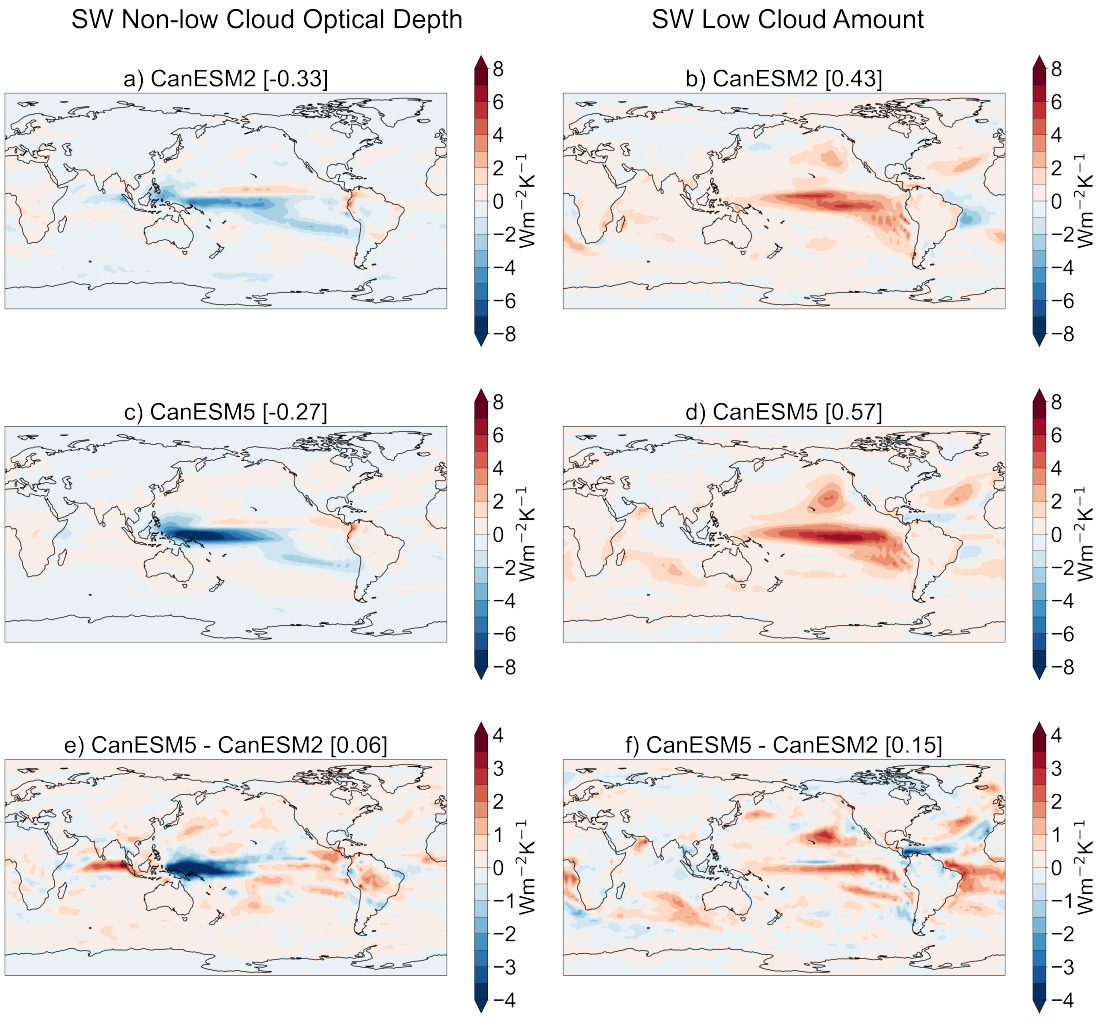

Figure 2.3: Annual mean SW non-low cloud optical depth (left) and SW low cloud amount (right) feedbacks for CanESM2 (panels a & b) and CanESM5 (panels c & d). Panels e & f show the difference between CanESM5 & CanESM2 for each respective feedback. Values in square brackets next to each subplot title denote the global mean value for each respective map. Note the difference in colour bar scales for top and bottom/middle panels.

Figure 2.3 shows annual mean SW non-low cloud optical depth and low cloud amount feedbacks for CanESM2 and CanESM5. The SW non-low cloud optical depth feedback is negative in CanESM2 & 5 (Figure 2.3a and c), with minima over the western tropical

Pacific Ocean. For the SW low cloud amount feedback, both models are strongest over subtropical/tropical Eastern Ocean basins and across the equatorial Pacific (Figure 2.3b and d). Notably, these regions have persistent low, stratiform cloud regimes, which are closely tied to strong temperature inversions that cap the PBL (Klein and Hartmann, 1993).

For CanESM5, increases in SW non-low cloud optical depth feedback are exhibited throughout the subtropical Pacific and tropical Eastern Pacific Ocean (Figure 2.3e). While there is strong positive feedback over the Eastern Indian Ocean and negative feedback over the Western Pacific Ocean, it is offset by a similar strength and opposing sign in the LW (not shown), and so it does not exert a major influence on the global mean net cloud feedback (LW+SW). For SW low cloud amount feedback, CanESM5 exhibits an increase over CanESM2 in every region of persistent low cloud cover regimes, as well as across the eastern equatorial Pacific and the western ocean basin off the Brazilian coast, relating to the simulation of substantially reduced LCC under a warming climate (Figure 2.3f).

Multiple lines of evidence from modelling studies have linked the sensitivity of LCC over the oceans to local changes in SST (Zhou et al., 2017; Andrews and Webb, 2018). Furthermore, the evolving spatial pattern of surface warming from interannual to centennial time scales is associated with differences between interannual and long term cloud feedback strength (Zhou et al., 2015). The underlying physical mechanisms linking local sea surface warming to reduced LCC are: 1) increased surface latent heat flux dries and deepens the boundary layer via increased buoyancy-driven turbulence and resultant downward mixing from free troposphere air (Qu et al., 2015; Rieck et al., 2012), and 2) increased surface specific humidity promotes further moisture contrast between the boundary layer and the free troposphere such that when air is mixed downward it is relatively drier (Van der Dussen et al., 2015; Qu et al., 2015). We use a proxy term, $SST^{\#}$, as a measure of

distribution of surface warming in the tropics (Figure 2.4) (Fueglistaler, 2019). Specifically, SST$^{\#}$ is calculated as difference between the warmest 30% of tropical SSTs (i.e. the Indo-Pacific) and the tropical average, and therefore provides quantitative information about zonal asymmetries in the tropical SST pattern and how they evolve over time.

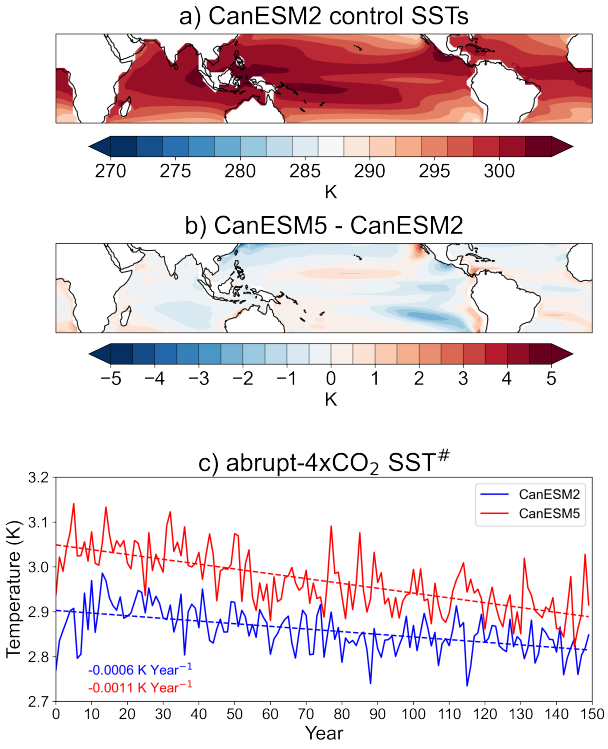

Figure 2.4: a) Pre-industrial Control mean (150 years) tropical SSTs for CanESM2. b) Pre-industrial Control mean (150 years) tropical SSTs for CanESM5, expressed as a difference relative to CanESM2. c) Annual mean time series of SST$^{\#}$ for both CanESM2 and CanESM5 for abrupt-4xCO_2 experiments.

The Pre-industrial control tropical SST pattern for CanESM2 is shown in Figure 2.4a, and exhibits a familiar zonally-asymmetric pattern with the warmest SSTs in the Indo-Pacific, and cooler waters in the east Pacific and southeastern regions of each ocean basin. Relative to CanESM2, CanESM5's control SSTs are substantially cooler— up to 3 K—

over the eastern tropical Pacific (Figure 2.4b). Colder SSTs are also prevalent in the northern Pacific, off of the western Australian coast, and the northern tropical Atlantic ocean (Figure 2.4b). There is little difference between the SSTs in the Indo-Pacific, which has important implications for $SST^{\#}$. Figure 2.4c shows a time series of $SST^{\#}$ for abrupt-4xCO_2 experiments. Given $SST^{\#}$ represents the difference between the warmest waters in tropics relative to the average, a higher value indicates greater asymmetry between warmer and cooler regions of tropical SST. The relatively colder waters in CanESM5's control climatology results in a larger $SST_{\#}$ term, which is also illustrated at the beginning of the abrupt-4xCO_2 timeseries (Figure 2.4c). The difference between the models decreases as the climate warms in response to CO_2. The higher $SST^{\#}$ term at the beginning of the simulation in CanESM5 suggests a stronger SW CRE in the pre-industrial control (Fueglistaler, 2019). The strong positive SW cloud feedback in CanESM5, particularly from low clouds, warms the eastern Pacific (and other cooler areas) at a faster rate than CanESM2 (Figure 2.3f), which gradually decreases the difference in $SST^{\#}$ over the course of the abrupt-4xCO_2 simulation (Figure 2.4c). While the distribution of surface warming in the tropics is known to be important for low clouds (Andrews and Webb, 2018), we also briefly analyse another important controlling factor: estimated inversion strength (EIS) (Figure 2.5).

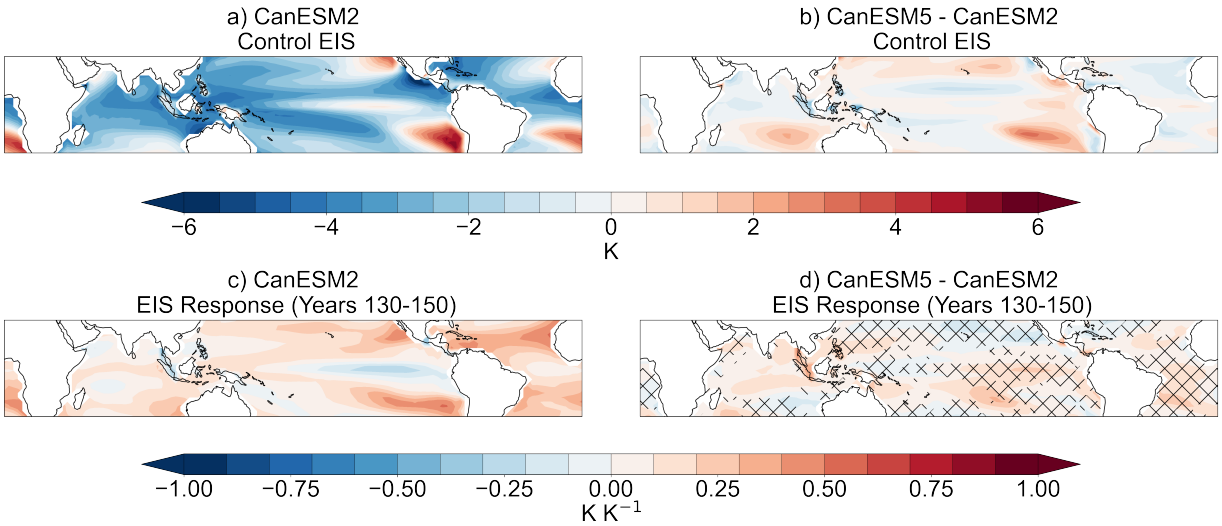

Figure 2.5: a) Annual mean control climatology (150 year mean) tropical EIS for CanESM2. b) Annual mean control climatology (150 year mean) tropical EIS for CanESM5, expressed as a difference relative to CanESM2. c) Tropical EIS response (years 130-150 mean) for CanESM2. d) Tropical EIS response (years 130-150 mean) for CanESM5, expressed as a difference relative to CanESM2's response. For EIS responses, each grid box value is normalized by the global mean surface air temperature response (also years 130-150 mean relative to the control period). for Hatching represents areas where the SW low cloud feedback is more positive in CanESM5.

Figure 2.5 shows EIS for both the control climatology and response abrupt-4xCO_2 simulations, and is calculated using air temperatures at the surface and 700hPa as in Wood and Bretherton (2006). Regions with a strong positive EIS are indicative of a boundary layer that is decoupled from the free troposphere, with strong subsidence and cooler SSTs, and therefore more low cloud fraction. Conversely, a strong negative EIS is indicative of a weak inversion and a surface that is coupled tightly to the free troposhere (i.e. unstable vertical temperature profile), and is therefore inefficient at trapping moisture within the boundary layer. In the CanESM2 control period, EIS is strongly positive across all eastern ocean basins and the eastern equatorial Pacific (Figure 2.5a). In CanESM5, control EIS mirrors the corresponding SST pattern (Figure 2.5b, 2.4b). In the response period, EIS increases

throughout most of the tropics for both models (Figure 2.5c & d). CanESM5 exhibits a stronger increase in EIS throughout most of the tropics relative to CanESM2. Given that EIS and low cloud fraction are strongly positively correlated (Wood and Bretherton, 2006), a stronger response (as seen in CanESM5) would promote more cloud fraction if it were the only cloud controlling factor. However, we find no clear relationship between regions of more positive SW low cloud feedback and increased inversion strength response (Figure 2.5d). Inferring causal changes in cloud feedbacks between models from EIS alone is difficult given its correlation with SSTs (Scott et al., 2020) (see Figure 2.4b and Figure 2.5b). We now turn towards prescribed SST experiments from Cloud Feedback Model Inter-comparison Project (CFMIP) to further investigate the role of SST warming distribution as a cloud controlling factor.

2.4.3 Prescribed SST Experiments

To investigate the spatial pattern of surface warming and its influence on SW cloud feedbacks, we present results from an additional experiment from the CFMIP Tier 2 experiment deck— amip-piForcing (Webb et al., 2017). The amip-piForcing experiment forces the atmosphere model with the reconstructed historical SSTs and sea ice boundary conditions from 1870 to 2014 (Hurrell et al., 2008). An important distinction from the base amip experiment is the anthropogenic and natural atmospheric forcings are held fixed to their pre-industrial control levels in amip-piForcing, which allows for a more direct comparison to abrupt-4xCO_2 experiments, as it removes the influence of non-SST mediated cloud responses. Thus, using amip-piForcing, we can isolate the contribution to changes in cloud feedbacks that arises due to changes in the atmosphere model (CanAM4 to CanAM5) independent of the change to the ocean model (NCAR CSM to CanNEMO). We show global

mean low cloud feedbacks and SST$^{\#}$ time series for both amip-piForcing and abrupt-4xCO$_2$ CanESM5 experiments in Figure 2.6.

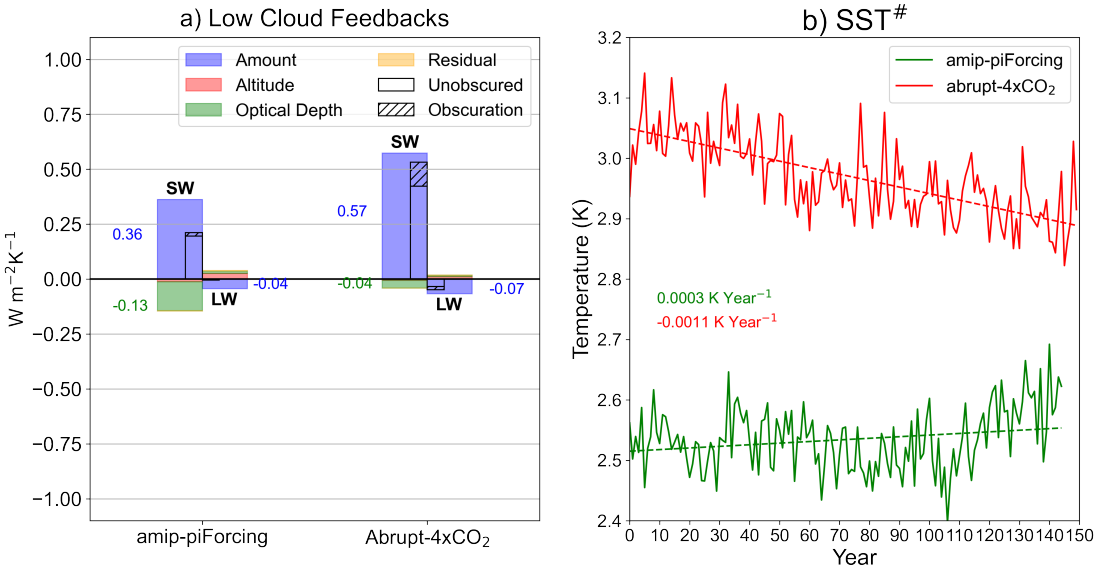

Figure 2.6: a) Global, annual mean decomposed cloud feedbacks for CanESM5's amip-piForcing and abrupt-4xCO$_2$ experiments. Feedbacks are partitioned into both LW and SW contributions from cloud amount (blue), cloud altitude (red), optical depth (green), and residual (orange) terms. Feedbacks are also separated via non-obscured and obscuration terms in black bars. For contributions smaller than 0.01 Wm^{-2}K^{-1}, text values were omitted for the sake of clarity. b) Annual mean time series of SST$^{\#}$ for both CanESM5 experiments.

For low clouds, the SW feedback is stronger (+0.21 Wm^{-2}K^{-1}) in the abrupt-4xCO$_2$ experiment than amip-piForcing— largely due to the cloud amount feedback, but with a smaller contribution from the optical depth feedback (Figure 2.6a). This result is consistent with theoretical understanding relating warmer local SSTs to reduced boundary layer marine cloud cover as outlined in the previous section, which is further emphasized by the geographic distribution of warming in the amip-piForcing experiment (Figure 2.6b). In amip-piForcing, the eastern Pacific warms only by a small amount relative to the abrupt-4xCO$_2$ experiment (Figure A.4), which is exemplified by the SST$^{\#}$ time series.

Furthermore, the SST$^{\#}$ trend is opposite in amip-piForcing, illustrating the warming in the Indo-Pacific warm pool over the historical record (Figure A.4), which is not present in coupled model abrupt-4xCO_2 experiments (Andrews et al., 2018).

We summarize feedback results from all experiments considered in this study in Table 2.2. The Planck response is nearly identical for all three experiments. The combined lapse rate and water vapour feedback is similar in abrupt-4xCO_2 experiments for both models, but noticeably more negative in the amip-piForcing experiment. The combined result is a product of the more negative lapse rate feedback, which arises due to the relatively stronger warming in the Indo-Pacific warm pool (Andrews et al., 2018) from the reconstructed SST dataset used as forcing (Hurrell et al., 2008). Surface temperatures in the deeply convective warm pool increase Earth's emission temperature via enhanced latent heat release, which stabilizes the vertical temperature profile and warms the upper troposphere. Outgoing longwave radiation increases and produces a strong radiative cooling effect. The surface albedo feedback is stronger in the CanESM5 for coupled model experiments, but reduced in amip-piForcing relative to CanESM5's abrupt-4xCO_2 experiment, which is likely a result of the constrained sea ice boundary conditions present. The longwave cloud feedback is similar across all three experiments/models, and the SW cloud feedback has strongly increased in CanESM5 for coupled experiments, but is reduced to a similar magnitude to CanESM2 abrupt-4xCO_2 in the amip-piForcing experiment. The net feedback result for the amip-piForcing experiment is strongly negative in CanESM5 relative to abrupt-4xCO_2, which is due to the combined effect of a reduced surface albedo, SW cloud, and lapse rate feedbacks.

Table 2.2: Summary of radiative feedbacks, calculated using a combined radiative kernel/regression method (adjusted-CRE in the case of the cloud feedbacks listed here) for both model version abrupt $4xCO_2$ experiments, as well as CanESM5's amip-piForcing experiment. All feedbacks are in units of $Wm^{-2}K^{-1}$. Feedbacks from the amip-piForcing run were calculated using the 1980-2010 period as a baseline

Model	Planck	LR + WV	Surface Albedo	LW Cloud	SW Cloud	Net
CanESM2 ($4xCO_2$)	-3.29	1.26	0.44	0.73	-0.21	-1.03
CanESM5 ($4xCO_2$)	-3.30	1.29	0.49	0.79	0.06	-0.66
CanESM5 (piForcing)	-3.31	0.96	0.45	0.76	-0.21	-1.35

2.5 Discussion & Conclusions

In this study, we have analysed both forcing and feedback in idealized experiments with instantaneous quadrupling of atmospheric CO_2 (abrupt-$4xCO_2$) using two versions of CanESM to elucidate the underlying cause behind CanESM5's increased ECS (5.65 K). Using radiative kernels and output from RFMIP, we find only modest differences in both forcing and non-cloud feedbacks, with a small contribution from a slight increase in the surface albedo feedback. The largest difference in feedback strength between CanESM2 to CanESM5 is from the cloud feedback, particularly in the SW. Further breakdown of the cloud feedback into its individual components (optical depth, altitude, and amount) at distinct cloud top

heights (<680 hPa for non-low, ≥680 hPa for low) revealed that the SW low cloud amount and non-low cloud optical depth feedbacks are the dominant contributor to CanESM5's increased ECS (+0.14 and 0.06 $Wm^{-2}K^{-1}$, respectively) in abrupt 4x-CO_2 simulations. Analysis of the spatial pattern for each feedback showed the largest model differences in SW low cloud amount feedback over subtropical eastern ocean basins and across the equatorial Pacific ocean, and in SW non-low optical depth feedback over the subtropical and extratropical Pacific ocean.

We analysed the spatial pattern of surface warming and its influence on the SW low cloud feedback using the CFMIP tier 2 amip-piForcing experiment in CanESM5, which exhibited significantly reduced SW cloud feedback due to the lack of local warming in regions with persistent low cloud cover— in agreement with studies linking warmer (colder) SSTs to decreased (increased) LCC (Qu et al., 2014; Bretherton and Blossey, 2014; Brient and Schneider, 2016). We found a similar strength in LW cloud feedback from both abrupt-4xCO_2 and amip-piForcing experiments, and a reduced lapse rate feedback in the amip-piForcing experiment due to the relatively stronger surface warming in the Indo-Pacific warm pool. While lacking an analogous amip-piForcing experiment for CanESM2, the results presented here agree with similar experiments conducted using other ESMs (i.e. more negative lapse rate and SW cloud feedback) that have been studied with respect to pattern effects of warming (Andrews et al., 2018). Furthermore, the SW cloud feedback strength in the CanESM2-abrupt-4xCO_2 is equal to that of the CanESM5 amip-piForcing experiment despite a different pattern effect of warming (Figure 2.4a & Figure 2.6b). The amip-piForcing results presented here confirm the well documented relationship between local SSTs as a controlling factor for low clouds. This result suggests that both the pattern of warming itself, and the sensitivity of low cloud fraction to this pattern plays a key role in CanESM5's higher ECS. Disentangling the role of the ocean model replacement (The

National Centre for Atmospheric Research CSM ocean model for CanESM2 (Gent et al., 1998) to CanNEMO for CanESM5 (Swart et al., 2019)) and the developmental changes to cloud microphysics in CanAM5 (e.g. the new autoconversion scheme and aerosol indirect effect) is a subject for future work. As a first step, an equivalent series of experiments as analyzed in this study could be ran with an intermediary development version of CanESM5 that couples CanAM5 to CanESM2's ocean model to isolate the role of CanNEMO. One could also study the role of ocean heat transport differences between the two model versions as well using a slab ocean version of CanESM5 with specified heat fluxes into the deep ocean. The role of ocean heat transport, and it how differs in CanNEMO, may be important for local changes in SSTs and thus cloud fraction (Singh et al., 2022).

Our results add further evidence the recent trend of several ESMs participating in CMIP6 exhibiting higher ECS than their CMIP5 counterpart— predominantly due to changes in SW cloud feedback strength and/or aerosol-cloud interactions (Gettelman et al., 2019; Andrews et al., 2019; Bodas-Salcedo et al., 2019). However, it is worth noting that several modelling centres report increased ECS sourced from distinct developments in newer versions of their respective model (e.g. addition of a mixed-phase cloud scheme and improved aerosol-cloud interactions, as well as the higher horizontal ocean model resolution its influence on SSTs in cold upwelling regions, in HadGEM3 (Bodas-Salcedo et al., 2019; Mulcahy et al., 2018; Andrews et al., 2019).

Finally, we emphasize that the results presented in this study do not seek to comment on the plausibility of climate sensitivity from either version of CanESM. Recently, there has been an expansion of work relating constraints on climate sensitivity through the use of the satellite and paleoclimate observational records (Sherwood et al., 2020). Furthermore, there are limitations of interpreting the validity of climate sensitivity results (as calculated here) due to uncertainties associated with statistical methods (e.g. assuming a time-invariant

climate sensitivity parameter via the regression approach) (Gregory et al., 2004). However, we reiterate the scope of this study: establishing a causal link for the increased climate sensitivity from CanESM2 to CanESM5 under long term, idealized climate change.

Chapter 3

On the Linearity of External Forcing Response in Solar Geoengineering Experiments

3.1 Overview

As an idealized proxy for solar geoengineering, the GeoMIP G1 experiment forces Earth System Models with prescribed reductions in solar radiation to balance increases in atmospheric CO_2. One key source of uncertainty is the magnitude of solar constant reduction required to offset a CO_2 quadrupling. Here, we employ single-forcing simulations with CESM to decompose the distinct radiative adjustments associated with solar and CO_2 forcing in the G1 experiment. We find that radiative adjustments to both single forcings have a net positive effect on top of atmosphere energy balance such that they both increase the net G1 forcing. Stratospheric temperature and shortwave cloud adjustments are the

main sources of positive adjustment in both Solar and 4xCO_2 simulations. We also show that net radiative adjustment in G1 cannot be represented linearly with CO_2 and solar forcing adjustments, which is primarily traced to reductions in boundary layer clouds.

3.2 Introduction

Solar radiation modification, or solar geoengineering, refers to the deliberate modification of sunlight incident upon the earth as a means of countering anthropogenic climate change. While early studies used simple models to explore the role of solar radiation as an external forcing on the climate system (Wetherald and Manabe, 1975; Hansen et al., 1997), solar geoengineering as a potential mitigating strategy against greenhouse gas induced warming is a theoretical but nascent field of research (Crutzen, 2006; Wigley, 2006; Robock, 2008). Coordinated efforts to research geoengineering using Earth System Models (ESMs) began with the GeoMIP(Kravitz et al., 2011b, 2013,b, 2015). Initially, core GeoMIP experiment design consisted of idealized experiments where the solar constant was adjusted within a given ESM to offset either instantaneous or time-evolving increases in CO_2. Solar geoengineering designs have since expanded beyond simple tuning (Latham, 1990; Alterskjær et al., 2012; Niemeier et al., 2013; Kravitz et al., 2013b; Keith et al., 2016); however, idealized experiments using direct solar constant tuning have persisted in GeoMIP due to their insights into geoengineered climates and ease of implementation.

From both a modeling and implementation standpoint, one element of uncertainty in idealized geoengineering experiments is the amount of solar constant reduction required to offset a given increase in CO_2. In the GeoMIP G1 experiment, where the solar constant is reduced to balance an abrupt quadrupling of CO_2, the inter-model spread in the required varies between 3.5-5% (Kravitz et al., 2013, 2021). For modeling groups, determining the

necessary reduction is typically achieved using a brute-force approach, where a heuristic equation is used to provide an initial guess for the globally averaged solar constant reduction:

$$ERF_{4xCO_2} = \frac{\Delta S_0 \pi r^2}{4\pi r^2}(1-\alpha), \tag{3.1}$$

where ERF_{4xCO_2} is the Effective Radiative Forcing (ERF) from a quadrupling of CO_2, r is the radius of the Earth, α is the planetary albedo, and ΔS_0 is the solar constant reduction. The solar constant is then tuned iteratively to achieve approximate top of atmosphere (TOA) energy balance closure (Kravitz et al., 2011a). The iterative approach is the result of Equation 3.1 chronically under-predicting the reduction in the solar constant needed to close the energy budget (Russotto and Ackerman, 2018), which we will eventually argue is the result of Equation 3.1 only considering radiative adjustments from one (CO_2) of the two forcings in the G1 experiment. The ERF_{4xCO_2} is calculated using the reference Abrupt 4xCO_2 experiment from the CMIP core deck.

The inter-model spread of the solar constant offset in G1 has been primarily attributed to rapid adjustments in the climate system as a response to both CO_2 increases and solar constant reductions (Russotto and Ackerman, 2018). Rapid responses in temperature, moisture, and clouds induce radiative perturbations alongside the direct IRF of a given forcing factor (e.g. $CO_{2,}$, aerosols, solar). which taken together determine the ERF (Sherwood et al., 2015).

Despite previous studies exploring rapid adjustments as a response to external agents, their role in idealized geoengineering scenarios— which involve multiple forcings on the climate system— remains unclear. Here, we decompose the rapid adjustments from both CO_2 and solar forcing in the G1 experiment using a series of single forcing experiments

with the Community Earth System Model (CESM). We show that the required offset is not easily predicted using the heuristic equation from GeoMIP because rapid adjustments as a response to negative solar forcing have a net positive radiative effect. Furthermore, we find that adjustments from CO_2 and solar forcing do not add linearly due to enhanced boundary layer cloud reduction in our G1 simulation.

3.3 Methods

3.3.1 Community Earth System Model

We employ CESM version 1.2.2 in its atmosphere & land only (or "F") component set (Hurrell et al., 2013). Specifically, the component set employed here consists of the Community Atmosphere Model 4 (CAM4) with 26 vertical levels and 4° x 5° horizontal resolution, the Community Land Model 4 (CLM4), and prescribed pre-industrial ocean and sea ice climatologies. We use CAM4 with a 4° x 5° horizontal resolution given our analysis is focused on global and zonal mean quantities, as well as for its computational efficiency. CAM4 is configured with the Cloud Object Simulator Package (COSP, Bodas-Salcedo et al. (2011)) enabled, which includes cloud diagnostics consistent with the International Satellite Cloud Climatology Project (ISCCP) (Klein and Jakob, 1999; Schiffer and Rossow, 1983). The ISCCP diagnostics include cloud fraction as a function of cloud top pressure (CTP) and optical depth (τ), which can be used with cloud radiative kernels to calculate the radiative perturbation associated with cloud responses at various heights and optical thicknesses (Zelinka et al., 2012a).

All experiments follow the Radiative Forcing Model Inter-Comparison Project (RFMIP) protocol (Pincus et al., 2016). Simulations are run for 30 years using a repeating annual

cycle of pre-industrial sea ice and sea surface climatologies as boundary conditions. All experiments with external forcings are compared to a control simulation where CO_2 and the solar constant are kept at their default pre-industrial values (Table 3.1). Following RFMIP methodology allows for direct calculation of the ERF for each experiment. This offers a distinct advantage relative to the so-called "Gregory" method, which relies on using linear regression on coupled model output in order to extrapolate the ERF (Gregory et al., 2004), and is therefore subject to drawbacks of assuming linearity in the climate response to changes global mean surface temperature (Knutti et al., 2017).

We follow the GeoMIP G1 protocol to estimate the necessary solar constant reduction needed to offset quadrupled CO_2 (Kravitz et al., 2011a) (i.e. using Equation 3.1). To quantify ERF_{4xCO_2}, we run an abrupt-4xCO_2 experiment (herein referred to as 4xCO_2) and take the difference between 30 year global mean net top of atmosphere radiation relative to a pre-industrial control experiment (Hansen et al., 2005). Planetary albedo (α) is calculated as the 30 year global mean ratio of reflected to down welling shortwave radiation at the TOA. This gives α=0.34 for 4xCO_2, and then we rearrange and solve for ΔS_0. We use the same prescribed value of ΔS_0 for solar forcing only (SOLAR) and G1 experiments, where in G1 an abrupt quadrupling of CO_2 and solar constant reduction are applied at the same time. We run two sets of SOLAR and G1 experiments— one where ΔS_0 is calculated as per Equation 3.1, and another where ΔS_0 is tuned through successive simulations to ensure global mean energy balance in G1. These experiments are referred to as the equation and balance runs, respectively (e.g. $G1_e$, and $G1_b$) (Table 3.1).

Experiment	CO_2 (ppm)	S_0 (W m^{-2})	Note
Control	284.7	1360.89	Baseline
4xCO_2	1138.8	1360.89	single forcing
$SOLAR_e$	284.7	1317.19	single forcing
$SOLAR_b$	284.7	1311.00	single forcing
$G1_e$	1138.8	1317.19	combined forcings
$G1_b$	1138.8	1311.00	combined forcings

Table 3.1: Experiments performed for this study. Subscripts e and b refer to equation and balance simulations, respectively.

3.3.2 Radiative Adjustments

We decompose the ERF in each experiment using the following equation:

$$ERF = IRF + \sum_{x}^{n} \frac{\partial R}{\partial x} dx \tag{3.2}$$

where ERF is the Effective Radiative Forcing for a given climate forcing (4xCO_2, SOLAR), IRF is the Instantaneous Radiative Forcing, and the summation term is the sum of all radiative adjustments from responses in surface albedo, temperature, water vapor, and clouds (Smith et al., 2018; Chung and Soden, 2015; Zhang and Huang, 2014). We clarify our use of the term "adjustments", as opposed to "feedbacks" to be consistent with RFMIP experiment design where all SSTs and sea ice are prescribed. The partial term ($\frac{\partial R}{\partial x}$) represents the radiative sensitivities of a given state variable (x), and dx represents the climate response in x due to the external forcing of SOLAR, 4xCO_2, and G1 relative to the Control simulation. Since G1 targets global mean TOA energy balance, the ERF_{S_0}

should be equal to the right hand side (RHS) of Equation 3.2. However, since rapid adjustments for SOLAR experiments cannot be known a priori, any residual from Equation 3.1 is a result of SOLAR or combined forcing rapid adjustments.

We quantify the ERF directly from model output as the difference of 30 year, annual mean net TOA radiation in forcing experiments relative to the Control experiment. Each non-cloud radiative adjustment is quantified using radiative kernels (Shell et al., 2008). We use the radiative kernels from Shell et al. (2008) specifically as they were computed using radiative transfer code (Community Atmosphere Radiative Transfer Model (CAMRT) Collins et al. (2004)) most similar as to the version of CESM used for this study. All radiative kernels are horizontally interpolated to 4° x 5° horizontal resolution and all climate responses are vertically interpolated to match the 17 pressure levels of the kernels (where applicable). We quantify cloud adjustments using the COSP output from CESM and cloud radiative kernels designed for use with ESMs (Zelinka et al., 2012a, 2013, 2016). Using the cloud kernel method, cloud radiative adjustments can be decomposed into contributions from both boundary layer ($\geq$ 680 hPa) and free troposphere ($<$ 680 hPa) clouds in both the longwave and shortwave[1]. Lastly, we quantify the IRF as the residual of the ERF and all radiative adjustments via rearranging the terms in Equation 3.2. Under this framework where all radiative adjustments and the ERF are explicitly quantified, we assume that any error due to nonlinearities in the energy budget decomposition (Equation 3.1) is small enough to consider negligible.

[1]See Zelinka et al. (2016) supplementary information for more methodological details

3.4 Results

3.4.1 Energy Budget Residual in G1

We begin by showing the TOA energy budget response (i.e. the ERF) for each experiment in our study. The global mean ERF for 4xCO_2 is 7.21 W m^{-2} (Figure 3.1a). Using this value, Equation 3.1 predicts a ΔS_0 of 43.70 W m^{-2} to offset the ERF_{4xCO_2}. However, the ERF for $SOLAR_e$ is -6.46 W m^{-2}, indicating that the ΔS_0 is insufficient to fully balance ERF_{4xCO_2}, and this is confirmed by the residual ERF of 0.93 W m^{-2} in the $G1_e$ experiment. While this residual is relatively small in the context of the global planetary energy budget, GeoMIP protocol requires ESMs to be within 0.1 W m^{-2} of energy balance (Kravitz et al., 2011b). That Equation 3.1 produces a positive residual in ERF (i.e. it underestimates ΔS_0 required to balance 4xCO2 forcing) is well-documented (Russotto and Ackerman, 2018), but to our knowledge has not been adequately explained by previous studies. In contrast, the ERF for $G1_b$ is 0.09 W m^{-2}, indicating the effectiveness of manually tuning ΔS_0.

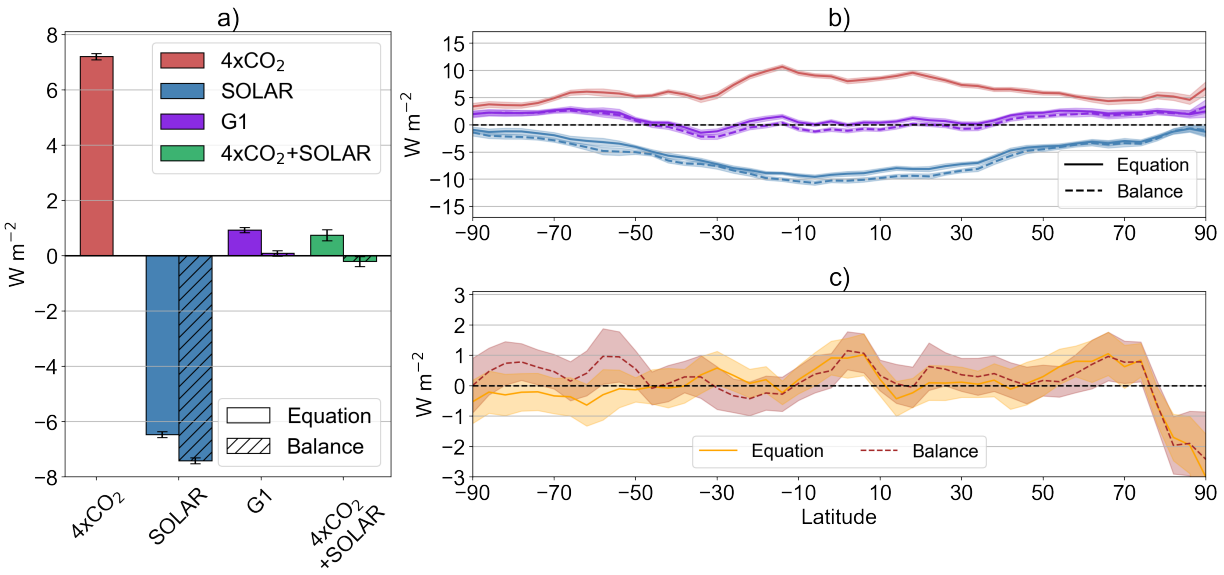

Figure 3.1: a) Global mean ERF values for SOLAR (equation and balance), 4xCO_2, and G1 (equation and balance) experiments. For comparison, we also plot the sum of SOLAR and 4xCO_2 experiments as well. Error bars denote ± 2 standard error using all 30 years for each experiment. b) The corresponding Zonal mean ERF. c) Zonal mean residual ERF between G1 and 4xCO_2+SOLAR (equation and balance) experiments. For subplots b and c, the shaded regions are calculated as in subplot a.

The remainder of this section presents the physical evidence for why this imbalance in ERF exists. The first piece of evidence comes from the meridional structure of ERF in response to 4xCO_2 and SOLAR forcing. For 4xCO_2, ERF peaks in the tropics and decreases toward the poles (Figure 3.1b), in line with previous studies linking its meridional structure to the Planck response of warmer emission temperatures (Zhang and Huang, 2014). The SOLAR ERF is strongest (more negative) over the tropics and weakest (more positive) near the poles, which arises from the tropics receiving the largest fraction of insolation globally and thus the largest fractional decrease as a result of ΔS_0. In $G1_e$ the ERF is near zero throughout the tropics, whereas in $G1_b$ it is slightly negative. From the extratropics to the poles, both G1 experiments are have a positive residual ERF (Figure 3.1b).

Given that ERF takes into account all radiative adjustments from temperature, surface albedo, water vapour, and clouds, it is insufficient as a stand alone metric to assess linearity between single versus combined forcing experiments. For both SOLAR and the $4xCO_2$ experiments specifically, differences in both sign and magnitude of radiative adjustments have been linked to residual positive forcing in GeoMIP G1 experiments (Russotto and Ackerman, 2018). To understand what drives the nonlinearity in the response, we now present the decomposition of ERF into the IRF and its individual radiative adjustments.

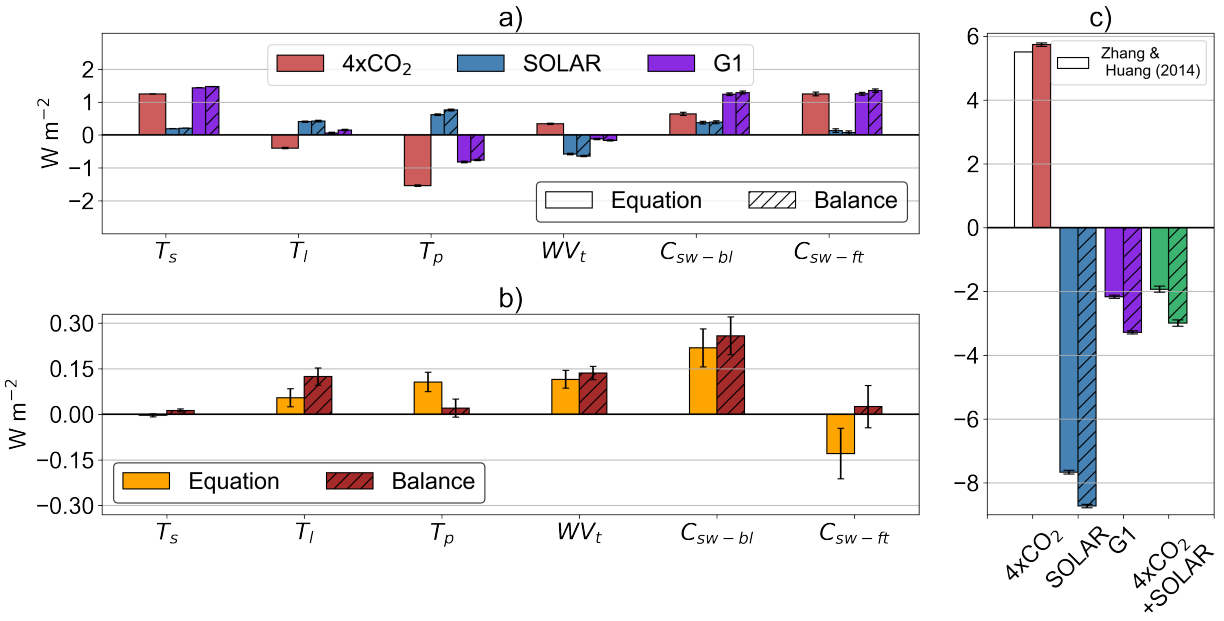

Figure 3.2: Global, annual mean non-zero radiative adjustments for a) $4xCO_2$, SOLAR, and G1 experiments. Both equation and balance experiments are also presented for SOLAR and G1. b) Residual between the G1 experiment and the combined $4xCO_2$+SOLAR experiment output. From left to right, adjustments are listed as stratosphere temperature (T_s), lapse rate $T_{(l)}$, Planck (T_p), troposphere water vapour (WV_t) shortwave boundary layer cloud ($C_{sw\text{-}bl}$), shortwave free troposphere cloud ($C_{sw\text{-}ft}$). A table with all adjustments can be found in the supplementary information document (Table S1). c) Corresponding Global mean IRF. We also show the IRF for $4xCO_2$ as calculated in Zhang and Huang (2014) for comparison. The IRF for Error bars for all three subplots are calculated as in Figure 3.1.

In terms of magnitude, the biggest contributions to both G1 experiments are from adjustments that are positive in both $4xCO_2$ and SOLAR (Figure 3.2a). On a per adjustment basis, both equation and balance experiments are of similar sign and magnitude. The net radiative adjustment for $G1_e$ and $G1_b$ is 3.10 W m^{-2} and 3.37 W m^{-2}, respectively. In both cases, this is explained primarily by positive adjustments from stratospheric temperature and both boundary layer and free troposphere clouds in the SW, and partially offset by a negative Planck adjustment (Figure 3.2a). The net G1 adjustment illustrates the importance of including rapid responses here with respect to achieving energy balance, as the $G1_e$ ERF is only slightly positive (0.93 W m^{-2}, Figure 3.1a) and would thus be substantially more negative without rapid adjustments. By construction, the Planck adjustment is entirely explained by land surface air temperature changes because SSTs and sea ice boundary conditions remain fixed. The land surface warms in G1 and $4xCO_2$, and cools in both SOLAR experiments (Figure S1). The stratospheric temperature adjustment is positive due to radiative cooling in both single forcing experiments, a result that has been consistently observed across modelling studies (Wang and Huang, 2020; Chung and Soden, 2015; Hansen et al., 2005; Manabe and Wetherald, 1975). The SW cloud adjustments are partitioned into boundary layer and free troposphere components, both of which are positive for $4xCO_2$ and SOLAR experiments, indicating widespread reduction in cloud amount and/or optical depth throughout the troposphere. Conversely, LW cloud adjustments are near zero across all experiments and both cloud top distinctions. The contrast between longwave and shortwave cloud adjustments is linked to the fixed SSTs in all experiments, where SW heating from cloud fraction reduction is primarily linked to fast responses after a forcing agent has been introduced, while LW heating is mostly surface temperature mediated (Zelinka et al., 2013). Given our experiments hold SSTs fixed, the longwave effect of cloud adjustments is near zero (Table S1).

Positive adjustments in both 4xCO_2 and SOLAR experiments highlight why Equation 3.1 often under predicts the ΔS_0 offset to balance increased CO_2. Adjustments positively affect the IRF for 4xCO_2 and SOLAR experiments, but not in equal amounts. Equation 3.1 only considers adjustments from CO_2, not adjustments for the solar constant reduction or potential non-linear interactions between the combined forcings. This result is also supported by the global mean IRF for both 4xCO_2 and $SOLAR_e$. In $G1_e$, the negative instantaneous forcing (-2.17 W m^{-2}) is the result of all adjustments from 4xCO_2 (+1.47 W m^{-2}, Figure 3.2a) being factored into Equation 3.1, which necessitates a greater reduction in the solar constant and thus a more negative $SOLAR_e$ instantaneous radiative forcing (Figure 3.2c).

3.4.2 Non-linear Responses to Combined Forcings

Finally, we quantify radiative adjustments associated with non-linear responses to 4xCO_2 and both SOLAR experiments. Computing the sum of the responses of SOLAR and 4xCO_2 provides a useful baseline to quantify non-linearities against their respective G1 experiment. Any residual in the energy budget is, by construction, a product of feedbacks in the climate response that cause radiative adjustments and further perturb the energy budget in G1. We refer to any difference between $G1_x$ and 4xCO_2+$SOLAR_x$ with prime notation. The global mean $ERF_e^{'}$ and $ERF_b^{'}$ are 0.19 W m^{-2} and 0.29 W m^{-2}, respectively (Figure 3.1a).

In general, G1 residuals are small, but positive, for most rapid adjustments (Figure 3.2b). $C_{sw-bl}^{'}$ is the largest for both $G1_e$ (0.22 W m^{-2}) and $G1_b$ (0.26 W m^{-2}). The only negative residual is for $C_{sw-ft}^{'}$ in $G1_e$, which is not statistically different than zero for $G1_b$. Both the inter-annual uncertainty, and the discrepancy between equation and balance

experiments are largest for the C'_{sw-ft}, reiterating that clouds contribute a major part of the signal, but also a considerable proportion of the noise. The net $G1'_e$ adjustment is 0.43 W m^{-2}, or 13.8% of the net $G1_e$ adjustment. For $G1'_b$, the net adjustment is 0.58 W m^{-2}, or 17.1% of the total $G1_b$ adjustment.

For $G1_e$ and $G1_b$, total cloud radiative adjustments are dominated by 4xCO_2, with responses from SOLAR primarily limited to boundary layer clouds (Figure 3.2a). We further break down the cloud fraction response by showing the ISCCP simulator output for both $G1_e$ and $G1_b$ in Figure 3.3. The ISCCP simulator provides cloud fraction on seven CTP and τ bins for every gridbox, where each CTP-τ bin corresponds to cloud fraction at a given height and optical thickness. In line with their radiative adjustments, both $G1_e$ and $G1_b$ have statistically significant reductions optically thick clouds throughout the troposphere, with the largest reductions in CTP bins ¡680 hPa (Figure 3.3a and b). Cloud fraction increases near the tropical tropopause (Figure S4); however, given these increases are confined to optically thin bins (Figure 3.3a), the global mean LW adjustment is near zero (Table S1). There is a potential compensatory effect as well due to free troposphere cloud fraction being defined here as below 680 hPa. Any potential decrease in upwelling OLR from tropical cirrus cloud response would be offset by the decreases in cloud fraction in the 680-310 hPa CTP bins.

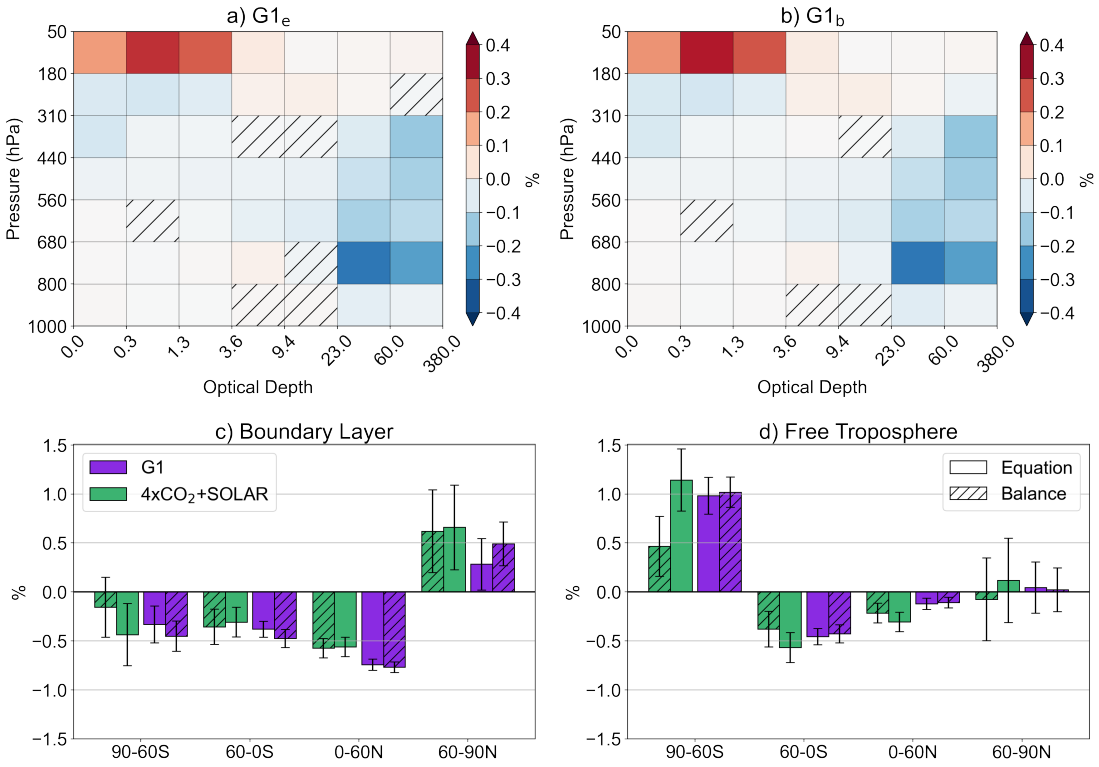

Figure 3.3: a & b) Global, annual mean ISCCP simulator cloud fraction response (in %) for $G1_e$ and $G1_b$, respectively. As with all other figures, responses are calculated as 30 year means. The y and x-axes represent seven cloud top pressure pressure (hPa) and optical depth (τ, dimensionless) bins with labels at bin edges. τ-CTP bins without hatching represent statistically significant differences between the G1 simulations and the Control simulation, calculated using all 60 available simulation years with a two tailed Student's t-test (p ¡ 0.05). c). Zonal mean boundary layer cloud fraction response (in %) binned into four different latitude bands for $G1_e$, $G1_b$, $4xCO_2$+$SOLAR_e$, and $4xCO_2$+$SOLAR_b$ experiments. Error bars represent ± 2 standard error of the mean. d) As in c), but for free troposphere cloud fraction,

For both G1 experiments, boundary layer cloud fraction decreases across all latitude bands except the Arctic (Figure 3.3c). $G1_b$ exhibits the largest decrease over $G1_e$ predominantly in the southern hemisphere. For free troposphere clouds, reductions in optically thick clouds are confined to 60S-60N (Figure 3.3b and d). Over the Antarctic, both $G1_e$ and $G1_b$ experiments show an increase in cloud fraction near the tropopause and a decrease

of near the surface. This is tied to the Antarctic vertical temperature profile response. In G1 experiments, the boundary layer and surface warm but the upper troposphere cools (Figure S2d and b). The cooling upper troposphere has a destabilizing effect on the boundary layer below, enhancing upward mixing and reducing cloud fraction (Salvi et al., 2021). The result is likely compounded by a limitation of ISCCP simulator output, where its top down perspective can miss changes in low cloud fraction due to overlying obscuration (Zelinka et al., 2018). Since Antarctic free troposphere cloud increases in G1, the ISCCP simulator may show a decrease in boundary layer cloud fraction solely due to changes in the overlying amount or spatial distribution. The temperature profile response itself is linked to the combined cooling and heating profiles of both a negative solar and positive CO_2 forcing (Henry and Merlis, 2020). In both $G1_e$ and $G1_b$, the increased LW absorption from CO_2 produces pronounced warming in the boundary layer, whereas reduced solar forcing produces vertically homogeneous cooling (Figure S2b and c). Notably, the Arctic cloud fraction response differs from the Antarctic by a relatively smaller increase in boundary layer cloud fraction and little change in the free troposphere, albeit with substantial interannual uncertainty (Figure 3.3d). The mid to upper troposphere warms in the Arctic, which may offset the destabilizing effect of near surface warming.

The magnitude and sign of cloud adjustments to external forcings is a large source of uncertainty across ESMs (Smith et al., 2020a). While these results are from a single model, they qualitatively agree with results assessing multi-model ensemble cloud adjustments as a response to increased CO_2 (Kamae and Watanabe, 2012). Our results also show that the free troposphere cloud response in G1 is dominated by the CO_2 forcing as opposed to solar forcing (Figure 3.2a).

3.5 Discussion and Conclusions

In this study, we have decomposed the top of atmosphere energy budget in a series of fixed-SST, single and multi-forcing experiments using CESM to clarify the role of rapid adjustments in an idealized geoengineering scenario. The total rapid adjustment increases the IRF for both $4xCO_2$ and SOLAR forcing experiments. In the context of the G1 experiment with $4xCO_2$ and SOLAR forcing combined, this reduces the impact of the solar constant offset, which necessitates a stronger reduction than predicted by Equation 3.1. A decomposition of radiative adjustments in G1 reveals a non-linear effect that accounts for 13%-17% of the total adjustment, amplifying the SW cloud adjustment through further reductions in boundary layer clouds. This result can be attributed to three distinct physical drivers. As LW heating caused by the CO_2 IRF dries the lower free troposphere, relatively drier air is mixed downward from aloft to decrease optically thick boundary layer clouds (Figure S3) (Kamae and Watanabe, 2012). This effect is slightly dampened by free troposphere warming, which acts to increase lower tropospheric stability (Salvi et al., 2021). However, if a negative solar forcing is applied in conjunction with CO_2 forcing, the free troposphere exhibits less warming and the compensatory stabilizing effect is removed, which amplifies boundary layer cloud reduction. Decomposing the low cloud response in G1 experiments into contributions from cloud controlling factors may offer further insight (Scott et al., 2020; Klein et al., 2017; Qu et al., 2015), but such work is beyond the scope of this study.

From a modeling perspective, our results illustrate the difficulty in achieving energy budget closure at the top of atmosphere for G1 via a trial and error approach. While rapid adjustments in $SOLAR_e$ and $SOLAR_b$ are qualitatively similar in this study, they vary as a function of the initial offset. If one were to run a solar forcing only experiment to

quantify the net radiative adjustment as done here, which could then be factored back into Equation 3.1, it would not consider the relationship between the magnitude of adjustments relative to the solar constant offset. Moreover, our results presented here are from a single ESM, and the magnitude of solar forcing rapid adjustments likely varies from model to model (Smith et al., 2018).

An intuitive next step would be to assess the role of rapid adjustments in more applicable geoengineering scenarios using stratospheric aerosol injections to offset multiple external forcings (e.g. the G6 sulfur scenario). Solar dimming experiments do not wholly capture modeled responses from aerosol injections, particularly with regards to atmospheric chemistry and dynamics (Visioni et al., 2021a). Results from GeoMIP6 transient scenarios show that fully coupled ESMs exhibit similar globally averaged surface responses regardless of whether or not external forcings are applied smoothly or as a once per decade step function (Visioni et al., 2021b). Nevertheless, decomposing rapid adjustments to individual forcings in transient geoengineering scenarios could reveal regional climate responses and underlying non-linear physical drivers as shown here.

Complications for modeling centres notwithstanding, these results exemplify the need for further research on rapid adjustments in geoengineering scenarios, particularly for ones with real world applicability as it will be an integral component in quantifying both geoengineering effectiveness (in terms of energy budget or surface temperature based objectives) and near term impacts (in terms of rapid climate response).

Chapter 4

Declining Geoengineering Efficacy Caused by Cloud Feedbacks in Transient Solar Dimming Experiments

4.1 Overview

Solar geoengineering with injections of aerosols into the stratosphere has emerged as a research area of focus with the potential to cool the planet. However, the amount of solar geoengineering required to achieve a given level of cooling, and how this relationship evolves in response to increasing greenhouse gas emissions, remains unclear. Here, we explore the evolution of solar geoengineering efficacy over time under an idealized forcing framework. Using Earth System Model simulations that dynamically adjust the amount

of insolation to offset global mean warming from increasing CO_2, we find that decreases in global planetary albedo diminish the efficacy of a solar geoengineering proxy of dimming the sun. Physically, the decrease in albedo is primarily driven by reductions in optically thick tropical cloud fraction in the boundary layer and mid troposphere, which are driven by a drying and destabilization of the mid to lower troposphere. These results reaffirm the need to understand the troposphere response, particularly from clouds, in realizable solar geoengineering experiments and their potential to feed back onto planetary albedo, thus impacting the solar geoengineering effectiveness.

4.2 Introduction

The current best estimate of observed historical global mean surface warming relative to the preindustrial era is 1.0-1.25° C (2022-2013 average) (IPCC, 2023). As temperatures continue to increase in the wake of Paris Agreement goals of limiting global warming to 1.5° C and 2.0° C, research into emergency climate intervention strategies, or geoengineering, has grown over the past two decades (Crutzen, 2006; Wigley, 2006; Keith and MacMartin, 2015; Robock, 2008). SAG has been studied more intensively than other proposed geoengineering methods as volcanic eruptions have provided as useful analogue to illustrate the cooling effect at the surface of sulphate aerosols in the stratosphere (Stenchikov et al., 1998), and research surrounding its implementation (Davidson et al., 2012), cost per year (Smith and Wagner, 2018), achievable targets from use (Kravitz et al., 2017), adverse impacts (Robock, 2008), and governance (McLaren and Corry, 2021) have progressed over the past decade. However, despite the rapid evolution of geoengineering research, outstanding questions remain on SAG effectiveness, unaccounted climate impacts, and what international governance would look like (Kravitz and MacMartin, 2020).

Coordinated efforts to compare ESM simulations of geoengineering, such as the Geoengineering Model Inter-comparison Project (GeoMIP), have enabled multi-model comparisons of several experiment designs that range from idealized solar constant tuning simulations to Shared Socioeconomic Pathways (SSP) simulations with SAG to dampen surface warming (Kravitz et al., 2011b, 2013). However, the complexity of SAG experiment designs from GeoMIP has partially contributed to the smaller number of ensemble members for GeoMIP experiments relative to other MIPs. For example, 6 ESMs participated in the G6sulfur experiment with the target of reducing surface warming from SSP5-8.5 down to the medium forcing SSP2-4.5 experiment (Kravitz et al., 2015). Of these 6 models, Visioni et al. (2021b) found an inter-model spread of 29±9-Tg of SO_2 per year between 2081-2100 needed to meet G6sulfur specifications, where some models with prognostic treatment of stratospheric aerosols injected SO_2 near the equator and others scaled aerosol optical depth (AOD). The inter-model spread of SAG in the G6sulfur experiment is representative of *geoengineering efficiency* (GE), or the radiative forcing (in W m^{-2}) per injected Tg of SO_2. In the stratosphere alone, inter-model spread of SAG efficiency is physically driven by differences in model treatment of dynamics, chemistry, and aerosol microphysics (Visioni et al., 2021a). Therefore, simplified experiment designs where the solar constant is tuned within ESMs (e.g., the G6solar experiment) provide a valuable proxy for SAG to explore geoengineering efficacy from the perspective of surface and troposphere response while controlling for differences in model treatment of aerosols. Solar tuning experiments were included in all iterations of GeoMIP (Kravitz et al., 2011b, 2015). Outside of geoengineering model inter-comparison efforts, the efficacy of solar forcing has been explored relative to that of CO_2 to further understand the roles of various forcing agents on the climate system (Hansen et al., 2005; Kaur et al., 2023; Wetherald and Manabe, 1975; Modak et al., 2016).

The use of a forcing-feedback framework has become conventional to separate the Ef-

fective Radiative Forcing (ERF) from a particular forcing agent from surface radiative feedbacks (Gregory et al., 2004; Andrews et al., 2012). The ERF is defined as the sum of both the instantaneous forcing (IRF) from introducing a forcing agent (e.g., dimming the solar constant by 4%) as well as the "radiative adjustments" of the climate after the forcing agent is introduced but prior to the relatively slower surface response (Sherwood et al., 2015). From the perspective of geoengineering, understanding the physical drivers of differences between solar and CO_2 forcing efficacy informs the effectiveness of proposed strategies (Russotto and Ackerman, 2018; Smith et al., 2018; Virgin and Fletcher, 2022). In particular, the use of transient simulations where solar and CO_2 forcing efficacy evolve over time could inform the source of inter-model spread in more realizable geoengineering experiment designs like SAG.

Here, we investigate the evolution of geoengineering efficacy over time in an idealized experiment framework. Specifically, we explore the physical drivers behind changes in planetary albedo in transient solar dimming experiments, and how such drivers potentially feed back onto the global Top of Atmosphere (TOA) energy budget, thus impacting the efficacy of reducing the solar constant over time against increasing concentrations of CO_2. Finally, we discuss the limitations of this approach and whether or not this form of analyses can be extrapolated to experiment designs with SAG as opposed to solar constant tuning.

4.3 Methods

4.3.1 Community Earth System Model

We use version 1.2.2 of the Community Earth System Model (CESM) for all experiments in this study (Hurrell et al., 2013). All experiments use the Community Atmosphere Model

version 4 (CAM4) with an eulerian dynamical core at T31 horizontal resolution (3.75° latitude/longitude gridboxes) with 26 vertical levels (Gent et al., 2011). CAM4 is built with the Cloud Object Simulator Project (COSP) enabled to produce extra cloud diagnostics from the International Satellite Cloud Climatology Project (ISCPP) simulator (Bodas-Salcedo et al., 2011; Klein and Jakob, 1999; Schiffer and Rossow, 1983). We use CAM4 at this resolution for its computational efficiency, and note that a similar configuration has been used successfully to study global climate responses to perturbed cloud and aerosol microphysics (Fletcher et al., 2018, 2022). Furthermore, given that we tune the solar constant as a proxy for geoengineering and that our analysis primarily focuses on the surface and troposphere response, stratospheric chemistry and prognostic aerosol treatment are not essential for this work. However, we acknowledge that the use of an older model configuration means that caution must be used when attempting to generalize these results to newer ESMs. The remainder of the component set consists of the Community Land Model version 4 (CLM4) with biogeochemical cycling active (Lawrence et al., 2011), the Parallel Ocean Program 2 (POP2) for coupled simulations at 3° horizontal resolution (Smith et al., 2010), the Community Ice CodE Model (CICE) model (Hunke and Lipscomb, 2008), the River Transport Model (RTM), and stub components for the land ice and ocean wave models.

4.3.2 Experiment Design

First, we run a coupled, 100 year pre-industrial control experiment (CTL) which all subsequent experiments are branched from (Table 4.1). To quantify the ERF and radiative adjustments for large changes in CO_2 and the solar constant (S_0), we follow the Radiative Forcing Model Inter-comparison Project (RFMIP) protocol (Pincus et al., 2016). We

extract the monthly mean sea surface temperatures (SST) and sea ice forcing files from year 100 of CTL, which are used as repeating climatologies for all subsequent atmosphere and land only experiments. To quantify a baseline for perturbed experiments, we run a 30 year fixed SST and sea ice control experiment (CTL_f) using the year 100 CTL sea ice and SST's repeating annually. Perturbed CO_2 ($4xCO_{2(f)}$) and solar constant (SOL_f) experiments use the same SST and sea ice forcing files as CTL_f in order to isolate the atmosphere response to each forcing. $4xCO_{2(f)}$ quadruples CO_2 concentration and SOL_f reduces the solar constant by 4%.

Using a single year as opposed to a climatological mean to create SST and sea ice forcing files means that the boundary forcing represents one particular realization of inter-annual variability from the CTL experiment. However, we tested the impact on the results of using a multi year climatology to create forcing files and the primary conclusions were unchanged. Furthermore, we stress that the SSTs and sea ice are identical between the baseline and perturbed experiments. The decision to use year 100 was to ensure consistency with the coupled experiments and to constrain the PI controller in the first year of the GEO experiment. Since the controller uses annual means to calculate the temperature error each year, specifying a climatological temperature as the target would produce a synthetic "error" in the first year of GEO through the eyes of the controller even though the warming signal from increases in CO_2 would likely not have arisen. This is, admittedly, a choice we made to reduce the drawbacks of using a controller that responds to interannual variability. Specifically, the GEO experiment targets the global, year 100 annual mean surface air temperature of the CTL experiment by adjusting the solar constant each year using a control system (See Subsection 4.3.3).

Experiment	CO_2 (ppm)	S_0 (W m^{-2})	Length (years)	Note
CTL	284.7	1360.89	100	coupled equilibration run
SI	284.7	±1% amplitude sin wave	140	branched from CTL, system identification run for controller
1%CO_2	+1%CO_2 yr^{-1} (linear)	1360.89	140	branched from CTL
GEO	+1%CO_2 yr^{-1} (linear)	time varying	140	branched from CTL, S_0 dictated by controller
CTL_f	284.7	1360.89	30	fixed year 100 repeating CTL SST's and sea ice
$4xCO_{2(f)}$	1138.8	1360.89	30	CTL_f sea ice & SST's
SOL_f	284.7	1306.45	30	CTL_f sea ice & SST's

Table 4.1: Experiments performed for this study. Note that experiments with a subscript "f" denote experiments with fixed SSTs and sea ice derived from year 100 of the CTL experiment.

We run two coupled experiments with time varying forcings that both branch off of year 100 of CTL and run for 140 years. In "1%CO2", concentration increases each year by 1% of the pre-industrial CO2 concentration to a terminal value of 686.19 parts per million

(ppm) by the end of the experiment. GEO uses the same CO_2 forcing as 1%CO_2, but uses a proportional-integral (PI) controller to dynamically adjust the solar constant every year to suppress changes in global mean surface air temperature. We use a 1%CO_2 forcing in GEO as it is time varying and therefore more analogous to a real world emissions pathway. Lastly, in order to quantify the gain parameters for the PI controller, we run a 140 year System identification (SI) experiment forced by a time varying S_0 sinusoid. The detailed methodology of the SI experiment and PI controller implementation is expanded in the following section.

4.3.3 Control System Design

We use a PI controller to manage the solar constant as a proxy for geoengineering in the GEO experiment (Kravitz et al., 2016):

$$\Delta\ S_0(t) = -k_p T_e(t) - k_i \sum_{n=0}^{t} T_e(n) \tag{4.1}$$

Where $\Delta\ S_0$ is the change in the solar constant (in percent), k_p is the proportional gain term (in % K^{-1}), T_e is the temperature error relative to the target baseline, k_i is the integral gain term (in % K^{-1} $year^{-1}$) and the final RHS side term is the integrated temperature error since the beginning of the run. Equation 4.1 is shown in discrete time here given the controller readjusts the solar constant at the end of each year.

As illustrated by Virgin and Fletcher (2022), the magnitude of radiative adjustments as a response to both CO_2 and solar forcing directly influence TOA energy balance and thus the efficacy of any prescribed reduction in S_0 designed to suppress a GHG-forced temperature response. For idealized, instantaneous (step function) CO_2 forcing, it is possible

to quantify radiative adjustments first and factor them into the required solar constant offset calculation, which is the suggested approach for GeoMIP G1 experiments (Kravitz et al., 2011a,b). However, this is impractical and subject to large uncertainty because the total radiative adjustment contribution to the ERF of a prescribed solar forcing varies as a function of the forcing itself (Virgin and Fletcher, 2022). This problem is also present for coupled simulations with time varying CO_2 forcing, where any prescribed reduction in S_0 would need to consider radiative adjustments as a response both the ΔS_0 and +1% CO_2 for a given year, as well as the current climate state (e.g., lapse rate, cloud fraction distribution) that would impact the instantaneous radiative forcing (IRF) efficacy.

To mitigate against this problem, we configure the coupled simulation to target a specific surface air temperature as opposed to TOA energy balance using a PI controller (Kravitz et al., 2016; Tilmes et al., 2018; Kravitz et al., 2014). We follow the detailed methodology in Kravitz et al. (2016) to optimize the controller performance in GEO. Specifically, we target a global, annual mean surface air temperature of 284.63 K, which is the year 100 value at the end of the CTL simulation. At the end of each year, we calculate the global, annual mean surface air temperature error relative to the target, as well as the integrated error since the experiment start ($n = 0$). Then, Equation 4.1 is used to calculate ΔS_0, which is a percentage change in the solar constant relative to the CAM4 default value of 1360.89 W m^{-2}.

The choice of k_i and k_p vary from system to system. In our use case of simulating idealized geoengineering using CESM, picking gain values that accurately represent the system requires understanding both the magnitude and timescale of the model surface temperature response to a perturbation in S_0. As shown in MacMartin et al. (2014), system identification (SI) simulations are used to quantify the magnitude and timescale of the response at various frequencies. The SI experiment S_0 and surface air temperature

response for CESM 1.2.2 is shown in Figure 4.1. We use a S_0 forcing sinusoid with an amplitude of $\pm 1\%$ and a period of 16 years, corresponding to an angular frequency of approximately 0.39 radians year^{-1}.

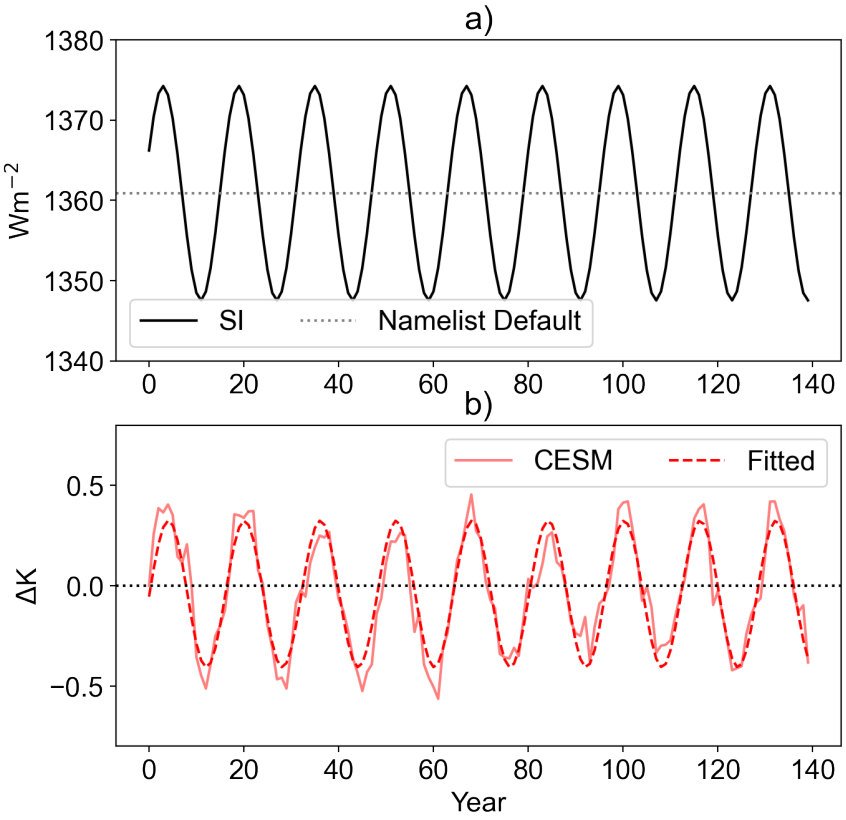

Figure 4.1: a) Solar constant time series used in the SI experiment for proportional-integral controller parameter calculation. The sinusoid has an amplitude of 1% and a period 16 years. b) The global, annual mean surface air temperature response from CESM in the SI experiment and the corresponding sinusoidal fit.

Figure 4.1b shows that the surface air temperature response is also a sinusoid, indicating the relationship between surface temperature and a unit perturbation in S_0 is sufficiently linear at this frequency. In practice, the linearity of this relationship will also depend on interannual variability, the frequency of the forcing, and underlying basic state. Since the

controller only considers the portion of the output that is linearly related to the input, this represents an important limitation of the approach. However, as we will show later, the controller is effective at suppressing the surface temperature response without amplifying natural variability despite such limitations.

Following Kravitz et al. (2016), we quantify the magnitude of the response using the S_0 forcing and a sinusoidal fit of the surface air temperature response. The magnitude of the *system* response (M) at 0.39 radians year^{-1} is calculated as the ratio of amplitudes between the input and output. The timescale of the response is quantified by the phase lag of the *system* response (Φ), which is the difference in phase between the output and the input (Table 4.2). Φ quantifies the effect of time lag between the input signal (solar constant change here) and the output response (surface temperature change) at this particular frequency, where climate models with greater phase lag have a longer detection window after a forcing has been applied. Both the input and output in the SI simulation are sinusoidal (Figure 4.1), so we can quantify the detection window by taking the difference between each curve's phase. In practice with model ensembles, the inter-model spread in phase lag would be the result of the timescale and magnitude of radiative adjustments as a response to the input signal.

Lastly, we also quantify the effect of time lag as well (Φ_t). Since the controller uses annual means, the information used at the end of each year is on average half a year old. Furthermore, since the controller will hold S_0 constant for a full year before updating again, another half year of lag is introduced. At 0.39 radians year^{-1}, Φ_t=22.50°.

variable	value
M	0.37 K $\%^{-1}$
Φ	25.57°
Φ_t	22.50°
k_i	1.02 % K^{-1} $year^{-1}$
k_p	0.85 % K^{-1}

Table 4.2: Summary metrics for the SI experiment from CESM 1.2.2. Note that, when calculating gain values, the sign of phase-related metrics are flipped by convention since the output lags behind the input.

M, Φ, and Φ_t collectively describe the key features of the system at the chosen frequency, which can be used to optimize k_i and k_p values. Lastly, we use a phase margin of 60° when calculating gain values, where the phase margin is the difference between the total phase lag of the system (Φ_t+Φ) plus the controller and -180°. The phase margin represents a buffer zone between the total phase lag of the system plus the controller and the point of system instability. Therefore, it is useful to select a higher phase margin to account for the SI experiment failing to accurately characterize the behaviour of the system at the chosen frequency. For more information on control system design for geoengineering with ESMs and a step by step methodology for optimizing gain values using system identification runs, see Kravitz et al. (2016).

Alongside effectively managing the surface air temperature response, the advantage of using the PI controller as opposed to manually adjusting the solar constant is that the reduction in S_0 becomes an emergent property of the model. Treating the time varying S_0 as an emergent property– analogous to the surface temperature response in +1%CO_2 yr^{-1} or abrupt 4xCO_2 experiments– allows one to quantify *geoengineering feedbacks* as an energy budget perturbation per unit of geoengineering (in our case, a 1% change in S_0). We expand

on this in the following subsection.

4.3.4 Radiative Adjustments & Feedbacks

As in Virgin and Fletcher (2022), we quantify radiative adjustments in fixed SST and sea ice experiments using a linear framework for the TOA energy budget:

$$ERF = IRF + A_{net}, \tag{4.2}$$

$$\text{where } A_{net} = \sum_{i=1}^{N} \frac{\partial R}{\partial x_i} dx_i \tag{4.3}$$

The ERF is decomposed into the IRF and the total radiative adjustment (A_{net}). The total radiative adjustment is the sum of adjustments from fast responses in surface albedo, temperature, water vapour, and clouds (Chung and Soden, 2015; Smith et al., 2018). Radiative kernels ($\frac{\partial R}{\partial x_i}$) are applied to state variable responses (dx_i) to calculate each adjustment (in W m^{-2}). For $4xCO_{2(f)}$ and SOL_f, all state variable responses are calculated as the 30 year mean difference relative to CTL_f. For surface albedo, temperature, and water vapour, we use radiative kernels calculated using CAM3 (Shell et al., 2008), which used the CAM Radiative Transfer model (CAMRT) that is also used in the CAM4 configuration used for our experiments. For clouds, we use cloud radiative kernels designed for use with COSP output from ESMs (Appendix A, Zelinka et al. (2012a,b)). Using the cloud kernel method, we decompose both the shortwave (SW) and longwave (LW) cloud adjustments into contributions from the boundary layer (>680 hPa) and free troposphere ($\leq$ 680 hpa). More detail on using cloud radiative kernels to decompose cloud feedbacks can be found in Zelinka et al. (2016). Finally, the ERF is calculated as the 30 year mean TOA net radiation delta relative to CTL_f.

The conventional linear forcing-feedback framework uses global, annual mean surface warming as the independent variable, which would produce zero feedbacks by construction for GEO and any geoengineering experiment design that targeted global mean surface air temperature. Therefore, we introduce a new methodology for the GEO experiment to quantify the relationship between time varying adjustments as a response to combined transient greenhouse gas and geoengineering forcings.

The theoretical basis centers on the definition of a geoengineering feedback parameter, which is directly analogous to the classic radiative feedback parameter (Hansen et al., 1997):

$$\lambda_g = \frac{dR}{dg}, \tag{4.4}$$

where dR is the unit change in the TOA energy budget (in W m^{-2}) and dg is the unit change in geoengineering. In the case of the GEO experiment, the unit change of geoengineering is a percentage reduction in S_0. The geoengineering feedback can be linearly decomposed similar to surface temperature mediated feedbacks:

$$\frac{dR}{dg} = \sum_{i=1}^{N} \frac{\partial R}{\partial x_i} \frac{\partial x_i}{\partial g}, \tag{4.5}$$

where, as in Equation 4.3, $\frac{\partial R}{\partial x_i}$ represents the radiative sensitivities for a given state variable (x_i), and $\frac{\partial x_i}{\partial g}$ represents the state variable response per unit change of geoengineering. Therefore, geoengineering feedbacks here are quantified in units of W m^{-2} $\%^{-1}$. In practice, we quantify the radiative adjustment associated with each state variable for each year of the GEO experiment relative to 30 year control climatology (years 70-100 of CTL) using radiative kernels. Then, each radiative adjustment time series is linearly regressed against ΔS_0 as calculated by the controller using all 140 years. Note that the sign convention of all geoengineering feedbacks presented in this paper has been flipped to equate the

decrease of S_0 to an *increase* in geoengineering. Since ΔS_0 is used as a proxy for a family of SRM techniques such as SAG, geoengineering feedbacks can physically be thought of as state variable responses initiated by SRM that cause additional changes to planetary albedo that either amplify (positive feedback) or damp (negative feedback) the initial SRM. Thus, the practical impact of geoengineering feedbacks is to change the efficacy of the SRM technique being applied, resulting in either more or less geoengineering being required to meet a particular temperature target than was originally estimated in the absence of such feedbacks.

4.4 Results

4.4.1 Radiative Forcing & Adjustments

First, we present results from the fixed SST experiments from to quantify the radiative forcing and adjustments associated with the CO2 and Solar forcings applied separately and in the absence of surface temperature-mediated feedbacks. The global, annual mean ERF is -8.17 W m^{-2} in SOL_f, which more than compensates for the global mean ERF associated with quadrupling CO_2 (7.53 W m^{-2}). Previous work has explored the difference in efficacy between the two forcings here (Modak et al., 2016; Russotto and Ackerman, 2018), which has been linked to radiative adjustments. Quantifying the ERF and radiative adjustments for $4xCO_{2(f)}$ and SOL_f, as well as exploring the physical drivers of each adjustment, provide a useful point for comparison against the GEO experiment which has both a positive CO_2 and a negative solar forcing (Table 4.1). By deconstructing the ERF in terms of the TOA energy budget for $4xCO_{2(f)}$ and SOL_f, we expect these results to provide insight into the drivers of geoengineering feedbacks in the coupled GEO experiment.

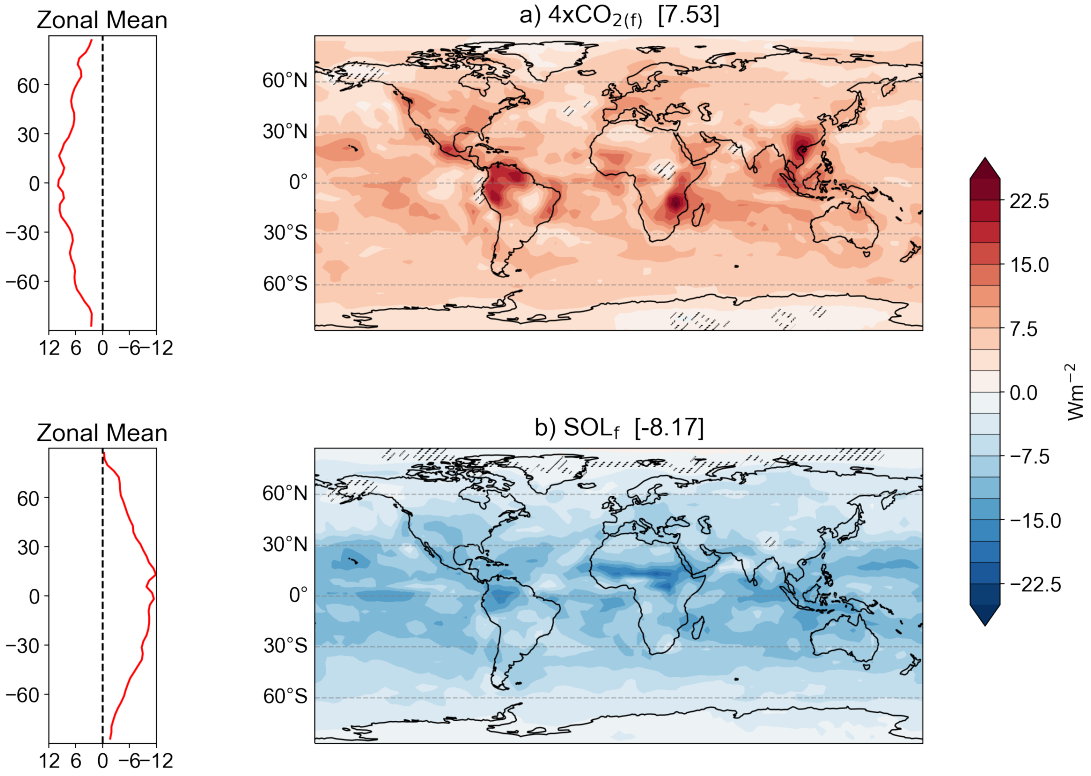

Figure 4.2: Effective Radiative Forcing (ERF) maps for the $4xCO_{2(f)}$ and SOL_f experiments. Calculation follows RFMIP protocol, where each map is the 30 year annual mean response of each experiment relative to CTL_f. Hatching represents gridboxes that are not statistically significant ($p>0.05$), where significance is calculated using a two tailed independent t-test using all 60 years. The global mean ERF values are shown in brackets next to each subplot title.

The prescribed forcing in $4xCO_{2(f)}$ is a spatially homogeneous increase in CO_2 concentration, but the the ERF peaks in the tropics and is weaker towards the poles (Figure 4.2a). This is primarily driven by the instantaneous forcing (IRF) prior to any radiative adjustments, where increased CO_2 produces a more optically opaque atmosphere, effectively shifting the emission layer upward (Zhang and Huang, 2014; Huang et al., 2017). Where the lapse rate is the steepest, the net forcing is larger as the emission temperature there is colder (Huang et al., 2016).

The meridional of SOL_f ERF is primarily driven by heterogeneous spatial distribution of downwelling shortwave radiation produced by reducing the solar constant (Figure 4.2b), where a 4% reduction scales the climatological distribution of insolation. Radiative adjustments from local changes in temperature, water vapour, and clouds contribute to the ERF at the gridbox level. For particularly the Arctic in SOL_f, the net TOA radiation is not statistically different from CTL_f at the 95% confidence level, where the ERF is near zero (Figure 4.2b, see hatching).

The ERF spatial distribution for both experiments in Figure 4.2 is also influenced by experiment design given the land surface is not constrained. We show the surface air temperature response in Figure 4.3. The surface response is spatially consistent for both experiments, where the northern hemisphere warms in $4xCO_{2(f)}$ and cools in SOL_f.

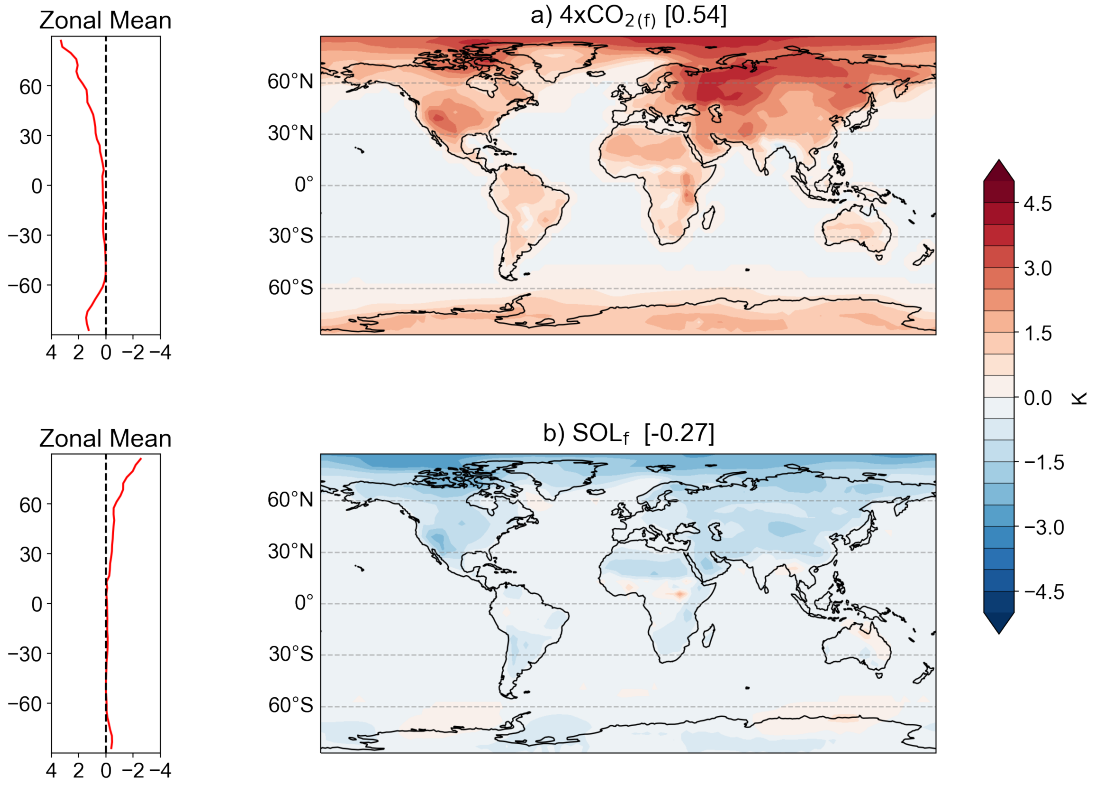

Figure 4.3: As in Figure 4.2, but for surface air temperature response relative to CTL_f.

Furthermore, despite the fixed sea ice fraction, Arctic amplification (AA) is present in both experiments as well consistent with the sign of both forcings. That is, peak cooling in the Arctic in SOL_f and peak warming in the Arctic for $4xCO_{2(f)}$. This result supports previous studies that show increased atmospheric poleward energy transport under CO_2 forcing (Huang et al., 2017) and its influence on meridional surface warming profiles (Rose et al., 2014).

To quantify what is driving the overall ERF, we break down global, annual mean radiative adjustments for $4xCO_{2(f)}$ and SOL_f in Figure 4.4. The net adjustment is positive for both experiments, where the stratosphere temperature, troposphere temperature, and

shortwave cloud adjustments are the largest contributors. Surface albedo, LW cloud, water vapour, and troposphere temperature are of opposite sign and similar magnitude between each experiment, whereas stratospheric temperature and SW cloud adjustments are positive for both experiments. As a result, the net adjustment is 1.07 W m^{-2} for SOL_f and 2.17 W m^{-2} for $4xCO_{2(f)}$, indicating that radiative adjustments amplify the positive CO_2 IRF and damp the negative solar forcing. The standard error for all individual adjustments, as well as the net adjustment, in both experiments is less than 10% of the total, demonstrating the robustness in these responses. These results are qualitatively consistent with our previous work that showed the dampening effect of radiative adjustments on solar dimming efficacy (Virgin and Fletcher, 2022).

Our understanding of all non-cloud radiative adjustments is fairly straightforward. Stratospheric cooling is present in both experiments and results in a positive radiative adjustment (Wetherald and Manabe, 1975; Manabe and Wetherald, 1975). The tropospheric temperature adjustment is tied to the surface response in both experiments. The lapse rate contribution to the tropospheric adjustment is near zero in $4xCO_{2(f)}$, illustrating that the Planck response from northern hemisphere warming over land contributes the most to the total temperature adjustment (Figure 4.3a). In contrast, the positive troposphere temperature adjustment in SOL_f is roughly equal between lapse rate and Planck adjustments. The Planck adjustment is caused by land surface cooling over all land surfaces (Figure 4.3b). In low latitudes, the moist adiabatic adjustment preferentially cools the upper troposphere relative to the surface, which decreases emitting temperature and causes a positive lapse rate adjustment. The land surface response dominates in the global mean for both experiments, which produces a positive temperature adjustment for SOL_f and a negative adjustment for $4xCO_{2(f)}$.

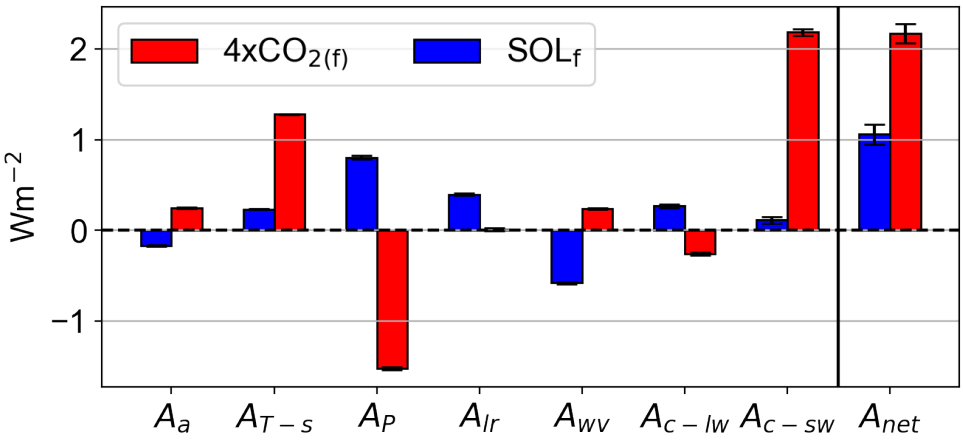

Figure 4.4: Global, annual mean radiative adjustments in W m^{-2} for the $4xCO_{2(f)}$ and SOL_f experiments. Each value is calculated using the 30 year mean climate response relative to a pre-industrial control simulation. Uncertainty is defined as plus/minus 1 standard error of the mean using all 30 years of the response. From left to right, adjustments are listed as surface albedo (A_a), stratospheric temperature (A_{T-s}), Planck (A_P), lapse rate (A_{lr}) , troposphere + stratosphere water vapour (A_{wv}), longwave cloud (A_{c-lw}), shortwave cloud (A_{c-sw}), and net (A_{net}).

The largest and most important difference between SOL_f and $4xCO_{2(f)}$ arises through cloud radiative adjustments, which is explored in further detail in Figure 4.5. Figures 4.5a and b show the global, annual mean cloud fraction response as a function of optical depth and cloud top pressure (CTP). In both experiments, the fraction of optically thin clouds in the upper troposphere and lower stratosphere cloud fraction increases in the lowest optical depth bins. However, these cloud changes contribute little to the net cloud adjustment because the radiative sensitivity for the bottom two optical depth bins is low throughout the atmosphere column (Figure C.1, Zelinka et al. (2012a)). In SOL_f, the weakly positive total LW cloud adjustment is also due to slight increases of optically thick clouds in mid troposphere (560-310 hPa, which are more sensitive to changes in cloud fraction in terms of radiation (Figures 4.5b, C.1).

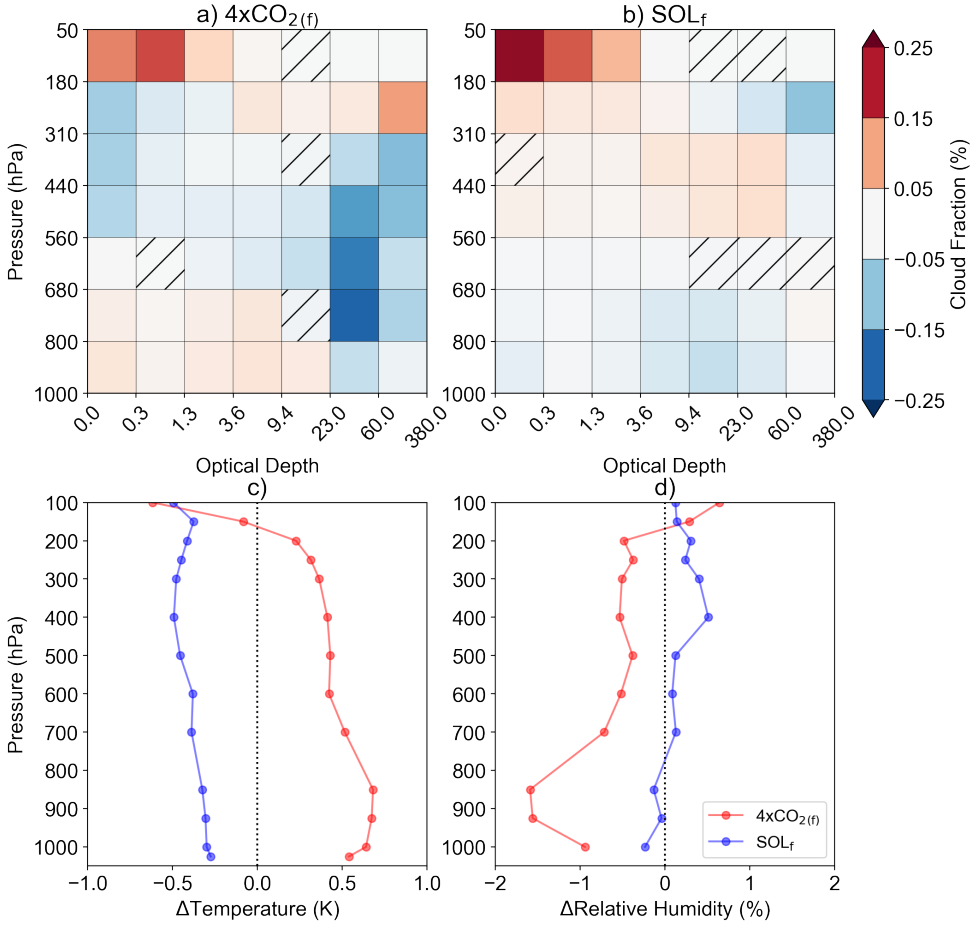

Figure 4.5: a) & b) Global, annual mean ISCCP cloud fraction response (in percent) for the $4xCO_{2(f)}$ and SOL_f experiments, respectively. The ISCCP fraction is plotted on optical depth (x) and cloud top pressure (y) axes. Responses are defined as the 30 year climatology delta relative to the control case. Hatching represents statistically insignificant grid boxes calculated using a student's two tailed independent t-test with all 60 years of available data. c) & d) Global, annual mean air temperature and relative humidity responses for both $4xCO_{2(f)}$ and SOL_f experiments.

The SW cloud adjustment is 2.18 W m^{-2} in $4xCO_{2(f)}$, which is driven by decreases in the optically thickest clouds throughout the troposphere below 310hPa (Figure 4.5a). The SOL_f total SW cloud adjustment is 0.11 W m^{-2}, consistent with previous work showing that cloud radiative adjustments for idealized geoengineering forcings are positive for the

CO_2 component of the forcing (Virgin and Fletcher, 2022; Russotto and Ackerman, 2018). While there are small decreases in clouds for the largest optical depth bins, their radiative contribution to the total adjustment is offset by increases for all other optical depths throughout the mid troposphere.

The physical causes of these changes in cloud fraction and altitude are related to the details of each experiment's configuration. The global mean vertical temperature and relative humidity responses for both experiments are shown in Figure 4.5c and d. For $4xCO_{2(f)}$, the bottom heavy warming profile dominates, which has a destabilizing effect on the troposphere alongside preferentially drying the boundary layer (Salvi et al., 2021). Physically, lower troposphere drying comes from the combination of fixed SSTs with small increases in surface air temperature, which decreases upward latent heat flux from the surface (Kamae and Watanabe, 2013). The result is reductions in optically thick clouds and a positive radiative adjustment in the global mean (Figures 4.4,4.5a). In SOL_f, the troposphere cools throughout the column, which reflects the different radiative forcing structure between CO_2 versus solar forcing. CO_2 forcing makes the atmosphere more optically opaque, while solar forcing primarily changes surface radiative flux and therefore impacts LW radiation throughout the atmosphere (Henry and Merlis, 2020).

4.4.2 Geoengineering Feedbacks

With a physical basis for explaining radiative adjustments as a response to CO_2 and solar forcing in the fixed SST experiments, we now explore the coupled GEO experiment through geoengineering feedbacks and their impact on the PI controller's ability to meet the target global, annual mean surface temperature.

The PI controller performs well in terms of dynamically maintaining the global, annual

mean surface air temperature close to target to counteract the CO_2 forcing in the GEO experiment (Figure 4.6a). Residual year-to-year variability in surface air temperature is an expected feature of the temperature time series given the lag of the controller in adjusting S_0, in the present of internal variability on a wide spectrum of timescales. This result agrees with previous studies showing that control system design is effective at both characterizing the frequency response of ESMs to forcing (Figure 4.1) and simulating geoengineering to meet specified climate objectives (Kravitz et al., 2014, 2016; MacMartin et al., 2014; MacMynowski et al., 2011).

In GEO, The PI controller reduced S_0 by 36.86 W m^{-2} (0.97%) by the end of the simulation (Figure 4.6b). We also show global, annual mean planetary albedo on the secondary x-axis in Figure 4.6b, which decreased by 0.54% by the end of GEO.

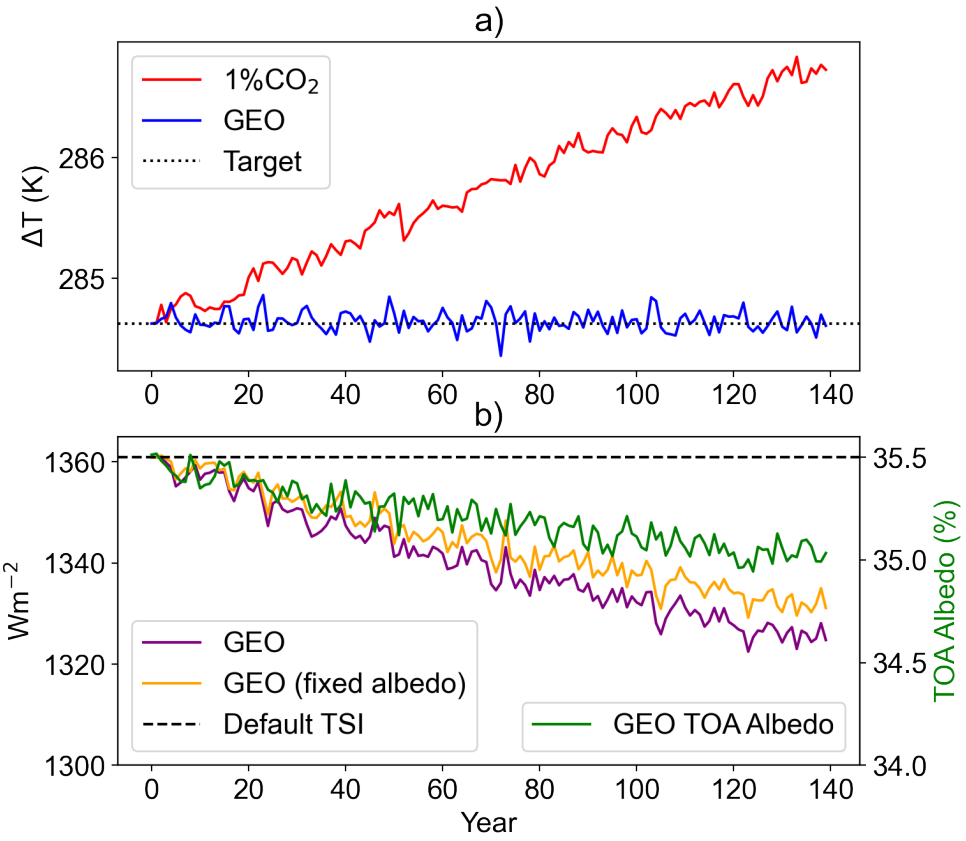

Figure 4.6: a) Global, annual mean surface air temperature for the 1%CO_2 (red) and GEO experiments (blue). b) S_0 for the GEO experiment calculated by the controller (purple line). The orange line is the S_0 assuming planetary albedo remains fixed to the year 0 value (0.355) for the full length of the simulation. Planetary TOA albedo is shown on the secondary y-axis (green line).

This result implies that the efficacy of a unit change in S_0 gradually diminished over time as a larger proportion of downwelling SW radiation was reaching the surface. This is illustrated by the orange line in Figure 4.6b, which is the implied S_0 for GEO assuming planetary albedo remained fixed at its year 0 value (0.355) for all 140 years. In terms of insolation, this is expressed as an extra 6.89 W m^{-2} reduction by the end of the simulation. The reduction in albedo contrasted against the effectiveness of the PI controller illustrates

the advantage of using control system design for geoengineering given its ability to account for changes in state variables in a non-linear fashion "on the fly", which would have been more difficult to account for via manual tuning. Furthermore, it also implies that radiative adjustments make a non-negligible contribution to the TOA energy budget in GEO and therefore the surface temperature response. We show the spatial distribution of the surface air temperature response in Figure 4.7.

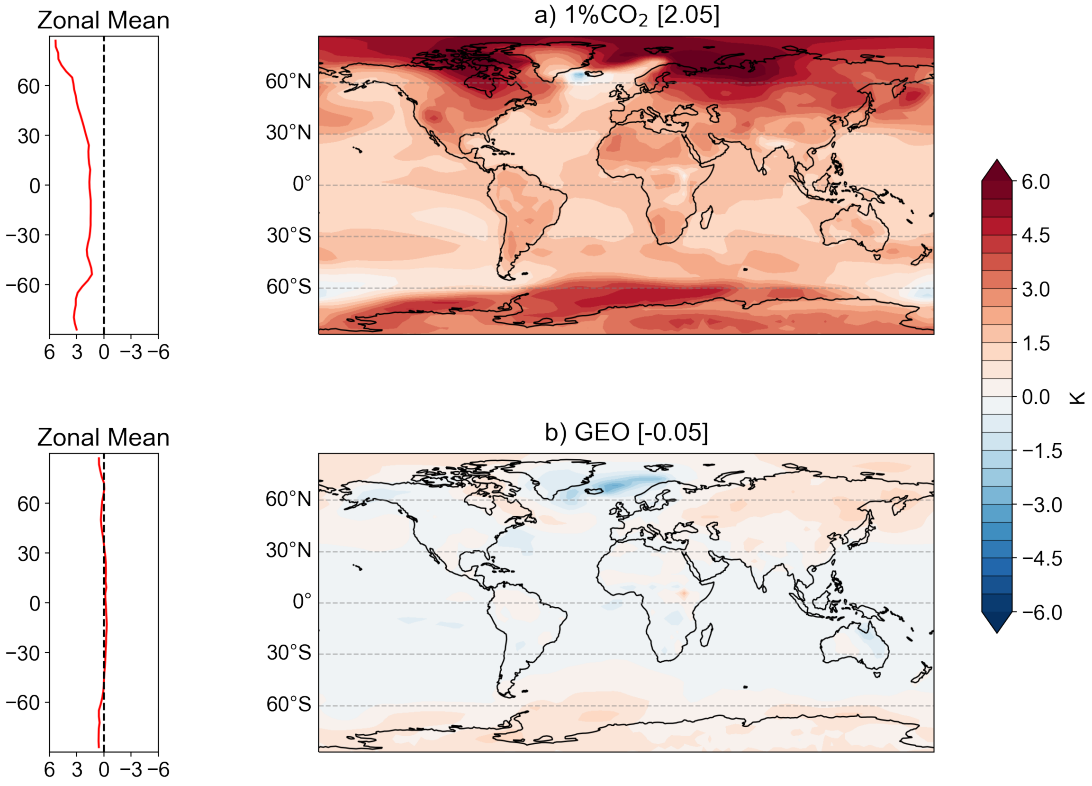

Figure 4.7: Annual mean surface air temperature response for years 120-140 relative to the CTL experiment climatology for a) the 1%CO_2 experiment and b) the GEO experiment. The global mean is included as the values in square brackets next to each title.

Figure 4.7a shows the familiar pattern of warming associated with greenhouse gas forcing experiments that includes greater warming over land than ocean and amplified warming

at higher latitudes, particularly in regions of high preindustrial sea ice concentration. Despite the PI controller effectively suppressing global mean surface warming induced by CO_2 forcing, there are clear examples where the regional warming from CO_2 is under-corrected, and others where it is over-corrected. Widespread low latitude cooling is offset by high latitude warming, which is consistent with other models running the G1 GeoMIP experiment (Kravitz et al., 2013). While the North Atlantic cools in GEO here, the magnitude and sign of this response is uncertain across models for G1. Contrasting the GEO surface temperature response against 1%CO_2 surface warming by the end of both experiments exemplifies the impact of solar dimming. That is, the combined effect of CO_2 forcing and surface temperature mediated feedbacks contributing to the spatial structure of surface warming in 1%CO_2– particularly with respect to polar amplification (Figure 4.7a). In order to better understand the evolution of geoengineering efficiency in the GEO experiment, we decompose the geoengineering feedback parameter in Figure 4.8.

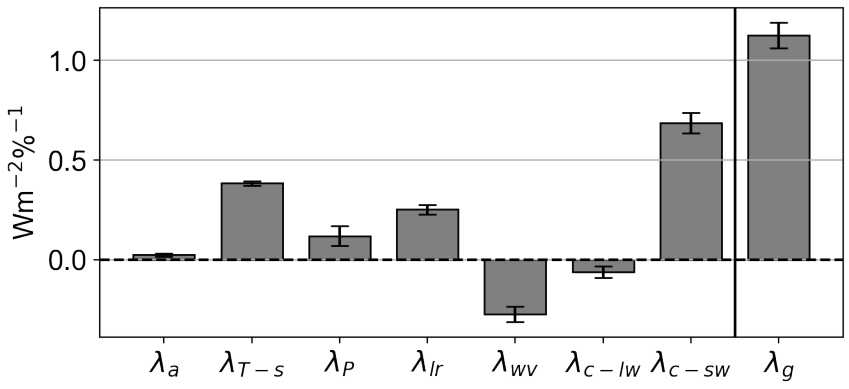

Figure 4.8: Global, annual mean geoengineering feedbacks for the GEO experiment. From right to left, feedbacks are listed as surface albedo (λ_a), stratosphere temperature (λ_{T-s}), Planck (λ_P), lapse rate (λ_{lr}), troposphere water vapour (λ_{wv}), longwave cloud (λ_{c-lw}), shortwave cloud (λ_{c-sw}), and net (λ_g). The error bars denote the regression slope 95% confidence interval for each feedback. Note that the sign of these feedbacks have been flipped to illustrate the energy budget response against a *reduction* in the solar constant as a proxy for geoengineering.

The net geoengineering feedback (λ_g) is made up of contributions from surface albedo, temperature, water vapour, and cloud feedbacks. Temperature feedbacks are separated into a stratosphere and troposphere component, and the latter is comprised of Planck and lapse rate feedbacks. Recall that the sign of the denominator in the regression has been flipped to represent decreases in S_0 as an increase in geoengineering (Section 24.3.4). The net geoengineering feedback (λ_g) is 1.13 W $m^{-2}\%^{-1}$, which represents the net energy tendency at the TOA per percent reduction in S_0. The two largest positive contributors to λ_g are the SW cloud and stratosphere temperature feedbacks. The surface albedo and LW cloud are feedbacks are near zero. The near zero surface albedo feedback is consistent with other idealized geoengineering simulations that show minimal changes in sea ice extent despite residual polar warming (Kravitz et al., 2013). Finally, the lapse rate (+0.25 W $m^{-2}\%^{-1}$) and water vapour (-0.27 W $m^{-2}\%^{-1}$) feedbacks sum to near zero when combined.

Physically, the stratosphere temperature feedback is consistent with the fixed SST experiments in Section 3.1 where the stratosphere cooled in both SOL_f and abrupt-4x$CO_{2(f)}$. As the controller reduces S_0, the stratosphere continues to cool due to the combined positive CO_2 and negative solar forcing. In terms of TOA energy balance, this adjustment drives increased outgoing LW flux to space that, when combined with a decreasing S0, produces a positive feedback loop. The weakly positive Plank feedback in GEO results from cooling in the tropics and subtropics (Figure 4.7b), and the positive lapse rate feedback indicates preferentially enhanced cooling in the upper troposphere relative to the surface in the tropics. As a feedback loop, the continued reduction in S_0 further enhances upper troposphere preferential cooling relative to the boundary layer and surface. The water vapour feedback is intrinsically linked to the vertical structure of the temperature response because the water vapour kernel assumes a constant relative humidity (Soden et al., 2008). As the troposphere cools, specific humidity decreases and the greenhouse effect from water

vapour is diminished.

The geoengineering SW cloud feedback is distinct given its first order impact on planetary albedo and that it is the largest contributor to the net positive geoengineering feedback (0.67 W $m^{-2}\%^{-1}$). As shown in Figure 4.4, although both $4xCO_{2(f)}$ and SOL_f have a positive SW cloud adjustment, it is an order of magnitude stronger in response to CO_2 forcing than negative solar forcing. This result brings a limitation of this approach into focus, which is the implied physical linkage by defining geoengineering feedbacks per percent reduction in S_0. In GEO, the $1\%CO_2$ forcing and evolving SSTs both are likely contributing to the changes in cloud fraction over time. While we do not attempt to attribute changes in cloud fraction from CO_2 forcing, solar forcing, and and surface response, we focus on the SW cloud feedback spatial distribution and physical drivers in the next section to better understand the relationship between tuning S_0 against a positive CO_2 forcing and changes to clouds.

4.4.3 Cloud Response

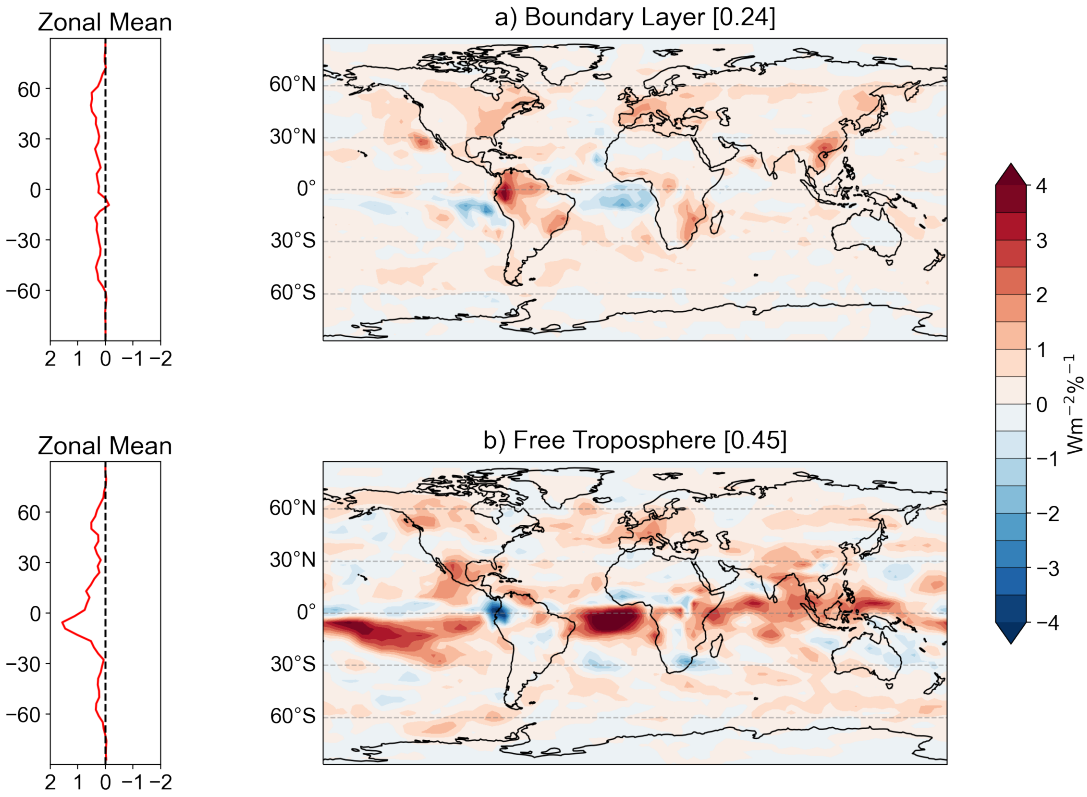

Figure 4.9: Annual mean geoengineering shortwave cloud feedbacks separated into boundary layer (>680 hPa, a and b) and free troposphere (≥ 680 hPa, c and d) contributions for the GEO experiment. Feedbacks were calculated for each grid box by regressing the shortwave cloud radiative adjustment times series (relative to years 70-100 of CTL) against the ΔS_0 calculated by the PI controller. Global mean values are shown next to each subplot title. As in Figure 4.8, the sign has been flipped as a proxy for geoengineering.

Figure 4.9 shows the annual mean SW cloud geoengineering feedback decomposed into boundary layer and free troposphere components. About two-thirds of the global mean total cloud feedback comes from changes to clouds in the free troposphere (≤ 680 hPa), and one-third from changes to clouds in the boundary layer (> 680 hPa). The boundary

layer feedback is generally positive from mid to lower latitudes (Figure 4.9a). Regional maxima over the Amazon and over mid latitude forested regions may be attributable to the physiological effect on plants from CO_2 forcing, where reduced evapotranspiration causes reductions in boundary layer cloud fraction (Doutriaux-Boucher et al., 2009). There are regions of negative feedback in the tropics off the African coast and the Eastern Pacific cold tongue, which indicates an increase in low cloud fraction over these regions. The free troposphere feedback also increases toward lower latitudes, with a band of strong positive feedback across the equatorial Eastern Pacific, Atlantic, and Indian oceans. The local maxima are found in regions with reductions in cloud fraction, which could potentially obfuscate the boundary layer feedback result due to the ISCCP's top down perspective (Zelinka et al., 2018). To better understand the temporal evolution of the strong positive SW cloud geoengineering feedback in the tropics over the oceans, we now analyze the evolution of the three cloud controlling factors over the course of the GEO experiment.

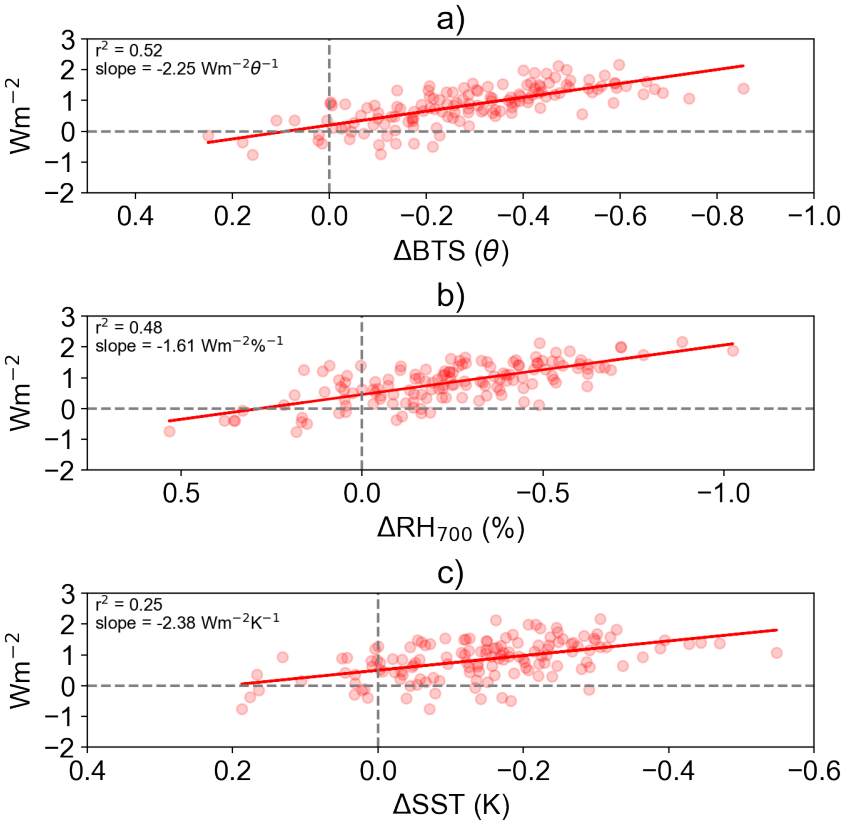

Figure 4.10: The tropical mean (30N-30S) free troposphere SW cloud radiative adjustment, calculated using cloud kernels, in GEO plotted against a) tropical mean bulk tropospheric stability (see Appendix B), b) tropical mean 700 hPa relative humidity, and c) tropical mean SSTs. Each marker is a year in all 140 years of GEO relative to the CTL experiment climatology. Note that the x axis has been flipped for all three plots to illustrate the decreasing trend in each variable over time in GEO.

Focusing on the tropics, we plot the evolution of the free troposphere SW cloud radiative adjustment in GEO against bulk tropospheric stability (BTS), 700 hPa relative humidity, and SSTs in Figure 4.10. BTS is defined as $\theta_{200-850} - \theta_{850-1000}$, where $\theta_{200-850}$ is the mean potential temperature from 200 to 850 hPa and $\theta_{850-1000}$ is mean potential temperature from 850-1000 hPa (Salvi et al., 2021). All three factors exhibit a decreasing trend in

GEO over time; the tropical surface cools, the boundary layer dries, and free troposphere destabilizes. The negative BTS trend also informs our understanding of the positive lapse rate geoengineering feedback. Near the surface, the rate of cooling is small relative to the upper troposphere (Figure 4.7b). All three factors have negative relationships with SW free troposphere cloud radiative flux, which is physically consistent with the trend of decreasing free troposphere cloud fraction.

Despite the ocean being allowed to respond in GEO, these results are physically consistent with the combined global mean vertical profiles of temperature and relative humidity in $4xCO_{2(f)}$ and SOL_f (Figure 4.5c and d). The reduced S_0 over time in GEO enhances the vertically isothermal cooling, which is partially offset by the bottom heavy warming profile of increasing CO_2. In terms of explaining the SW cloud geoengineering feedback, the reduction in BTS decreases optically thick cloud fraction, which produces a positive radiative feedback. The effect is most pronounced in the tropics because of the meridional forcing structure from reducing S_0, where there is proportionally less downwelling SW radiation at the TOA in the topics relative to the poles (Figure 4.2b). The evolution of relative humidity is also conducive to reductions in cloud fraction as the boundary layer dries from CO_2 forcing (Figure 4.10b, Kamae and Watanabe (2012)).

4.5 Discussion & Conclusions

In this study, we have explored the role of radiative feedback loops in an idealized geoengineering simulation where the solar constant was dynamically adjusted to offset the global mean warming from a 1 percent per year increase in CO_2. We define a new type of radiative feedback diagnostic specifically for geoengineering experiments that quantifies the radiative perturbation per unit of geoengineering– in this case a percentage reduction in S_0.

We find that geoengineering feedbacks are physically consistent with radiative adjustments as a response to positive CO_2 and negative solar forcing that are of the same sign (Figure 4.4). Specifically, the strongest positive feedbacks are associated with reductions in mid-troposphere optically thick clouds over tropical oceans and stratospheric cooling (Figure 4.8). Stratospheric cooling has positive LW contribution and reductions in optically thick clouds have a negative SW contribution to TOA energy balance. The result is a reduction in the efficacy of S_0 in terms of its ability to suppress warming, which is illustrated by the PI controller dynamically accounting for the decreasing trend in planetary albedo in GEO by strengthening the reduction in S_0 over time (Figure 4.6).

Despite the advantage of this new approach in quantifying why geoengineering efficacy changes over time, geoengineering feedbacks suffer from several limitations that make them more difficult to interpret than traditional surface temperature mediated feedbacks. Perhaps most important is defining the feedback as per unit of geoengineering in the presence of both a time varying positive CO_2 forcing and surface response. As they are defined in Equation 4.3, radiative adjustments per unit of geoengineering ($\frac{\partial x_i}{\partial g}$) include state variable responses from CO_2 forcing and the secondary impact of local changes in surface temperature. While the spatial distribution of surface temperature can be controlled for (e.g., preserving the equator to pole temperature gradient alongside the global mean surface temperature), local changes in surface temperature in regions of deep convection can propagate throughout the atmospheric column and impact cloud fraction. Furthermore, the definition of a geoengineering feedback presupposes that any representation of geoengineering– either reductions in S_0 or gridbox injections of SO_2– is introduced to offset a positive greenhouse gas forcing. From a modelling standpoint, using the PI controller to interpret ΔS_0 as an emergent property of the model also requires a temperature response, where the surface warming is also influenced by the radiative adjustments from increasing CO_2 each year.

The strength of surface temperature mediated feedbacks differ when forced with solar versus CO_2 forcing (Kaur et al., 2023). Geoengineering feedbacks contrast from surface temperature feedbacks even further given they are a direct response to forcing type. The magnitude of the SW cloud geoengineering feedback is partially the result of negative solar forcing ERF peaking in the tropics (Figure 4.2b), which is unique to this type of geoengineering proxy. This is particularly important for any kind of stratospheric temperature feedback given that simulations of geoengineering with gridbox SO_2 injections heat the tropical lower stratosphere (Tilmes et al., 2009; Richter et al., 2018). SW cloud geoengineering feedbacks should be of particular focus given the inter-model spread of cloud adjustments from solar and CO_2 forcing (Modak et al., 2016; Schmidt et al., 2012; Smith et al., 2018). Quantifying the inter-model spread of cloud geoengineering feedbacks with a similar methodology as shown here would have significant implications for any realizable geoengineering scenario (e.g., aerosol injections in the G6sulfur scenario), as previous studies assessing cloud fraction response to volcanic eruptions or SAG in fixed SST experiments have shown reductions in tropical anvil clouds from increased upper troposphere stratification (Saint-Lu et al., 2022; Boucher et al., 2017). Notably, these studies contrast against the results that show mid troposphere reductions in cloud fraction here, which supports the notion that, in more respects than just changes in cloud fraction, solar constant tuning is not a suitable analogue for SAG for the purposes of impact assessment (Visioni et al., 2021a). Nevertheless, ESM surface temperature mediated cloud feedbacks that are biased high against expert synthesis are the main source of spread in Equilibrium Climate Sensitivity (ECS) in CMIP6 (Zelinka et al., 2022). Therefore, understanding how such biases would impact geoengineering efficacy over time is integral to constraining the expected climate response if a SAG scheme were to be implemented in nature. Future studies could use similar methods here to assess the thermodynamic response of the troposphere from

SAG deployed using control system design.

Chapter 5

Conclusions

5.1 Summary

As of 2023, the best estimate of the Earth's remaining budget to limit global, annual mean surface temperature rise to less than 1.5°C is 250 Gigatonnes of CO_2 equivalent (50% likelihood), which is a decrease of 37.5% relative to the IPCC Working Group I Sixth Assessment Report on Climate Change published in 2019 (Forster et al., 2023). Geoengineering research continues to gain traction as more consideration is given to potential emergency climate intervention measures to help achieve the goals set forth in the Paris Agreement. Should any form of geoengineering be implemented, it is essential to understand how the efficacy of geoengineering radiative forcing will evolve over time. This thesis strove to bridge the methodological gap between surface temperature mediated radiative feedbacks and potential geoengineering feedbacks and how they may impact forcing efficacy. Here, we revisit the research goals from Section 1.3 in the context of the three manuscripts comprising Chapters 2, 3, and 4.

Research Goal 1

Use conventional methods and climate model experiment design to understand how radiative forcing and individual radiative feedbacks contribute to differences in climate sensitivity and surface warming between ESMs.

The manuscript comprising Chapter 2 explored how changes in radiative feedback and forcing impact the increase in ECS from CanESM2 to CanESM5.0.3. ECS rose by 54% in CanESM5 to 5.65 K, which is the largest ECS in the CMIP6 ensemble (Zelinka et al., 2020) and sits outside the 5-95% confidence interval for the observation-based constrained ECS range of 2.3-4.7 K (Sherwood et al., 2020). We used a range of experiment designs from the CMIP deck to quantify the role of forcing and feedback individually. Using fixed-SST experiments from RFMIP to quantify the ERF from an abrupt quadrupling of CO_2, we found a difference of only 0.08 W m^{-2} in the ERF between the two model versions (Table 2.1). Using coupled, abrupt-4xCO_2 experiments, we found that the net radiative feedback parameter was more positive for CanESM5.0.3, which was the result of more positive surface Albedo, LW cloud, and SW cloud radiative feedbacks, with the SW cloud feedback responsible for over half of the ECS increase (Figure 2.1). When decomposed by altitude, optical depth, and analyzed spatially, we found that the SW cloud feedback increase was primarily driven by reductions in PBL cloud fraction amount over Eastern equatorial and sub-tropical ocean basins (Figure 2.3).

Research Goal 2

Understand the physical drivers of surface radiative feedbacks and how they impact planetary albedo and atmosphere infrared optical opacity, and therefore energy balance.

In Chapter 2, we further explored how regional changes in surface warming and EIS drive reductions in PBL cloud fraction in CanESM5.0.3, which resulted in stronger SW cloud feedbacks and therefore climate sensitivity. We found that CanESM5.0.3 had relatively cooler pre-industrial control state local SSTs and larger EIS in Eastern tropical and sub-tropical ocean basins than CanESM2, where both CCFs were conducive to increased cloud fraction (Figure 2.4b & 2.5a). In experiments where CO_2 was quadrupled, the larger decrease in PBL cloud fraction over time resulted in enhanced surface warming in the Eastern Pacific (Figure 2.5c), which is representative of the pattern effect frequently seen in warming experiments from ESMs (Stevens et al., 2016). We confirmed this result using the amip-PiForcing experiment, which forces CanESM5.0.3 using the historical pattern of warming, resulting in a more negative SW PBL cloud feedback due to constrained surface warming in regions with large stratocumulous cloud decks (Figure 2.6).

In addition to offering an exhaustive analysis of the evolution of ECS between two version of CanESM, Chapter 2 explores the impact of local changes in SSTs and their impact on radiative feedbacks. Previous work has shown spatial evolution of surface warming in both historical and idealized forcing experiments (e.g., 4xCO_2) is important for understanding the evolution of globally averaged lapse rate and cloud feedbacks (Andrews and Webb, 2018). This pattern effect of warming extends directly into Chapter 4 as well given the spatially heterogenous surface response in the GEO experiment.

Research Goal 3

Leverage the use of fixed-SST experiment design to quantify and differentiate radiative adjustments from surface radiative feedbacks and how they influence TOA energy balance, and therefore forcing efficacy. Extend the analysis of adjustments to assess solar forcing

efficacy as a proxy for geoengineering.

Chapter 3 shifts focus from feedback to forcing. Here, we use CESM and fixed-SST experiment design to quantify radiative adjustments and their impact on forcing efficacy for both a positive CO_2 and negative solar forcing. We find that radiative adjustments as a response to 4xCO_2 are a net positive contribution to the IRF such that they increase the ERF (Figure 3.2a)— a result consistent across many ESMs (Smith et al., 2018). We also find that the net adjustment to negative solar forcing is positive, which has a dampening impact on the efficacy of tuning the solar constant to offset the ERF from increasing CO_2. The largest contribution to the net adjustment in the G1 experiment came from a positive SW cloud adjustment, which was driven by a reduction in optically thick cloud fraction throughout the PBL and the mid-troposphere (Figure 3.3). This manuscript also briefly explores the potential for non-linear radiative adjustments as a result of both CO_2 and solar forcing being applied concurrently. We found that the troposphere temperature, water vapour, and SW PBL cloud adjustment are more positive when both forcings are applied together (Figure 3.3b), implying that a portion of the total radiative adjustment in the G1 experiment comes from the troposphere responding non-linearly to both forcings.

Chapter 3 stops short of assessing the physical drivers behind changes in cloud fraction in the G1 fixed-SST experiment. However, this is explored further in the following chapter.

Research Goal 4

Develop a method for quantifying geoengineering radiative feedbacks in transient dual-forcing experiments, where CO_2 is incrementally increased and the solar constant is decreased. Use this methodology to understand how geoengineering efficiency may evolve over time as a result of changes in planetary albedo.

With the groundwork for understanding how both external perturbations (i.e. forcing) and surface response (i.e. feedback) impact the global energy budget from Chapter 3, Chapter 4 iterates on these experiments to quantify radiative adjustments in a coupled solar dimming experiment. Using a PI controller to effectively manage the amount of downwelling SW radiation in response to increasing CO_2, we were able to maintain near zero global, annual mean warming over the course of the 140 year GEO experiment (Figure 4.6a). We found that planetary albedo was reduced by 0.54% by the end of the GEO experiment (Figure 4.6b), implying that the efficacy of solar dimming was being reduced over time. To further explore the reduction in efficacy, we define geoengineering feedbacks by regressing radiative adjustments in the GEO experiment against the reduction in S_0 and find that the largest positive feedbacks are stratosphere temperature and SW cloud (Figure 4.8). This result is consistent with the sign radiative adjustments in fixed-SST experiments in both Chapter 3 (SOLAR, Figure 3.2) and Chapter 4 (SOL_f, Figure 4.4). Finally, we conduct a deeper analysis on the SW cloud geoengineering feedback and found that it was the result of reductions in optically thick cloud fraction in the mid to lower troposphere over tropical ocean basins (Figure 4.9) The SSTs cooled, the lower troposphere dried, and bulk tropospheric stability decreased— all contributing to the positive feedback (Figure 4.10).

5.2 Limitations

Various experimental and methodological limitations for each manuscript were discussed within their respective chapters. Here, we focus on some limitations persisting across all three manuscripts. We also address a more subjective approach to what defines a geoengineering feedback, which was only briefly addressed at the end of Chapter 4.

Linearity Assumption for the Global Energy Budget

All three manuscripts use a linear framework for the TOA energy budget (Equations 2.1, 3.2, 4.2, 4.3). This assumption can be categorized in two ways,

1. The climate feedback parameter or geoengineering feedback parameter (λ in Equation 2.1 or λ_g in Equation 4.4, respectively) is constant in time.

2. All feedbacks or adjustments are independent and sum to the total climate feedback parameter or total radiative adjustment.

The linearity of the climate feedback parameter with respect to time depends on how it is defined (Knutti et al., 2017). The linear framework used in Chapter 2 is useful for assessing feedback from state variables that were considered, but does not account for feedbacks from the evolution in permafrost, vegetation, ice sheets or atmosphere chemical composition (Knutti and Rugenstein, 2015). Furthermore, linearity is also model-dependent, where many ESMs exhibit a relaxation of the net climate feedback over time (less negative) in idealized warming experiments (Andrews et al., 2012). This inter-model spread has been linked to model physics, but also the timescale and spatial pattern of surface warming (Andrews and Webb, 2018; Dong et al., 2020).

The linearity of the climate feedback parameter (or net radiative adjustment in the context of forcing only) can also be studied with respect to independence. In idealized warming experiments where feedbacks are studied on global scales, second order effects are typically neglected as their contribution is small (Boer and Yu, 2003; Klocke et al., 2013). However, non-linear interactions between some feedbacks, primarily interactions between non-cloud and cloud feedbacks, may be too large to neglect at local and/or shorter timescales (Zhu et al., 2019).

Radiative Kernels

There is more than one way to calculate radiative feedbacks (Wetherald and Manabe, 1988; Soden and Held, 2006; Zhu et al., 2019). Radiative kernels are used in all three manuscripts to calculate either adjustments or feedbacks. None of the kernels used in this thesis were derived from either CanESM2, CanESM5, or CESM1.2 with CAM4. In practice, the spread in radiative sensitivity across kernels is the result of differences in base state, vertical resolution, and the radiative transfer model used in their computation (Soden et al., 2008; Smith et al., 2018). Of these three factors, base state is the largest source of uncertainty, where warmer base states used in a kernel's computation produce larger temperature radiative sensitivities (Jonko et al., 2012, 2013). This result is somewhat intuitive given OLR scales to the fourth power of temperature. Kernel vertical resolution impacts stratosphere temperature radiative sensitivity. In all three manuscripts here, model output was interpolated down to the 17 standard CMIP5 pressure levels, with only 4 levels between 10 and 250 hPa (Taylor et al., 2012). Smith et al. (2020b) showed that, for kernels with higher resolution in the stratosphere, the temperature adjustment was more positive as less information was lost during the interpolation. This could be a potential explanation for why the clear-sky linearity test with CanESM failed using kernels from the ECHAM6 atmosphere model (Figure A.1), where the temperature kernel was interpolated from 47 down to 17 pressure levels (Block and Mauritsen, 2013).

For the work presented in the latter two manuscript chapters with experiments from CESM, differences in base state between the kernel and all experiments potentially overestimated the strength of temperature feedbacks or adjustments as all experiments started from a pre-industrial control state, whereas the kernels from CAM3 were derived from a base state closer to present day (Shell et al., 2008).

ISCCP Simulator Output

The cloud fraction variable from ISCCP simulator output is used in all three manuscript chapters in this thesis. As discussed in Chapter 2, ISCCP simulator output suffers from potential biases due to its top-down perspective, where high altitude clouds can mask the distribution of cloud fraction underneath (Zelinka et al., 2018; Scott et al., 2020). Therefore, when partitioning cloud feedbacks into discrete sections of the atmosphere column, some low cloud feedbacks can be aliased into the high cloud component solely due to changes in overlying clouds. In Chapter 2, we account for this via weighting low cloud fraction by upper level cloud-free grid-boxes (i.e. grid-boxes with cloud fraction in the lowest bins but with no cloud overhead receive of weight of 1). The same process was not carried out in Chapter's 3 and 4. Therefore, some of the low cloud radiative adjustments may be aliased into the non-low cloud component. This represents a discrepancy across the three manuscripts, but does not materially change the result of the total SW cloud adjustment or geoengineering feedback of any experiment conducted with CESM in the latter two manuscripts.

Geoengineering Feedback Terms & Definitions

It may seem straightforward to consider the CO_2 increase in GEO as an external forcing, while including the S_0 decrease as part of the geoengineering feedback given it is treated as an emergent property of the PI controller. This contrasts with how each of these components were defined in Chapter 3, where tuning S_0 was a manual process for the $G1_b$ and $SOLAR_b$ experiments. For the GEO experiment, the PI controller gain values are optimized using the SI experiment that quantifies the magnitude and timescale of the surface response to changes in S_0 (Figure 4.1). This step in the methods is what allows the

time series produced by the controller to be defined as an emergent property of the model. If the same experiment design and SI experiment were carried out under a multi-model ensemble, the range of gain values would reflect model uncertainty and would manifest as inter-model spread of the decreasing S_0 trend. However, it is also worth noting that the SI experiment and controller gain optimization does not require accurate and precise characterization of the system frequency response, as Kravitz et al. (2016) showed using two separate ESMs.

In terms of individual feedbacks, the SW cloud geoengineering feedback is the strongest in the GEO experiment (Figure 4.8). However, the fixed-SST experiments showed that the SW cloud adjustment from a 4x increase in CO_2 is significantly stronger than the adjustment from 4% decrease in S_0 (Figure 4.4). Therefore, in GEO where CO_2 concentration is increasing at 1% per year, the majority of the geoengineering feedback may be driven by CO_2 instead. Given that CO_2 is prescribed, this does not physically constitute a feedback. In Chapter 3, we also showed that some adjustment may be driven by non-linear responses to combined forcings, which may also be important for driving the positive net geoengineering feedback in the GEO experiment. This would be a subject for future work.

5.3 Future Research

As a direct followup to Chapter 4, future work could partition the three components driving the troposphere response in the GEO experiment— CO_2, changes in the S_0 , and local changes in surface temperature. As discussed in the previous section, the line begins to blur on what is defined as a forcing versus a feedback in coupled, transient geoengineering simulations. Therefore, it may be more useful to define all three components as *drivers* of the troposphere response in further discussions and/or work. Three experiments with each

driver applied separately would give insight into whether or not the cloud response in GEO is the linear sum of the three drivers. Practically, this would involve running three 140 year, atmosphere only experiments using the same configuration of CESM outlined in Chapter 4, Section 4.3.1: One with a 1% per year increase in CO_2, one with the S_0 time series extracted from the PI controller, and one with the SST and sea ice data extracted from GEO (analogous to the amip-piForcing experiment design from the CFMIP6 experiment deck and analyzed in Chapter 2).

For all experiments in Chapter's 3 and 4, we used CESM1.2.2 with CAM4. Given the focus on cloud radiative adjustments, surface temperature radiative feedbacks, and geoengineering feedbacks throughout this thesis, future work should consider bringing the methods used in Chapter 4 to new model versions with improved cloud microphysical parameterizations for aerosol-cloud interactions, as well as newer turbulence schemes such as the Cloud Layers Unified By Binormals (CLUBB) scheme in CAM6 (Danabasoglu et al., 2020). Models with interactive chemistry (e.g. WACCM6) are integral for realistic SAG experiment designs, but may also be important for solar dimming experiments as well. For example, stratospheric cooling in both the SOLAR experiment from Chapter 3 and the SOL_f experiment in Chapter 4 is driven by a reduction in SW radiation interacting with ozone, which heats the stratosphere (Forster and Shine, 1997).

Specific focus should be placed on models with large sensitivity to CO_2 and solar forcing as opposed to radiative feedback to assess inter-model spread in efficacy. For example, Russotto and Ackerman (2018) used the G1 ensemble from GeoMIP to assess inter-model spread in radiative adjustments and inferred that the majority of models had positive adjustments from solar forcing but with non-negligible spread. Furthermore, Smith et al. (2018) found that the cloud adjustment to a 5x increase in sulphate emissions had the largest uncertainty range relative to non-cloud adjustments across the models considered

in their ensemble.

More generally, the road forward for future work should take advantage of the methods used to quantify geoengineering feedbacks with SAG experiment designs. It could be argued that the PI controller approach to geoengineering experiment design limits the applicability of such methods to other models and existing datasets (Kravitz et al., 2017). For example, models contributing to GeoMIP6 took different approaches to either use aerosol emissions when possible or to scale AOD if they lack prognostic aerosol treatment (Visioni et al., 2021b). Even for the G6Solar experiment, some models decreased downwelling SW radiation once per decade as opposed to annually. This makes applying the methods used in Chapter 4 to quantify geoengineering feedbacks on existing datasets challenging given that S_0 is defined here as an emergent model property, whereas it could be considered a parameter to be manually, iteratively tuned as in the $G1_b$ experiment in Chapter 3. For available geoengineering experiment output, such as Geoengineering Large Ensemble (GLENS), that make use of the control system design with SAG, extrapolating the approach used here may be challenging given the increase in experiment design complexity with multiple temperature targets (Tilmes et al., 2018). Nevertheless, future research should prioritize increasing our understanding of geoengineering forcing efficacy from an energy budget point of view. Even if it is not through the definition of geoengineering feedbacks as defined here, other techniques used in this thesis such as the cloud radiative kernel technique, can be applied to GeoMIP model output where ISCCP simulator output is available to assess cloud radiative adjustments across the different modelling approaches taken in both the G6Solar and G6Sulfur scenarios.

Chapter 6

Copyright Statement

The material from Chapter 2 is contained within Virgin et al. (2021):

Virgin, J. G., C. G. Fletcher, J. N. Cole, K. von Salzen, and T. Mitovski, 2021: Cloud feedbacks from CanESM2 to CanESM5.0 and Their Influence on Climate Sensitivity. *Geoscientific Model Development*, **14 (9)**, 5355–5372

 The material from Chapter 3 is contained within Virgin and Fletcher (2022):

Virgin, J., and C. Fletcher, 2022: On the Linearity of External Forcing Response in Solar Geoengineering Experiments. *Geophysical Research Letters*, **49 (15)**, e2022GL100200

on July 12th, 2023 (License number: 5586450771598). The material from Chapter 4 is contained within a manuscript currently in review:

Virgin, J., and C. Fletcher, 2023: Declining Geoengineering Efficacy Caused by Cloud Feedbacks in Transient Solar Dimming Experiments. *Manuscript currently in review at Journal of Climate.*

Note that the versions included in this paper differ slightly to satisfy minor revisions as recommended by the thesis examination committee. However, there were no changes to any of the results.

References

Alterskjær, K., J. Kristjánsson, and Ø. Seland, 2012: Sensitivity to deliberate sea salt seeding of marine clouds–observations and model simulations. *Atmospheric Chemistry and Physics*, **12 (5)**, 2795–2807.

Andrews, T., J. M. Gregory, and M. J. Webb, 2015: The dependence of radiative forcing and feedback on evolving patterns of surface temperature change in climate models. *Journal of Climate*, **28 (4)**, 1630–1648.

Andrews, T., J. M. Gregory, M. J. Webb, and K. E. Taylor, 2012: Forcing, feedbacks and climate sensitivity in cmip5 coupled atmosphere-ocean climate models. *Geophysical research letters*, **39 (9)**.

Andrews, T., and M. J. Webb, 2018: The dependence of global cloud and lapse rate feedbacks on the spatial structure of tropical pacific warming. *Journal of Climate*, **31 (2)**, 641–654.

Andrews, T., and Coauthors, 2018: Accounting for changing temperature patterns increases historical estimates of climate sensitivity. *Geophysical Research Letters*, **45 (16)**, 8490–8499.

Andrews, T., and Coauthors, 2019: Forcings, feedbacks, and climate sensitivity in hadgem3-gc3. 1 and ukesm1. *Journal of Advances in Modeling Earth Systems*, **11 (12)**, 4377–4394.

Arora, V., and Coauthors, 2009: The effect of terrestrial photosynthesis down regulation on the twentieth-century carbon budget simulated with the cccma earth system model. *Journal of Climate*, **22 (22)**, 6066–6088.

Arora, V., and Coauthors, 2011: Carbon emission limits required to satisfy future representative concentration pathways of greenhouse gases. *Geophysical Research Letters*, **38 (5)**.

Betts, A. K., 1987: Thermodynamic constraint on the cloud liquid water feedback in climate models. *Journal of Geophysical Research: Atmospheres*, **92 (D7)**, 8483–8485.

Bjordal, J., T. Storelvmo, K. Alterskjær, and T. Carlsen, 2020: Equilibrium climate sensitivity above 5 ° c plausible due to state-dependent cloud feedback. *Nature Geoscience*, 1–4.

Block, K., and T. Mauritsen, 2013: Forcing and feedback in the mpi-esm-lr coupled model under abruptly quadrupled co2. *Journal of Advances in Modeling Earth Systems*, **5 (4)**, 676–691.

Blossey, P. N., and Coauthors, 2013: Marine low cloud sensitivity to an idealized climate change: The cgils les intercomparison. *Journal of Advances in Modeling Earth Systems*, **5 (2)**, 234–258.

Bodas-Salcedo, A., J. Mulcahy, T. Andrews, K. Williams, M. Ringer, P. Field, and G. Elsaesser, 2019: Strong dependence of atmospheric feedbacks on mixed-phase microphysics and aerosol-cloud interactions in hadgem3. *Journal of Advances in Modeling Earth Systems*, **11 (6)**, 1735–1758.

Bodas-Salcedo, A., and Coauthors, 2011: Cosp: Satellite simulation software for model assessment. *Bulletin of the American Meteorological Society*, **92 (8)**, 1023–1043.

Boer, G., and B. Yu, 2003: Climate sensitivity and climate state. *Climate Dynamics*, **21 (2)**, 167–176.

Bony, S., and Coauthors, 2015: Clouds, circulation and climate sensitivity. *Nature Geoscience*, **8 (4)**, 261–268.

Boucher, O., C. Kleinschmitt, and G. Myhre, 2017: Quasi-additivity of the radiative effects of marine cloud brightening and stratospheric sulfate aerosol injection. *Geophysical Research Letters*, **44 (21)**, 11–158.

Bouillon, S., M. A. M. Maqueda, V. Legat, and T. Fichefet, 2009: An elastic–viscous–plastic sea ice model formulated on arakawa b and c grids. *Ocean Modelling*, **27 (3-4)**, 174–184.

Bretherton, C. S., and P. N. Blossey, 2014: Low cloud reduction in a greenhouse-warmed climate: Results from lagrangian les of a subtropical marine cloudiness transition. *Journal of Advances in Modeling Earth Systems*, **6 (1)**, 91–114.

Bretherton, C. S., P. N. Blossey, and C. R. Jones, 2013: Mechanisms of marine low cloud sensitivity to idealized climate perturbations: A single-les exploration extending the cgils cases. *Journal of Advances in Modeling Earth Systems*, **5 (2)**, 316–337.

Brient, F., and T. Schneider, 2016: Constraints on climate sensitivity from space-based measurements of low-cloud reflection. *Journal of Climate*, **29 (16)**, 5821–5835.

Caldeira, K., and G. Bala, 2017: Reflecting on 50 years of geoengineering research. *Earth's Future*, **5 (1)**, 10–17.

Caldwell, P. M., M. D. Zelinka, K. E. Taylor, and K. Marvel, 2016: Quantifying the sources of intermodel spread in equilibrium climate sensitivity. *Journal of Climate*, **29 (2)**, 513–524.

Ceppi, P., F. Brient, M. D. Zelinka, and D. L. Hartmann, 2017: Cloud feedback mechanisms and their representation in global climate models. *Wiley Interdisciplinary Reviews: Climate Change*, **8 (4)**, e465.

Cess, R. D., and Coauthors, 1989: Interpretation of cloud-climate feedback as produced by 14 atmospheric general circulation models. *Science*, **245 (4917)**, 513–516.

Cess, R. D., and Coauthors, 1990: Intercomparison and interpretation of climate feedback processes in 19 atmospheric general circulation models. *Journal of Geophysical Research: Atmospheres*, **95 (D10)**, 16 601–16 615.

Charney, J. G., and Coauthors, 1979: *Carbon Dioxide and Climate: A Scientific Assessment*. National Academies Press, Washington, DC, doi: 10.17226/12181.

Chung, E.-S., and B. J. Soden, 2015: An assessment of direct radiative forcing, radiative adjustments, and radiative feedbacks in coupled ocean–atmosphere models. *Journal of Climate*, **28 (10)**, 4152–4170.

Clement, A. C., R. Burgman, and J. R. Norris, 2009: Observational and model evidence for positive low-level cloud feedback. *Science*, **325 (5939)**, 460–464.

Collins, W. D., and Coauthors, 2004: Description of the ncar community atmosphere model (cam 3.0). *NCAR Tech. Note NCAR/TN-464+ STR*, **226**, 1326–1334.

Crutzen, P. J., 2006: Albedo enhancement by stratospheric sulfur injections: a contribution to resolve a policy dilemma? *Climatic change*, **77 (3-4)**, 211.

Danabasoglu, G., and Coauthors, 2020: The community earth system model version 2 (cesm2). *Journal of Advances in Modeling Earth Systems*, **12 (2)**, e2019MS001 916.

Davidson, P., C. Burgoyne, H. Hunt, and M. Causier, 2012: Lifting options for stratospheric aerosol geoengineering: advantages of tethered balloon systems. *Philosophical Transactions of the Royal Society A: Mathematical, Physical and Engineering Sciences*, **370 (1974)**, 4263–4300.

Dong, Y., K. C. Armour, M. D. Zelinka, C. Proistosescu, D. S. Battisti, C. Zhou, and T. Andrews, 2020: Intermodel spread in the pattern effect and its contribution to climate sensitivity in cmip5 and cmip6 models. *Journal of Climate*, **33 (18)**, 7755–7775.

Doutriaux-Boucher, M., M. Webb, J. M. Gregory, and O. Boucher, 2009: Carbon dioxide induced stomatal closure increases radiative forcing via a rapid reduction in low cloud. *Geophysical Research Letters*, **36 (2)**.

Dufresne, J.-L., and S. Bony, 2008: An assessment of the primary sources of spread of global warming estimates from coupled atmosphere–ocean models. *Journal of Climate*, **21 (19)**, 5135–5144.

Eitzen, Z. A., K.-M. Xu, and T. Wong, 2011: An estimate of low-cloud feedbacks from variations of cloud radiative and physical properties with sea surface temperature on interannual time scales. *Journal of climate*, **24 (4)**, 1106–1121.

Eyring, V., S. Bony, G. A. Meehl, C. A. Senior, B. Stevens, R. J. Stouffer, and K. E. Taylor, 2016: Overview of the coupled model intercomparison project phase 6 (cmip6) experimental design and organization. *Geoscientific Model Development*, **9 (5)**, 1937–1958.

Fichefet, T., and M. M. Maqueda, 1997: Sensitivity of a global sea ice model to the treatment of ice thermodynamics and dynamics. *Journal of Geophysical Research: Oceans*, **102 (C6)**, 12 609–12 646.

Fletcher, C. G., B. Kravitz, and B. Badawy, 2018: Quantifying uncertainty from aerosol and atmospheric parameters and their impact on climate sensitivity. *Atmospheric Chemistry and Physics*, **18 (23)**, 17 529–17 543.

Fletcher, C. G., W. McNally, J. G. Virgin, and F. King, 2022: Toward efficient calibration of higher-resolution earth system models. *Journal of Advances in Modeling Earth Systems*, **14 (7)**, e2021MS002 836.

Flynn, C. M., and T. Mauritsen, 2020: On the climate sensitivity and historical warming evolution in recent coupled model ensembles. *Atmospheric Chemistry & Physics*, **20 (13)**, 7829–7842.

Forster, P., and Coauthors, 2021: The earth's energy budget, climate feedbacks, and climate sensitivity.

Forster, P. M., T. Andrews, P. Good, J. M. Gregory, L. S. Jackson, and M. Zelinka, 2013: Evaluating adjusted forcing and model spread for historical and future scenarios in the cmip5 generation of climate models. *Journal of Geophysical Research: Atmospheres*, **118 (3)**, 1139–1150.

Forster, P. M., and K. P. Shine, 1997: Radiative forcing and temperature trends from stratospheric ozone changes. *Journal of Geophysical Research: Atmospheres*, **102 (D9)**, 10 841–10 855.

Forster, P. M., and Coauthors, 2023: Indicators of global climate change 2022: annual update of large-scale indicators of the state of the climate system and human influence. *Earth System Science Data*, **15 (6)**, 2295–2327.

Fueglistaler, S., 2019: Observational evidence for two modes of coupling between sea surface temperatures, tropospheric temperature profile, and shortwave cloud radiative effect in the tropics. *Geophysical Research Letters*, **46 (16)**, 9890–9898.

Gent, P. R., F. O. Bryan, G. Danabasoglu, S. C. Doney, W. R. Holland, W. G. Large, and J. C. McWilliams, 1998: The ncar climate system model global ocean component. *Journal of Climate*, **11 (6)**, 1287–1306.

Gent, P. R., and Coauthors, 2011: The community climate system model version 4. *Journal of climate*, **24 (19)**, 4973–4991.

Gettelman, A., and S. Sherwood, 2016: Processes responsible for cloud feedback. *Current Climate Change Reports*, **2 (4)**, 179–189.

Gettelman, A., and Coauthors, 2019: High climate sensitivity in the community earth system model version 2 (cesm2). *Geophysical Research Letters*, **46 (14)**, 8329–8337.

Glienke, S., P. J. Irvine, and M. G. Lawrence, 2015: The impact of geoengineering on vegetation in experiment g1 of the geomip. *Journal of Geophysical Research: Atmospheres*, **120 (19)**, 10–196.

Golaz, J.-C., L. W. Horowitz, and H. Levy, 2013: Cloud tuning in a coupled climate model: Impact on 20th century warming. *Geophysical Research Letters*, **40 (10)**, 2246–2251.

Golaz, J.-C., M. Salzmann, L. J. Donner, L. W. Horowitz, Y. Ming, and M. Zhao, 2011: Sensitivity of the aerosol indirect effect to subgrid variability in the cloud parameterization of the gfdl atmosphere general circulation model am3. *Journal of Climate*, **24 (13)**, 3145–3160.

Golaz, J.-C., and Coauthors, 2019: The doe e3sm coupled model version 1: Overview and evaluation at standard resolution. *Journal of Advances in Modeling Earth Systems*, **11 (7)**, 2089–2129.

Goosse, H., and Coauthors, 2018: Quantifying climate feedbacks in polar regions. *Nature communications*, **9 (1)**, 1–13.

Gregory, J., and Coauthors, 2004: A new method for diagnosing radiative forcing and climate sensitivity. *Geophysical research letters*, **31 (3)**.

Hansen, J., A. Lacis, D. Rind, G. Russell, P. Stone, I. Fung, R. Ruedy, and J. Lerner, 1984: Climate sensitivity: Analysis of feedback mechanisms. *feedback*, **1**, 1–3.

Hansen, J., M. Sato, and R. Ruedy, 1997: Radiative forcing and climate response. *Journal of Geophysical Research: Atmospheres*, **102 (D6)**, 6831–6864.

Hansen, J., and Coauthors, 2005: Efficacy of climate forcings. *Journal of geophysical research: atmospheres*, **110 (D18)**.

Hartmann, D. L., 2015: *Global physical climatology*, Vol. 103. Newnes.

Henry, M., and T. M. Merlis, 2020: Forcing dependence of atmospheric lapse rate changes dominates residual polar warming in solar radiation management climate scenarios. *Geophysical Research Letters*, **47 (15)**, e2020GL087 929.

Huang, Y., X. Tan, and Y. Xia, 2016: Inhomogeneous radiative forcing of homogeneous greenhouse gases. *Journal of Geophysical Research: Atmospheres*, **121 (6)**, 2780–2789.

Huang, Y., Y. Xia, and X. Tan, 2017: On the pattern of co2 radiative forcing and poleward energy transport. *Journal of Geophysical Research: Atmospheres*, **122 (20)**, 10–578.

Huneeus, N., and Coauthors, 2014: Forcings and feedbacks in the geomip ensemble for a reduction in solar irradiance and increase in co2. *Journal of Geophysical Research: Atmospheres*, **119 (9)**, 5226–5239.

Hunke, E., and W. Lipscomb, 2008: The los alamos sea ice model user's manual, version 4. *Los Alamos National Laboratory Tech. Rep.*

Hurrell, J. W., J. J. Hack, D. Shea, J. M. Caron, and J. Rosinski, 2008: A new sea surface temperature and sea ice boundary dataset for the community atmosphere model. *Journal of Climate*, **21 (19)**, 5145–5153.

Hurrell, J. W., and Coauthors, 2013: The community earth system model: a framework for collaborative research. *Bulletin of the American Meteorological Society*, **94 (9)**, 1339–1360.

IPCC, 2023: Longer report. *Synthesis Report of the IPCC Sixth Assessment Report*, H. Lee, K. Calvin, D. Dsgupta, K. Gerhard, A. Mukherji, P. Thorne, C. Trisos, J. Romero, P. Aldunce, K. Barret et al., Eds., Cambridge University Press, Cambridge, UK and New York, NY, USA, URL https://www.ipcc.ch/report/ar6/syr/downloads/report/IPCC_AR6_SYR_LongerReport.pdf.

Irvine, P. J., B. Kravitz, M. G. Lawrence, and H. Muri, 2016: An overview of the earth system science of solar geoengineering. *Wiley Interdisciplinary Reviews: Climate Change*, **7 (6)**, 815–833.

Jones, A., and Coauthors, 2013: The impact of abrupt suspension of solar radiation management (termination effect) in experiment g2 of the geoengineering model intercomparison project (geomip). *Journal of Geophysical Research: Atmospheres*, **118 (17)**, 9743–9752.

Jonko, A. K., K. M. Shell, B. M. Sanderson, and G. Danabasoglu, 2012: Climate feedbacks in ccsm3 under changing co 2 forcing. part i: Adapting the linear radiative kernel technique to feedback calculations for a broad range of forcings. *Journal of Climate*, **25 (15)**, 5260–5272.

Jonko, A. K., K. M. Shell, B. M. Sanderson, and G. Danabasoglu, 2013: Climate feedbacks in ccsm3 under changing co 2 forcing. part ii: Variation of climate feedbacks and sensitivity with forcing. *Journal of Climate*, **26 (9)**, 2784–2795.

Kamae, Y., and M. Watanabe, 2012: On the robustness of tropospheric adjustment in cmip5 models. *Geophysical Research Letters*, **39 (23)**.

Kamae, Y., and M. Watanabe, 2013: Tropospheric adjustment to increasing co 2: Its timescale and the role of land–sea contrast. *Climate Dynamics*, **41**, 3007–3024.

Kaur, H., G. Bala, and A. K. Seshadri, 2023: Why is climate sensitivity for solar forcing smaller than for an equivalent co 2 forcing? *Journal of Climate*, **36 (3)**, 775–789.

Keith, D. W., 2000: Geoengineering the climate: History and prospect. *Annual review of energy and the environment*, **25 (1)**, 245–284.

Keith, D. W., and D. G. MacMartin, 2015: A temporary, moderate and responsive scenario for solar geoengineering. *Nature Climate Change*, **5 (3)**, 201–206.

Keith, D. W., D. K. Weisenstein, J. A. Dykema, and F. N. Keutsch, 2016: Stratospheric solar geoengineering without ozone loss. *Proceedings of the National academy of Sciences*, **113 (52)**, 14 910–14 914.

Khairoutdinov, M., and Y. Kogan, 2000: A new cloud physics parameterization in a large-eddy simulation model of marine stratocumulus. *Monthly weather review*, **128 (1)**, 229–243.

Kiehl, J. T., and K. E. Trenberth, 1997: Earth's annual global mean energy budget. *Bulletin of the American meteorological society*, **78 (2)**, 197–208.

Klein, S. A., A. Hall, J. R. Norris, and R. Pincus, 2017: Low-cloud feedbacks from cloud-controlling factors: A review. *Shallow clouds, water vapor, circulation, and climate sensitivity*, 135–157.

Klein, S. A., and D. L. Hartmann, 1993: The seasonal cycle of low stratiform clouds. *Journal of Climate*, **6 (8)**, 1587–1606.

Klein, S. A., and C. Jakob, 1999: Validation and sensitivities of frontal clouds simulated by the ecmwf model. *Monthly weather review*, **127 (10)**, 2514–2531.

Klocke, D., J. Quaas, and B. Stevens, 2013: Assessment of different metrics for physical climate feedbacks. *Climate dynamics*, **41**, 1173–1185.

Knutti, R., and M. A. Rugenstein, 2015: Feedbacks, climate sensitivity and the limits of linear models. *Philosophical Transactions of the Royal Society A: Mathematical, Physical and Engineering Sciences*, **373 (2054)**, 20150 146.

Knutti, R., M. A. Rugenstein, and G. C. Hegerl, 2017: Beyond equilibrium climate sensitivity. *Nature Geoscience*, **10 (10)**, 727–736.

Kramer, R. J., H. He, B. J. Soden, L. Oreopoulos, G. Myhre, P. M. Forster, and C. J. Smith, 2021: Observational evidence of increasing global radiative forcing. *Geophysical Research Letters*, **48 (7)**, e2020GL091 585.

Kravitz, B., and D. G. MacMartin, 2020: Uncertainty and the basis for confidence in solar geoengineering research. *Nature Reviews Earth & Environment*, **1 (1)**, 64–75.

Kravitz, B., D. G. MacMartin, D. T. Leedal, P. J. Rasch, and A. J. Jarvis, 2014: Explicit feedback and the management of uncertainty in meeting climate objectives with solar geoengineering. *Environmental Research Letters*, **9 (4)**, 044 006.

Kravitz, B., D. G. MacMartin, M. J. Mills, J. H. Richter, S. Tilmes, J.-F. Lamarque, J. J. Tribbia, and F. Vitt, 2017: First simulations of designing stratospheric sulfate aerosol geoengineering to meet multiple simultaneous climate objectives. *Journal of Geophysical Research: Atmospheres*, **122 (23)**, 12–616.

Kravitz, B., D. G. MacMartin, H. Wang, and P. J. Rasch, 2016: Geoengineering as a design problem. *Earth System Dynamics*, **7 (2)**, 469–497.

Kravitz, B., A. Robock, O. Boucher, H. Schmidt, K. Taylor, G. Stenchikov, and S. Michael, 2011a: Specifications for geomip experiments g1 through g4. *Ben Kravitz*.

Kravitz, B., A. Robock, O. Boucher, H. Schmidt, K. E. Taylor, G. Stenchikov, and M. Schulz, 2011b: The geoengineering model intercomparison project (geomip). *Atmospheric Science Letters*, **12 (2)**, 162–167.

Kravitz, B., and Coauthors, 2013: Climate model response from the geoengineering model intercomparison project (geomip). *Journal of Geophysical Research: Atmospheres*, **118 (15)**, 8320–8332.

Kravitz, B., and Coauthors, 2013b: Sea spray geoengineering experiments in the geoengineering model intercomparison project (geomip): Experimental design and preliminary results. *Journal of Geophysical Research: Atmospheres*, **118 (19)**, 11–175.

Kravitz, B., and Coauthors, 2015: The geoengineering model intercomparison project phase 6 (geomip6): Simulation design and preliminary results. *Geoscientific Model Development*, **8 (10)**, 3379–3392.

Kravitz, B., and Coauthors, 2021: Comparing different generations of idealized solar geoengineering simulations in the geoengineering model intercomparison project (geomip). *Atmospheric Chemistry and Physics*, **21 (6)**, 4231–4247.

Kuang, Z., and Y. L. Yung, 2000: Observed albedo decrease related to the spring snow retreat. *Geophysical research letters*, **27 (9)**, 1299–1302.

Latham, J., 1990: Control of global warming? *Nature*, **347 (6291)**, 339–340.

Latham, J., and Coauthors, 2012: Marine cloud brightening. *Philosophical Transactions of the Royal Society A: Mathematical, Physical and Engineering Sciences*, **370 (1974)**, 4217–4262.

Lawrence, D. M., and Coauthors, 2011: Parameterization improvements and functional and structural advances in version 4 of the community land model. *Journal of Advances in Modeling Earth Systems*, **3 (1)**.

Lenton, T. M., and N. E. Vaughan, 2009: The radiative forcing potential of different climate geoengineering options. *Atmospheric Chemistry and Physics*, **9 (15)**, 5539–5561.

Liu, Y., and P. H. Daum, 2004: Parameterization of the autoconversion process. part i: Analytical formulation of the kessler-type parameterizations. *Journal of the atmospheric sciences*, **61 (13)**, 1539–1548.

MacMartin, D. G., B. Kravitz, D. W. Keith, and A. Jarvis, 2014: Dynamics of the coupled human–climate system resulting from closed-loop control of solar geoengineering. *Climate dynamics*, **43**, 243–258.

MacMartin, D. G., K. L. Ricke, and D. W. Keith, 2018: Solar geoengineering as part of an overall strategy for meeting the 1.5 c paris target. *Philosophical Transactions of the Royal Society A: Mathematical, Physical and Engineering Sciences*, **376 (2119)**, 20160 454.

MacMynowski, D. G., H.-J. Shin, and K. Caldeira, 2011: The frequency response of temperature and precipitation in a climate model. *Geophysical Research Letters*, **38 (16)**.

Madec, G., 2012: Nemo ocean engine, version 3.4. *Note du Pôle de modélisation, Institut Pierre-Simon Laplace (IPSL), France*, **(27)**, 367.

Manabe, S., and R. T. Wetherald, 1975: The effects of doubling the co 2 concentration on the climate of a general circulation model. *Journal of Atmospheric Sciences*, **32 (1)**, 3–15.

McLaren, D., and O. Corry, 2021: The politics and governance of research into solar geoengineering. *Wiley Interdisciplinary Reviews: Climate Change*, **12 (3)**, e707.

Mitchell, D. L., and W. Finnegan, 2009: Modification of cirrus clouds to reduce global warming. *Environmental Research Letters*, **4 (4)**, 045 102.

Modak, A., G. Bala, L. Cao, and K. Caldeira, 2016: Why must a solar forcing be larger than a co2 forcing to cause the same global mean surface temperature change? *Environmental Research Letters*, **11 (4)**, 044 013.

Mulcahy, J., and Coauthors, 2018: Improved aerosol processes and effective radiative forcing in hadgem3 and ukesm1. *Journal of Advances in Modeling Earth Systems*, **10 (11)**, 2786–2805.

Niemeier, U., H. Schmidt, K. Alterskjær, and J. Kristjánsson, 2013: Solar irradiance reduction via climate engineering: Impact of different techniques on the energy balance and the hydrological cycle. *Journal of Geophysical Research: Atmospheres*, **118 (21)**, 11–905.

Pendergrass, A. G., A. Conley, and F. M. Vitt, 2018: Surface and top-of-atmosphere radiative feedback kernels for cesm-cam5. *Earth System Science Data*, **10 (1)**, 317–324.

Pincus, R., P. M. Forster, and B. Stevens, 2016: The radiative forcing model intercomparison project (rfmip): experimental protocol for cmip6. *Geoscientific Model Development*, **9 (9)**, 3447–3460.

Pruppacher, H. R., and J. D. Klett, 1980: Microphysics of clouds and precipitation. *Nature*, **284 (5751)**, 88–88.

Qu, X., A. Hall, S. A. Klein, and P. M. Caldwell, 2014: On the spread of changes in marine low cloud cover in climate model simulations of the 21st century. *Climate dynamics*, **42 (9-10)**, 2603–2626.

Qu, X., A. Hall, S. A. Klein, and A. M. DeAngelis, 2015: Positive tropical marine low-cloud cover feedback inferred from cloud-controlling factors. *Geophysical Research Letters*, **42 (18)**, 7767–7775.

Ramanswamy, V., and Coauthors, 1991: Radiative forcing of climate. *NASA, Washington, Scientific Assessment of Ozone Depletion: 1991*.

Rasch, P. J., S. Tilmes, R. P. Turco, A. Robock, L. Oman, C.-C. Chen, G. L. Stenchikov, and R. R. Garcia, 2008: An overview of geoengineering of climate using stratospheric sulphate aerosols. *Philosophical Transactions of the Royal Society A: Mathematical, Physical and Engineering Sciences*, **366 (1882)**, 4007–4037.

Richter, H., Jadwiga, and Coauthors, 2018: Stratospheric response in the first geoengineering simulation meeting multiple surface climate objectives. *Journal of Geophysical Research: Atmospheres*, **123 (11)**, 5762–5782.

Rieck, M., L. Nuijens, and B. Stevens, 2012: Marine boundary layer cloud feedbacks in a constant relative humidity atmosphere. *Journal of the Atmospheric Sciences*, **69 (8)**, 2538–2550.

Robock, A., 2008: 20 reasons why geoengineering may be a bad idea. *Bulletin of the Atomic Scientists*, **64 (2)**, 14–18.

Robock, A., A. Marquardt, B. Kravitz, and G. Stenchikov, 2009: Benefits, risks, and costs of stratospheric geoengineering. *Geophysical Research Letters*, **36 (19)**.

Rose, B. E., K. C. Armour, D. S. Battisti, N. Feldl, and D. D. Koll, 2014: The dependence of transient climate sensitivity and radiative feedbacks on the spatial pattern of ocean heat uptake. *Geophysical Research Letters*, **41 (3)**, 1071–1078.

Russotto, R. D., and T. P. Ackerman, 2018: Changes in clouds and thermodynamics under solar geoengineering and implications for required solar reduction. *Atmospheric Chemistry and Physics*, **18 (16)**, 11 905–11 925.

Saint-Lu, M., S. Bony, and J.-L. Dufresne, 2022: Clear-sky control of anvils in response to increased co2 or surface warming or volcanic eruptions. *npj climate and atmospheric science*, **5 (1)**, 78.

Salvi, P., P. Ceppi, and J. M. Gregory, 2021: Interpreting the dependence of cloud-radiative adjustment on forcing agent. *Geophysical Research Letters*, **48 (18)**, e2021GL093 616.

Schiffer, R. A., and W. B. Rossow, 1983: The international satellite cloud climatology project (isccp): The first project of the world climate research programme. *Bulletin of the American Meteorological Society*, **64 (7)**, 779–784.

Schmidt, H., and Coauthors, 2012: Solar irradiance reduction to counteract radiative forcing from a quadrupling of co 2: climate responses simulated by four earth system models. *Earth System Dynamics*, **3 (1)**, 63–78.

Scott, R. C., T. A. Myers, J. R. Norris, M. D. Zelinka, S. A. Klein, M. Sun, and D. R. Doelling, 2020: Observed sensitivity of low-cloud radiative effects to meteorological perturbations over the global oceans. *Journal of Climate*, **33 (18)**, 7717–7734.

Senior, C., and W. Ingram, 1989: C02 and climate: A missing feedback. *Nature*, **341**, 132–134.

Shell, K. M., J. T. Kiehl, and C. A. Shields, 2008: Using the radiative kernel technique to calculate climate feedbacks in ncar's community atmospheric model. *Journal of Climate*, **21 (10)**, 2269–2282.

Shepherd, J. G., 2009: *Geoengineering the climate: science, governance and uncertainty*. Royal Society.

Sherwood, S., and Coauthors, 2020: An assessment of earth's climate sensitivity using multiple lines of evidence. *Reviews of Geophysics*, **58 (4)**, e2019RG000 678.

Sherwood, S. C., S. Bony, O. Boucher, C. Bretherton, P. M. Forster, J. M. Gregory, and B. Stevens, 2015: Adjustments in the forcing-feedback framework for understanding climate change. *Bulletin of the American Meteorological Society*, **96 (2)**, 217–228.

Sherwood, S. C., S. Bony, and J.-L. Dufresne, 2014: Spread in model climate sensitivity traced to atmospheric convective mixing. *Nature*, **505 (7481)**, 37–42.

Shine, K., 1986: On the modelled thermal response of the antarctic stratosphere to a depletion of ozone. *Geophysical research letters*, **13 (12)**, 1331–1334.

Singh, H., N. Feldl, J. E. Kay, and A. L. Morrison, 2022: Climate sensitivity is sensitive to changes in ocean heat transport. *Journal of Climate*, **35 (9)**, 2653–2674.

Slingo, A., 1989: A gcm parameterization for the shortwave radiative properties of water clouds. *Journal of the Atmospheric Sciences*, **46 (10)**, 1419–1427.

Smith, C., and Coauthors, 2018: Understanding rapid adjustments to diverse forcing agents. *Geophysical Research Letters*, **45 (21)**, 12–023.

Smith, C., and Coauthors, 2020a: Effective radiative forcing and adjustments in cmip6 models. *Atmospheric Chemistry and Physics*, **20 (16)**, 9591–9618.

Smith, C. J., 2018: Hadgem2 radiative kernels. URL https://doi.org/10.5518/406.

Smith, C. J., R. J. Kramer, and A. Sima, 2020b: The hadgem3-ga7. 1 radiative kernel: the importance of a well-resolved stratosphere. *Earth System Science Data*, **12 (3)**, 2157–2168.

Smith, R., and Coauthors, 2010: The parallel ocean program (pop) reference manual ocean component of the community climate system model (ccsm) and community earth system model (cesm). *LAUR-01853*, **141**, 1–140.

Smith, W., and G. Wagner, 2018: Stratospheric aerosol injection tactics and costs in the first 15 years of deployment. *Environmental Research Letters*, **13 (12)**, 124 001.

Soden, B. J., A. J. Broccoli, and R. S. Hemler, 2004: On the use of cloud forcing to estimate cloud feedback. *Journal of climate*, **17 (19)**, 3661–3665.

Soden, B. J., and I. M. Held, 2006: An assessment of climate feedbacks in coupled ocean–atmosphere models. *Journal of climate*, **19 (14)**, 3354–3360.

Soden, B. J., I. M. Held, R. Colman, K. M. Shell, J. T. Kiehl, and C. A. Shields, 2008: Quantifying climate feedbacks using radiative kernels. *Journal of Climate*, **21 (14)**, 3504–3520.

Solomon, S., 1999: Stratospheric ozone depletion: A review of concepts and history. *Reviews of Geophysics*, **37 (3)**, 275–316.

Stenchikov, G. L., I. Kirchner, A. Robock, H.-F. Graf, J. C. Antuna, R. G. Grainger, A. Lambert, and L. Thomason, 1998: Radiative forcing from the 1991 mount pinatubo volcanic eruption. *Journal of Geophysical Research: Atmospheres*, **103 (D12)**, 13 837–13 857.

Stevens, B., S. C. Sherwood, S. Bony, and M. J. Webb, 2016: Prospects for narrowing bounds on earth's equilibrium climate sensitivity. *Earth's Future*, **4 (11)**, 512–522.

Swart, N. C., and Coauthors, 2019: The canadian earth system model version 5 (canesm5. 0.3). *Geoscientific Model Development*, **12 (11)**, 4823–4873.

Tan, I., L. Oreopoulos, and N. Cho, 2019: The role of thermodynamic phase shifts in cloud optical depth variations with temperature. *Geophysical Research Letters*, **46 (8)**, 4502–4511.

Tan, I., T. Storelvmo, and M. D. Zelinka, 2016: Observational constraints on mixed-phase clouds imply higher climate sensitivity. *Science*, **352 (6282)**, 224–227.

Tang, T., and Coauthors, 2019: Comparison of effective radiative forcing calculations using multiple methods, drivers, and models. *Journal of Geophysical Research: Atmospheres*, **124 (8)**, 4382–4394.

Taylor, K. E., R. J. Stouffer, and G. A. Meehl, 2012: An overview of cmip5 and the experiment design. *Bulletin of the American Meteorological Society*, **93 (4)**, 485–498.

Tilmes, S., R. R. Garcia, D. E. Kinnison, A. Gettelman, and P. J. Rasch, 2009: Impact of geoengineered aerosols on the troposphere and stratosphere. *Journal of Geophysical Research: Atmospheres*, **114 (D12)**.

Tilmes, S., and Coauthors, 2018: Cesm1 (waccm) stratospheric aerosol geoengineering large ensemble project. *Bulletin of the American Meteorological Society*, **99 (11)**, 2361–2371.

Tsushima, Y., and Coauthors, 2006: Importance of the mixed-phase cloud distribution in the control climate for assessing the response of clouds to carbon dioxide increase: a multi-model study. *Climate Dynamics*, **27 (2-3)**, 113–126.

Van der Dussen, J., S. De Roode, S. Dal Gesso, and A. Siebesma, 2015: An les model study of the influence of the free tropospheric thermodynamic conditions on the stratocumulus response to a climate perturbation. *Journal of Advances in Modeling Earth Systems*, **7 (2)**, 670–691.

Verseghy, D. L., 2000: The canadian land surface scheme (class): its history and future. *Atmosphere-Ocean*, **38 (1)**, 1–13.

Vial, J., J.-L. Dufresne, and S. Bony, 2013: On the interpretation of inter-model spread in cmip5 climate sensitivity estimates. *Climate Dynamics*, **41 (11-12)**, 3339–3362.

Virgin, J., and C. Fletcher, 2022: On the linearity of external forcing response in solar geoengineering experiments. *Geophysical Research Letters*, **49 (15)**, e2022GL100 200.

Virgin, J., and C. Fletcher, 2023: Declining geoengineering efficacy caused by cloud feedbacks in transient solar dimming experiments. *Manuscript Submitted to Journal of Climate*.

Virgin, J. G., C. G. Fletcher, J. N. Cole, K. von Salzen, and T. Mitovski, 2021: Cloud feedbacks from canesm2 to canesm5. 0 and their influence on climate sensitivity. *Geoscientific Model Development*, **14 (9)**, 5355–5372.

Visioni, D., D. G. MacMartin, and B. Kravitz, 2021a: Is turning down the sun a good proxy for stratospheric sulfate geoengineering? *Journal of Geophysical Research: Atmospheres*, **126 (5)**, e2020JD033 952.

Visioni, D., and Coauthors, 2021b: Identifying the sources of uncertainty in climate model simulations of solar radiation modification with the g6sulfur and g6solar geoengineering model intercomparison project (geomip) simulations. *Atmospheric Chemistry and Physics*, **21 (13)**, 10 039–10 063.

von Salzen, K., and Coauthors, 2013: The canadian fourth generation atmospheric global climate model (canam4). part i: representation of physical processes. *Atmosphere-Ocean*, **51 (1)**, 104–125.

Wang, Y., and Y. Huang, 2020: Understanding the atmospheric temperature adjustment to co2 perturbation at the process level. *Journal of Climate*, **33 (3)**, 787–803.

Webb, M. J., and Coauthors, 2017: The cloud feedback model intercomparison project (cfmip) contribution to cmip6. *Geoscientific Model Development*, **2017**, 359–384.

Wetherald, R., and S. Manabe, 1988: Cloud feedback processes in a general circulation model. *Journal of the Atmospheric Sciences*, **45 (8)**, 1397–1416.

Wetherald, R. T., and S. Manabe, 1975: The effects of changing the solar constant on the climate of a general circulation model. *Journal of the Atmospheric Sciences*, **32 (11)**, 2044–2059.

Wigley, T. M., 2006: A combined mitigation/geoengineering approach to climate stabilization. *Science*, **314 (5798)**, 452–454.

Wood, R., 2005: Drizzle in stratiform boundary layer clouds. part ii: Microphysical aspects. *Journal of the atmospheric sciences*, **62 (9)**, 3034–3050.

Wood, R., and P. N. Blossey, 2005: Comments on "parameterization of the autoconversion process. part i: Analytical formulation of the kessler-type parameterizations". *Journal of the Atmospheric Sciences*, **62 (8)**, 3003–3006.

Wood, R., and C. S. Bretherton, 2006: On the relationship between stratiform low cloud cover and lower-tropospheric stability. *Journal of climate*, **19 (24)**, 6425–6432.

Zahariev, K., J. R. Christian, and K. L. Denman, 2008: Preindustrial, historical, and fertilization simulations using a global ocean carbon model with new parameterizations of iron limitation, calcification, and n2 fixation. *Progress in Oceanography*, **77 (1)**, 56–82.

Zelinka, M. D., K. M. Grise, S. A. Klein, C. Zhou, A. M. DeAngelis, and M. W. Christensen, 2018: Drivers of the low-cloud response to poleward jet shifts in the north pacific in observations and models. *Journal of Climate*, **31 (19)**, 7925–7947.

Zelinka, M. D., and D. L. Hartmann, 2010: Why is longwave cloud feedback positive? *Journal of Geophysical Research: Atmospheres*, **115 (D16)**.

Zelinka, M. D., S. A. Klein, and D. L. Hartmann, 2012a: Computing and partitioning cloud feedbacks using cloud property histograms. part i: Cloud radiative kernels. *Journal of Climate*, **25 (11)**, 3715–3735.

Zelinka, M. D., S. A. Klein, and D. L. Hartmann, 2012b: Computing and partitioning cloud feedbacks using cloud property histograms. part ii: Attribution to changes in cloud amount, altitude, and optical depth. *Journal of Climate*, **25 (11)**, 3736–3754.

Zelinka, M. D., S. A. Klein, Y. Qin, and T. A. Myers, 2022: Evaluating climate models' cloud feedbacks against expert judgment. *Journal of Geophysical Research: Atmospheres*, **127 (2)**, e2021JD035 198.

Zelinka, M. D., S. A. Klein, K. E. Taylor, T. Andrews, M. J. Webb, J. M. Gregory, and P. M. Forster, 2013: Contributions of different cloud types to feedbacks and rapid adjustments in cmip5. *Journal of Climate*, **26 (14)**, 5007–5027.

Zelinka, M. D., T. A. Myers, D. T. McCoy, S. Po-Chedley, P. M. Caldwell, P. Ceppi, S. A. Klein, and K. E. Taylor, 2020: Causes of higher climate sensitivity in cmip6 models. *Geophysical Research Letters*, **47 (1)**.

Zelinka, M. D., C. Zhou, and S. A. Klein, 2016: Insights from a refined decomposition of cloud feedbacks. *Geophysical Research Letters*, **43 (17)**, 9259–9269.

Zhang, M., and Y. Huang, 2014: Radiative forcing of quadrupling co2. *Journal of Climate*, **27 (7)**, 2496–2508.

Zhou, C., M. D. Zelinka, A. E. Dessler, and S. A. Klein, 2015: The relationship between interannual and long-term cloud feedbacks. *Geophysical Research Letters*, **42 (23)**, 10–463.

Zhou, C., M. D. Zelinka, and S. A. Klein, 2017: Analyzing the dependence of global cloud feedback on the spatial pattern of sea surface temperature change with a g reen's function approach. *Journal of Advances in Modeling Earth Systems*, **9 (5)**, 2174–2189.

Zhu, T., Y. Huang, and H. Wei, 2019: Estimating climate feedbacks using a neural network. *Journal of Geophysical Research: Atmospheres*, **124 (6)**, 3246–3258.

APPENDICES

Appendix A

Supplementary Material for Chapter 2

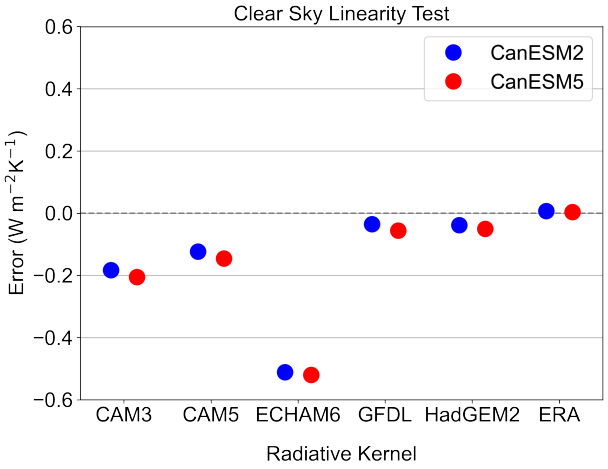

Figure A.1: Clear sky linearity test for 6 sets of radiative kernels considered in this study (CAM3, CAM5, ECHAM6, HadGEM2, and ERA kernels) tested using each version of CanESM. Y-axis error is defined as the absolute difference between the Gregory regression derived net clear sky climate feedback parameter, and radiative kernel derived net clear sky climate feedback parameter.

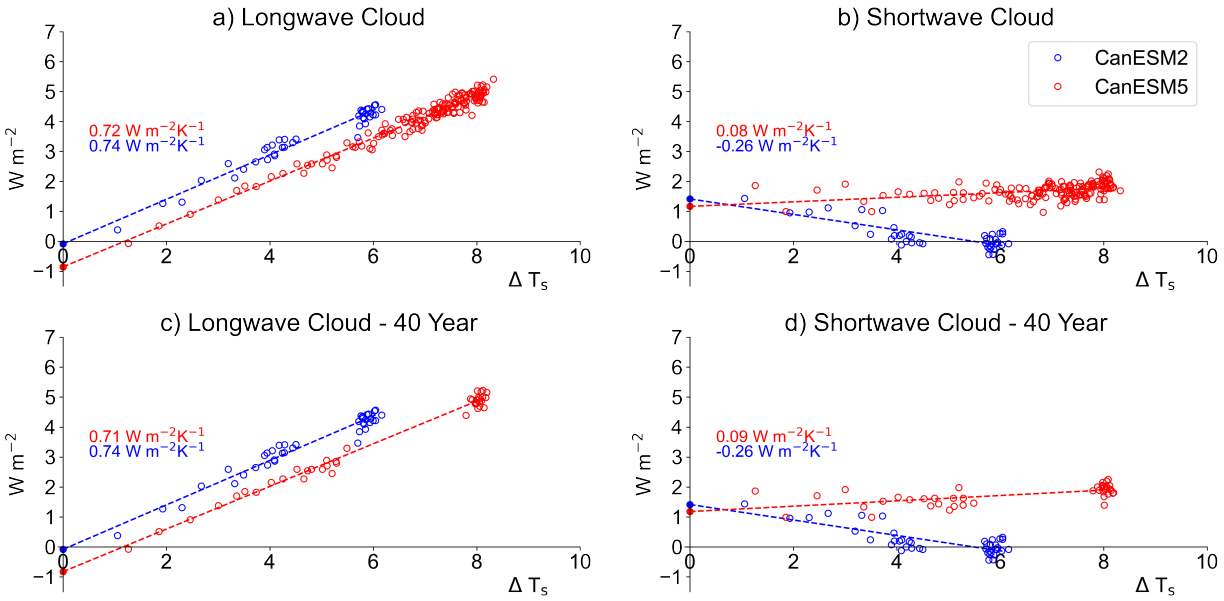

Figure A.2: Cloud long- and shortwave flux plotted against global, annual mean surface temperature change in abrupt-4xCO2 simulations for CanESM2 (blue) and CanESM5 (red), calculated using the cloud radiative kernel method. Standard 150 year Gregory regressions are conducted, where the slope of the regression line equals the cloud feedback (in $Wm^{-2}K^{-1}$). Panels a & b show regressions using all available years of data for each model version, whereas panels c & d show subsampled data for CanESM5 (years 1-20 & 120-140).

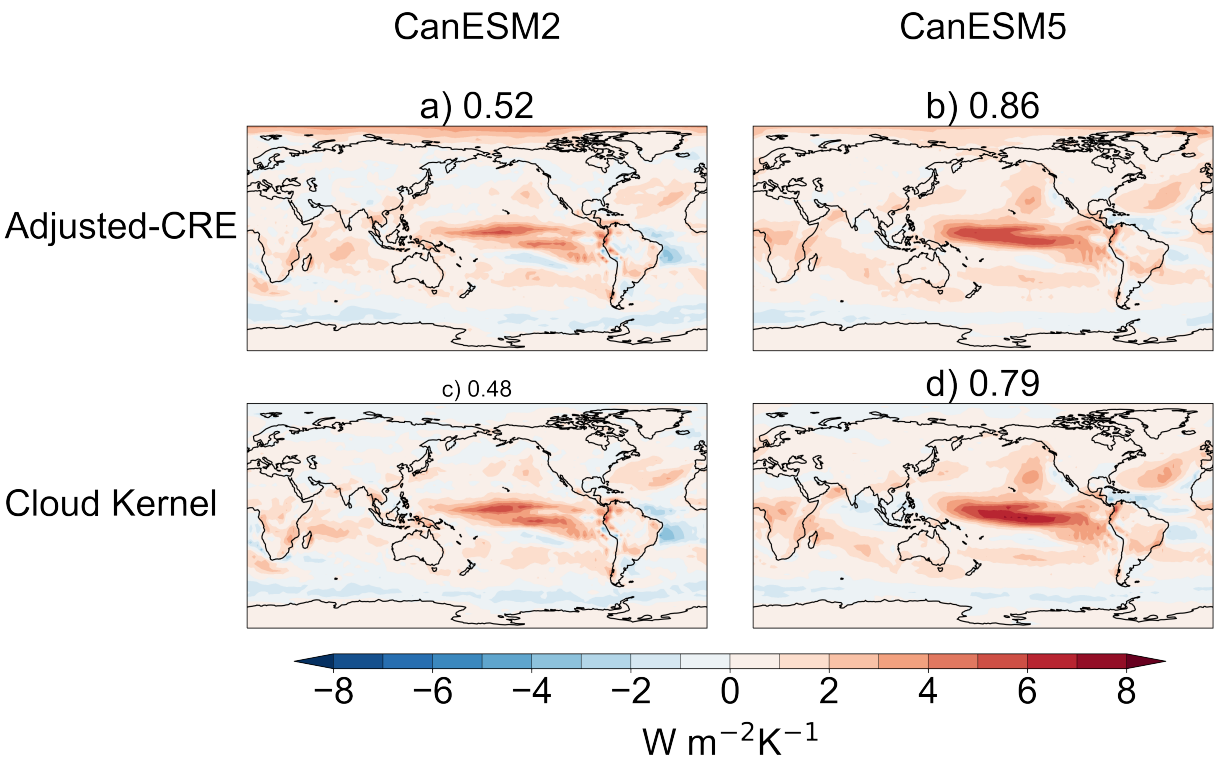

Figure A.3: Comparison of annual mean net cloud feedbacks for CanESM2 (panels a & c) and CanESM5 (panels b &d), calculated using the adjusted-CRE method and the cloud kernel method. Global mean values are shown in square brackets next to each subplot title. CanESM2 Pearson's $r = 0.72$ ($p < 0.01$); CanESM5 Pearson's $r = 0.86$ ($p < 0.01$).

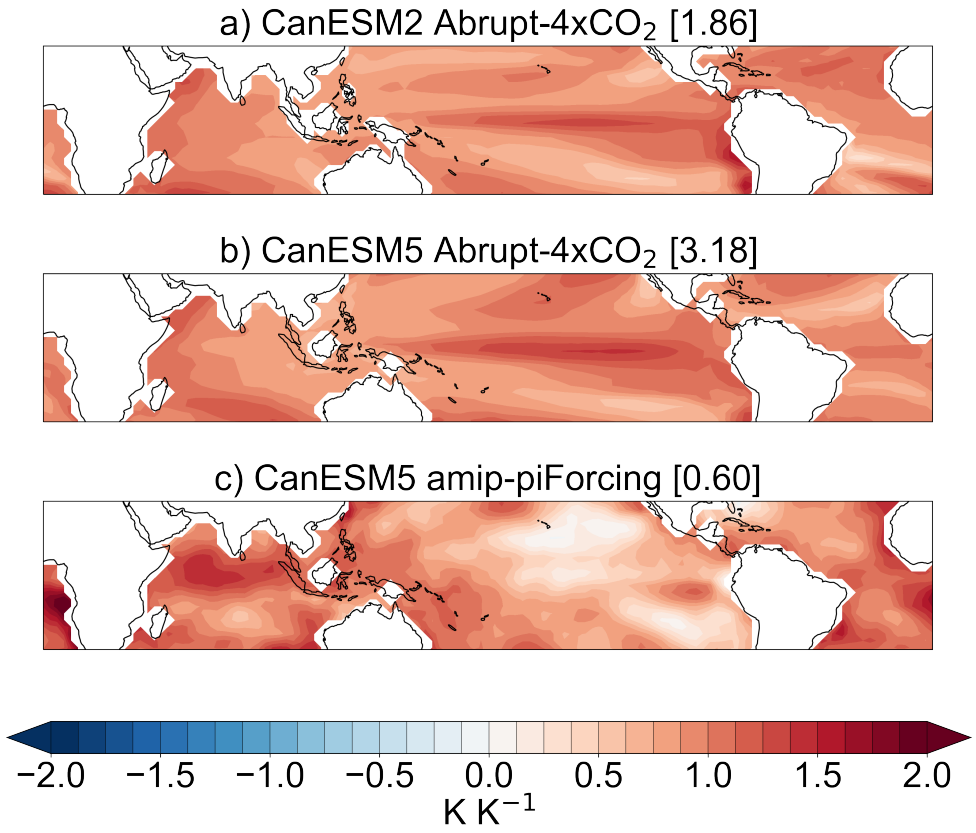

Figure A.4: Tropical SST response for the a) CanESM2 abrupt 4xCO_2 simulation, b) CanESM5 abrupt 4xCO_2 simulation, and c) CanESM5 amip-piForcing simulation. Responses are defined as the difference between 20 year means taken from the beginning and end of each simulation. All grid box values are divided by the global mean response for each respective simulation, which is shown in square brackets in each subplot title.

Appendix B

Supplementary Material for Chapter 3

Adjustment	$4xCO_2$	$SOLAR_e$	$SOLAR_b$	$G1_e$	$G1_b$
a	0±0	0±0	0±0	0±0	0±0
T_s	1.25±0.01	0.19±0	0.21±0	1.44±0.01	1.47±0.01
T_l	-0.40±0.02	0.41±0.02	0.43±0.02	0.06±0.02	0.15±0.02
T_p	-1.54±0.02	0.62±0.03	0.76±0.03	-0.82±0.02	-0.76±0.02
Q_s	0.01±0	-0.01±0	-0.01±0	0±0	0±0
Q_t	0.34±0.02	-0.58±0.02	-0.64±0.02	-0.12±0.02	-0.16±0.02
C_{sw-bl}	0.64±0.05	0.38±0.04	0.39±0.04	1.24±0.04	1.29±0.04
C_{sw-ft}	1.25±0.05	0.13±0.05	0.08±0.05	1.25±0.04	1.35±0.05
C_{lw-bl}	-0.07±0.01	-0.03±0	-0.04±0	-0.13±0.01	-0.14±0.01
C_{lw-ft}	-0.01±0.03	0.11±0.03	0.15±0.03	0.18±0.02	0.17±0.03
Net	1.47±0.07	1.20±0.07	1.32±0.07	3.10±0.06	3.37±0.06

Table B.1: Global, annual mean radiative adjustments for all experiments in this study. From top to bottom, adjustments are listed as surface albedo (a), stratosphere temperature (T_s), lapse rate (T_l), Planck (T_p), stratosphere water vapour (Q_s), troposphere water vapour (Q_t), shortwave boundary layer cloud (C_{sw-bl}), shortwave free troposphere cloud (C_{sw-ft}), longwave boundary layer cloud (C_{lw-bl}), longwave free troposphere cloud (C_{lw-ft}). All values are 30 year means ± 1 standard error of mean.

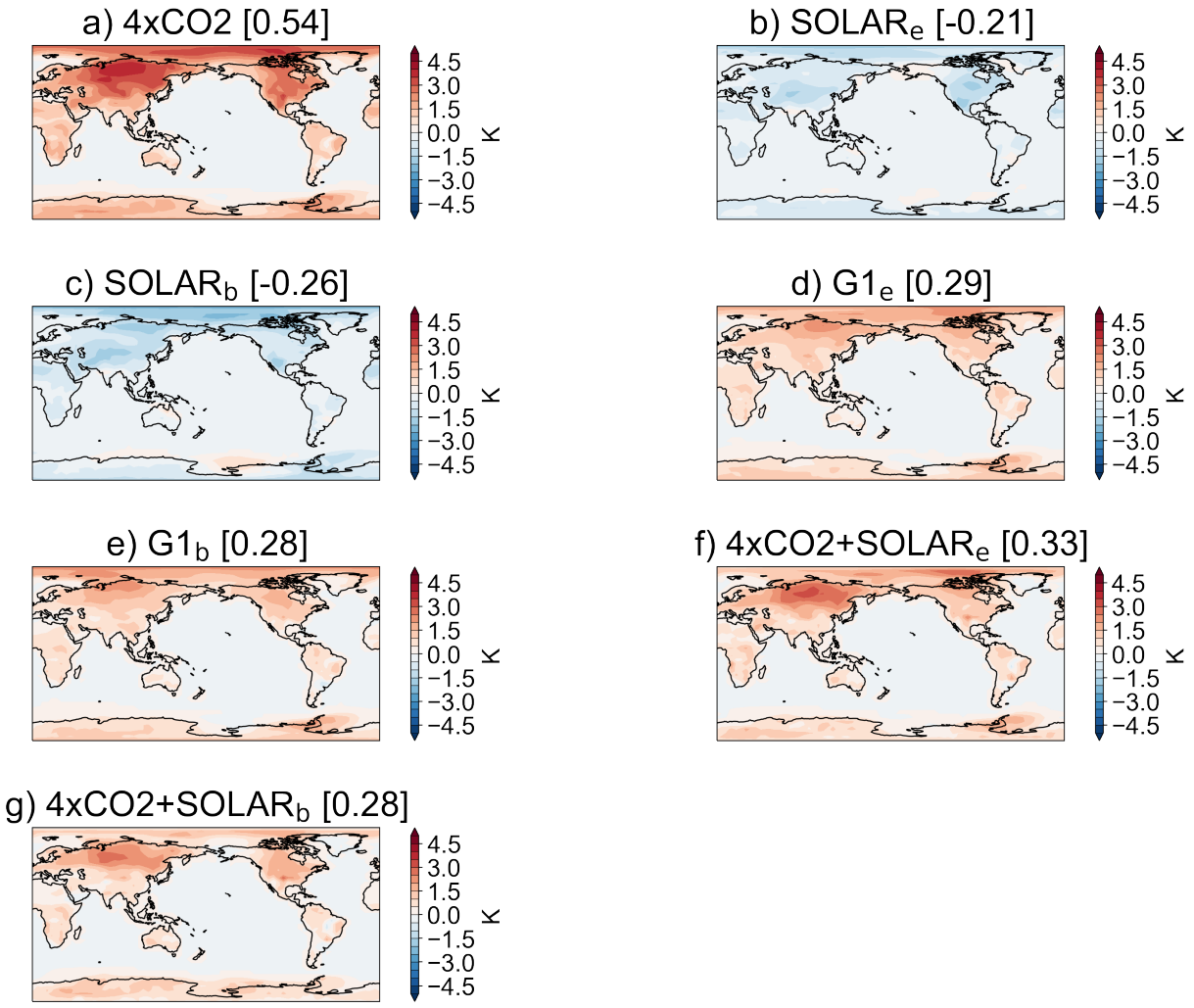

Figure B.1: 30 year annual mean surface temperature responses for all experiments in this study. Experiments are listed as subplot titles and values in square brackets are global means.

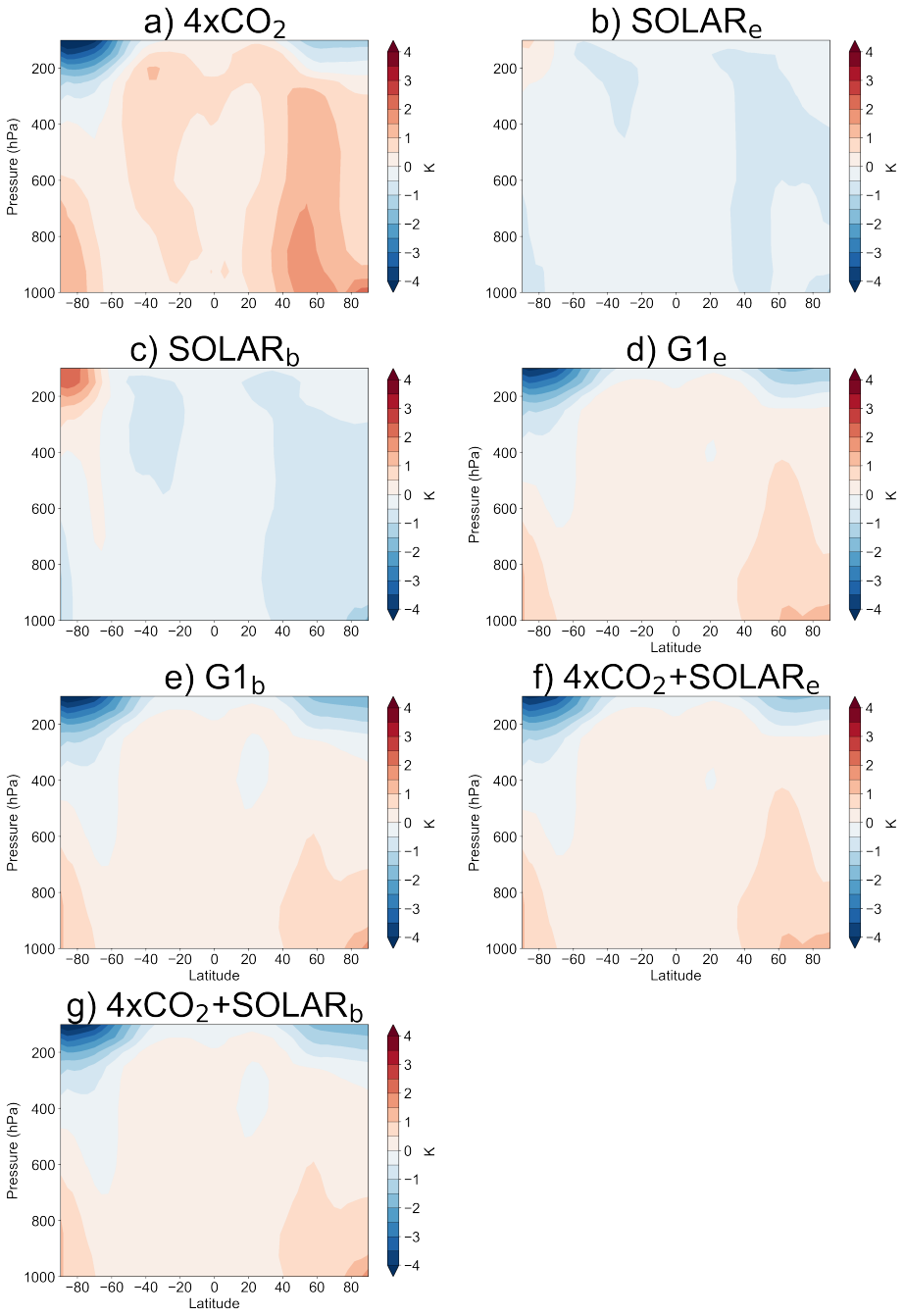

Figure B.2: 30 year annual, zonal mean air temperature responses for all experiments in this study. Experiments are listed as subplot titles.

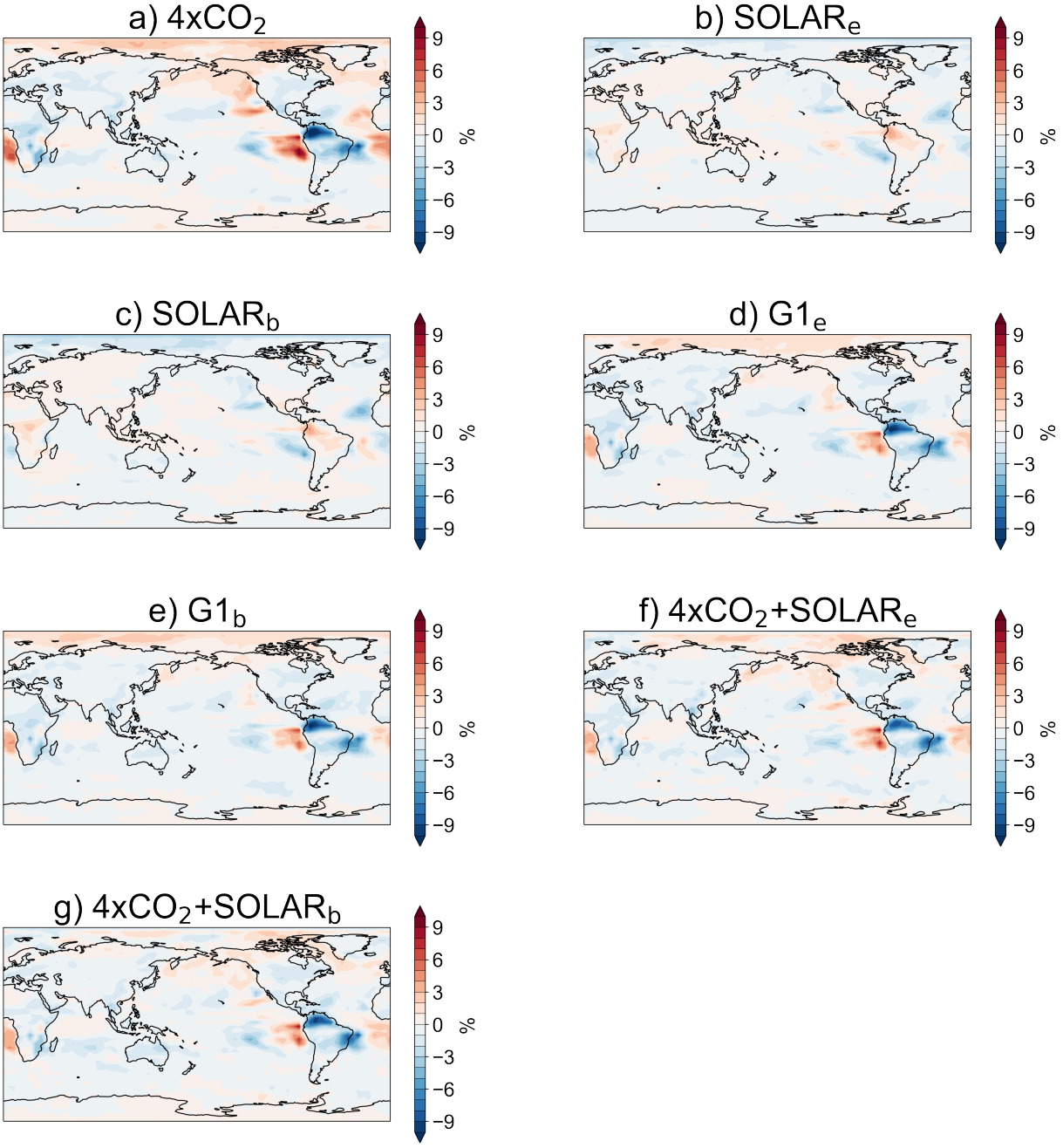

Figure B.3: 30 year annual mean ISCCP cloud fraction response (in %) from the 800-680 hPa CTP bin summed across all optical depths.

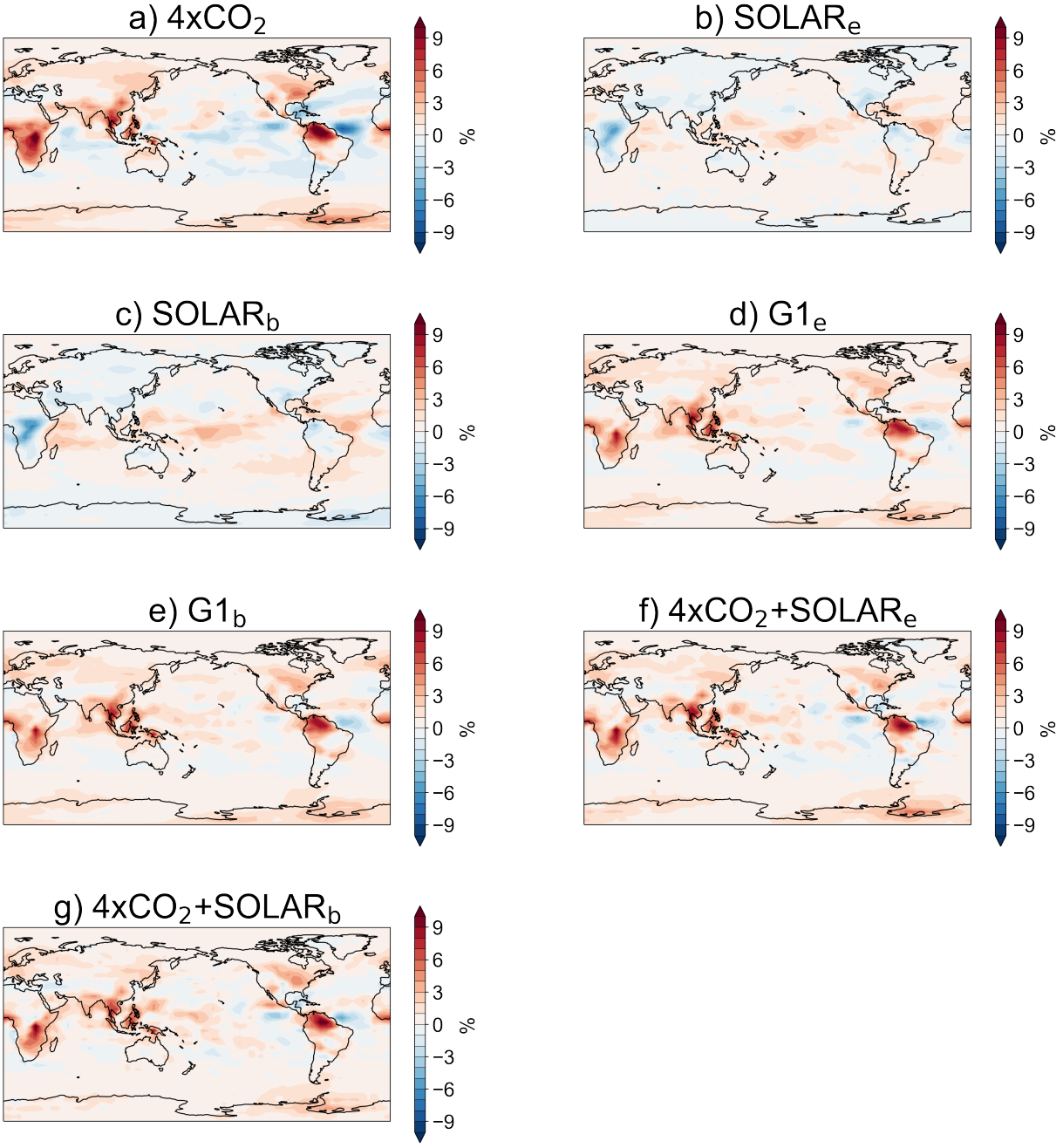

Figure B.4: 30 year annual mean ISCCP cloud fraction response (in %) from the 180-50 hPa CTP bin summed across all optical depths.

Appendix C

Supplementary Material for Chapter 4

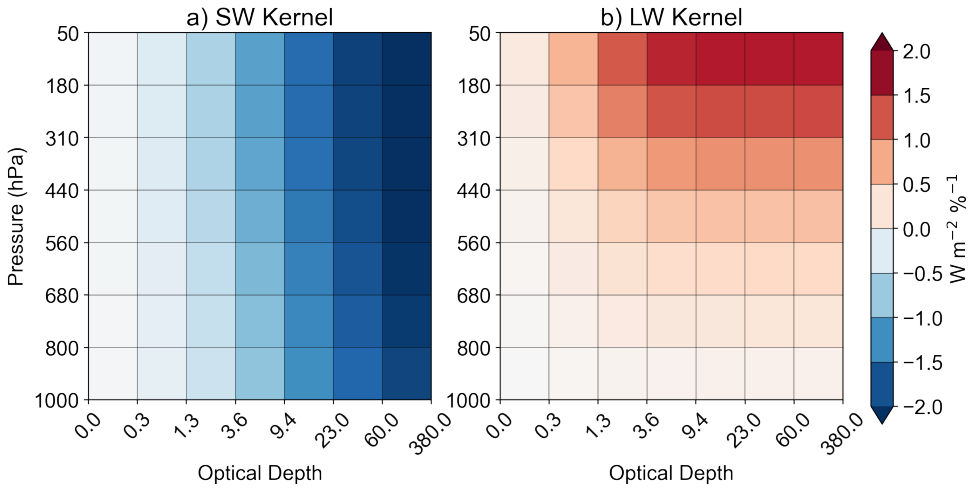

Figure C.1: a) & b) Global, annual mean ISCCP cloud radiative kernels (in W m^{-2}%$^{-1}$) from Zelinka et al. (2012a). The kernels are plotted on optical depth (x) and cloud top pressure (y) axes. The SW kernel was mapped to the long term climatology of the CTL experiment clear sky surface albedo before taking the global mean.